ABSTRACT

Title of Thesis: VEHICLE HANDLING, STABILITY,

AND BIFURCATION ANALYSIS

FOR NONLINEAR VEHICLE MODELS

Vincent Nguyen, Master of Science, 2005

Thesis directed by: Dr. Gregory A. Schultz
                        Department of Mechanical Engineering

Vehicle handling, stability, and bifurcation of equilibrium conditions were studied using a state vector approach. The research provided a framework for an improved method of vehicle handling assessment that included non-linear regions of performance and transient behavior. Vehicle models under pure lateral slip, constant velocity, and constant front steer were developed. Four-wheel, two-axle vehicle models were evolved from simpler models and were extended to include vehicle roll dynamics and lateral load transfer effects. Nonlinearities stem from tire force characteristics that include tire force saturation. Bifurcations were studied by quasi-static variations of vehicle speed and front steer angle. System models were expanded, assessing overall stability, including vehicle behavior outside normal operating ranges. Nonlinear models of understeering, oversteering, and

neutral steering vehicles were created and analyzed. Domains of attraction for stable equilibrium were discussed along with physical interpretations of results from the system analysis.

VEHICLE HANDLING, STABILITY,

AND BIFURCATION ANALYSIS

FOR NONLINEAR VEHICLE MODELS

by

Vincent Nguyen

Thesis submitted to the Faculty of the Graduate School of the
University of Maryland, College Park in partial fulfillment
of the requirements for the degree of
Master of Science
2005

Advisory Committee:

Dr. Gregory A. Schultz, Chairman/Advisor
Professor Balakumar Balachandran
Professor David Holloway

DEDICATION

To my father, who always allowed me to find my own path. Thank
you for your support in all of my endeavors.

ACKNOWLEDGEMENTS

TABLE OF CONTENTS

LIST OF TABLES

Chapter 1

Introduction

Vehicle dynamics and stability have been of considerable interest to automotive engineers, automobile manufacturers, the government, public safety groups, and the general public for a number of years. The obvious dilemma is that people naturally desire to drive faster and faster on the roads and highways, yet they expect their vehicles to be "infinitely" stable and safe during all normal and emergency maneuvers. For the most part, people pay little attention to the limited handling potential of their vehicles until some unusual behavior is observed that often results in fatality. Extreme examples of this are the handling behavior of the Chevrolet Corvair in the 1960s and the recent rollovers experienced with the Ford Explorer in the 1990s. Although there was much confusion about the exact cause of the Explorer rollovers, since they seemed to in part be linked to a model of Firestone tires, it is interesting that Ford soon lengthened the wheelbase of the vehicle. Nonetheless, significant incidents occurred, resulting in public outcry for improvement in safety. Note that the rates of speed at which drivers travel is rarely mentioned by the public as a root cause.

The fundamentals of the physics of vehicle handling began to be explored in earnest in the 1930s and 1940s by Olley *et al.* [15]. This work began by exploring

the basic behavior of pneumatic tires, which at the time were bias ply constructions. Radial tires began to gain widespread use in the 1970s. These new tires behaved somewhat differently, affecting vehicle behavior, and led to a rapid development of speed-rated tires. Better tires made it more comfortable for drivers to travel even faster. Consequently, interest in vehicle handling continued.

Recent efforts to better understand vehicle handling have demonstrated that much is still to be learned and developed in this field as vehicles continue to evolve. These efforts include cooperative work done by the major automobile manufacturers through the Alliance of Automobile Manufacturers [2], rule-making work and studies conducted by the National Highway Traffic Safety Administration (NHTSA), inspired by the rollover problems experienced with popular sport utility vehicles (SUVs), and Light Tactical Vehicle (LTV) handling studies being conducted by the U.S. Army.

The rapid success of sport utility vehicles in the U.S. has heightened interest in related rollover problems. Though most of the rollovers were tripped by leaving the roadway or hitting an obstacle, approximately 10% are unexplained and likely related to vehicle handling behavior [5]. The relatively high center-of-gravity of SUVs make them highly susceptible to rollover for any number of reasons. The introduction of stability control systems in American cars has opened up many new and exciting opportunities for vehicle dynamicists and controls engineers in the field of vehicle handling and stability research. New questions have arisen, such as how to identify a spin-out while it is happening, what to do to control the behavior, and how to control the behavior without creating an additional safety hazard, such as making the vehicle completely unresponsive. In any regard, the field of vehicle handling and stability is perhaps more exciting and full of problems

to solve than ever.

Historically, vehicle handling has been studied predominately by first quantifying the steady-state behavior of vehicles and then trying to relate steady-state principles to transient dynamics. This is so because steady-state behavior is much easier to visualize than transient dynamics, which are much more difficult to describe, let alone visualize. Performance within the linear region of modern tires, usually from 0.3 to 0.4 g of lateral acceleration, is well understood and predictable for steady-state maneuvers, and also, to some extent, in the transient case. However, tires are very non-linear beyond 0.4 g and eventually saturate with subsequent degradation in lateral force capability. Combining complicated tire characteristics with lateral weight transfer, differences in front/rear roll stiffness, suspension and steering kinematics and compliance, and other factors make transient behavior very difficult to describe and predict. The differential equations that describe vehicle motion can be written in terms of a few key variables and parameters as linear time-invariant systems. However, the variables and parameters used in these equations are often highly non-linear.

This research, presents a way to visualize transient behavior over a broad set of vehicle operating states. The work presented here helps bridge the gap between steady-state handling principles and transient dynamics, and provides an interesting way to visualize handling behavior, understand how changes in vehicle set-up affect stability, and provide a better way to teach vehicle dynamics. Ideas for future work to extend this research to possibly better characterize transient behavior will be introduced. In this chapter, the basics of steady-state vehicle dynamics will be presented, followed by discussion of how the system equations are typically developed. Finally, a brief literature review and introduction of the current research

will be given.

1.1 SAE vehicle model
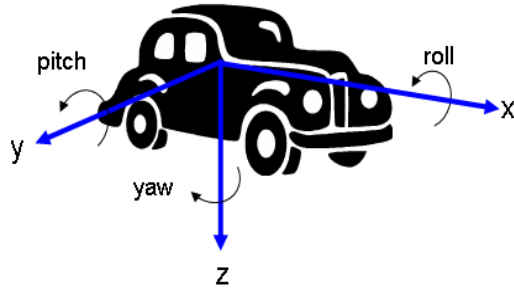
Figure 1.1: SAE vehicle coordinate orientations.

Unless otherwise noted, this paper uses the standard Society of Automotive Engineers (SAE) coordinate system shown in Figure 1.1 [8]. The vehicle's positive x axis is defined to be along the forward direction of the vehicle's longitudinal axis. The y axis is defined to be towards the right-hand side of the vehicle (while facing forward) and the z axis points in the downward direction. A two-axle, four-wheel vehicle with front wheel steering making a right-hand turn is shown in Figure 1.2. Also shown are the orientations of key vehicle parameters used in this research. The green line denotes the path of the vehicle center of gravity (CG), shown as a blue circle. The vehicle's instantaneous velocity, V, is shown tangent to the vehicle path. Vehicle sideslip, β, is defined as the angle between the vehicle x axis and the velocity vector at the CG, with positive sideslip defined with the vehicle axis oriented to the left of velocity. Front steer angle, δ_f, is the angle between the centerline of the front tires and the vehicle x axis. Positive steer is achieved with

the wheels steered to the right. Vehicle yaw rate, r is defined as a positive rotation about the vehicle z axis.
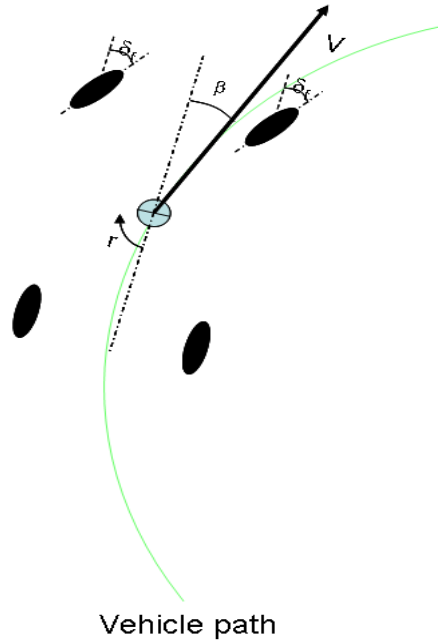
Figure 1.2: SAE four-wheel vehicle parameters. The blue circle represents the vehicle CG, β represents the vehicle sideslip, and δ_f represents the front steer angle.

1.2 Steady-state vehicle handling classification

Vehicle handling behavior is predominantly classified using the so-called understeer (US), oversteer (OS), and neutral steer (NS) conditions. These terms are traditionally applied to steady-state handling conditions. Steady-state handling can be defined as a maneuver in which there are constant vehicle parameters (steer angle, velocity, roll angle, etc.) and the vehicle motion is constant (constant yaw

rate, constant sideslip). Physically, this refers to a vehicle travelling at a constant velocity along a constant radius turn.

A two-axle, four-wheeled vehicle can be simplified using the so-called bicycle model [8], where each axle can be approximated as a single tire in line with the CG of the vehicle. The bicycle model representation of a four-wheeled vehicle is shown in Figure 1.3, and a diagram of a bicycle model vehicle under low-speed cornering conditions is shown in Figure 1.4. During low-speed cornering, it is assumed that the tires have not yet developed any lateral slip and are rolling in the direction of the velocity. Under this assumption, the front steer can be estimated as L/R, where L is the wheelbase of the vehicle and R is the radius of the turn. This steer angle is sometimes referred to as the Ackerman steer angle and is expressed in radians.
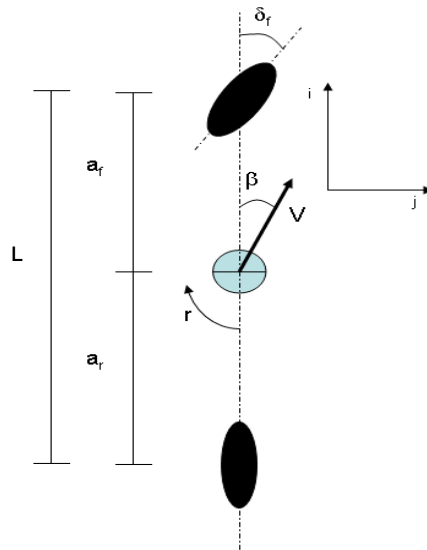
Figure 1.3: Simple bicycle model of a two-axle, four-wheel vehicle.

Under high-speed cornering conditions, where lateral tire slip has developed, the relationship between the actual steer angle and the Ackerman steer angle is
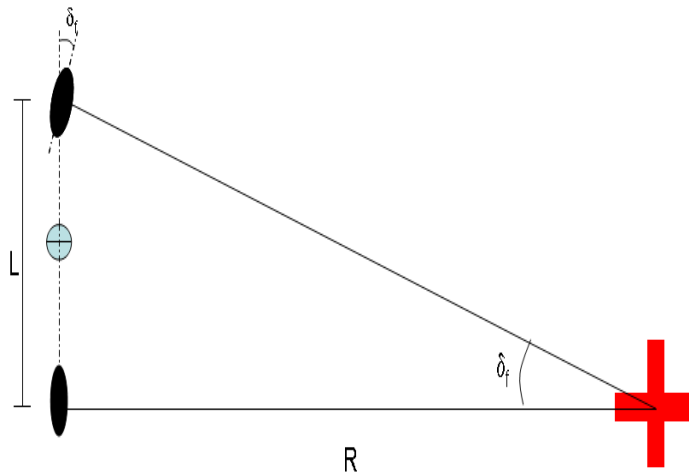
Figure 1.4: Diagram of low-speed cornering with bicycle model.

typically used to classify US/OS/NS for steady-state handling. For a high-speed right-hand turn, an understeering vehicle will have a front steer angle that is greater than the Ackerman steer angle. An oversteering vehicle will exhibit a lower steer angle than the Ackerman steer angle, and a neutral steering vehicle maintains the Ackerman steer angle through the high speed turns.

US/OS/NS can be described analytically. The tire force orientation for the US/OS/NS classification used by Gillespie [8] is shown in Figure 1.5. Tire lateral force is labelled as F and the tire slip angle, α, is defined as the angle between the velocity at the tire and the heading of the tire. Using the bicycle model under steady-state cornering in the positive yaw direction (right-hand turn), an expression for front steer angle can be developed (Eq. (1.1)). The terms α_f and α_r represent the front and rear tire slip angles. If in the maneuver, the front slip angle is greater than the rear, the subsequent front steer angle is greater than the Ackerman steer angle and the vehicle exhibits understeer. Conversely, if the rear slip angle is greater than the front, the steer angle is less than the Ackerman

7

steer angle and the vehicle exhibits oversteer. If the slip angles are equal, then the vehicle is steering at the Ackerman steer angle and is exhibiting neutral steer.

$$\delta_f = \frac{L}{R} + \alpha_f - \alpha_r \tag{1.1}$$
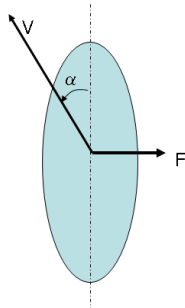
Figure 1.5: Tire force orientations for linear model used in [8] for classification of US/OS/NS.

Gillespie takes the analysis further with the use of a linear tire force model. Tire lateral force is assumed to be a linear function of the slip angle, and $F = C_\alpha \cdot \alpha$ describes the relationship. The coefficient C_α is called the tire-cornering stiffness and is a property of the tire. The tire model can then be applied along with a force balance equation to provide another expression for front steer angle, Eq. (1.2) [8]. W_f and W_r are the vehicle weights at the front and rear axles. In this expression, if $\left(\frac{W_f}{C_{\alpha f}} - \frac{W_r}{C_{\alpha r}} \right)$ is equal to 0, the vehicle is always neutral steering. However, if $\left(\frac{W_f}{C_{\alpha f}} - \frac{W_r}{C_{\alpha r}} \right)$ is positive, front steer angle can be expected to be greater than the Ackerman steer angle (at any given positive speed). In addition, the steer angle can be expected to continue to increase with respect to increasing vehicle speed. This means that the vehicle not only exhibits understeer, but it exhibits terminal understeer (increasing steer angle) as the vehicle speed is increased. Similarly

8

when $\left(\frac{W_f}{C_{\alpha f}} - \frac{W_r}{C_{\alpha r}}\right)$ is negative, the front steer angle will always be less than the Ackerman angle (for positive velocity), and it will continue to decrease as vehicle speed is increased. This vehicle not only exhibits oversteer, but exhibits terminal oversteer as the velocity is increased.

$$\delta_f = \frac{L}{R} + \left(\frac{W_f}{C_{\alpha f}} - \frac{W_r}{C_{\alpha r}}\right)\frac{V^2}{gR} \tag{1.2}$$

A handling diagram for the linear tire model and vehicle driving on a constant radius is provided in Figure 1.6. Steer angle is plotted against lateral acceleration (V^2/Rg). A neutral steering vehicle will maintain a constant steer angle (the Ackerman steer angle). An understeering vehicle produces steer angles greater than the Ackerman steer angle for nonzero velocity and will continue to increase steer angle at a rate proportional to the lateral acceleration. An oversteering vehicle operates at a steer angle less than the Ackerman steer angle and will decrease steer angle at a rate proportional to the lateral acceleration.

In practice, during a maneuver, the operator has no notion of the Ackerman steer angle. Instead, the operator perceives a change in steer angle as velocity is increased or decreased. In addition, because of nonlinear tire responses, some vehicles initially understeer, but as lateral acceleration is increased, a transition to neutral steer and eventually oversteer occurs. Consequently, it may be more practical from a driver's point of view to think of the onset of neutral steer and oversteer as occurring when the required steer angle to negotiate the turn begins to decrease (as speed is increased).

As such, the commonly accepted relationship between the actual steer angle and the Ackerman steer angle (greater than or less than) may not be descriptive enough. For practical use, US/OS/NS should be defined by the slope of the steer angle/acceleration curve rather than just the value of the steer angle (as compared

to the Ackerman steer angle). With the linear tire model, the relationship to the no-slip (Ackerman) steer angle coincides with rate of change of the steer angle (if $\delta > L/R$ then δ is always increasing and vice versa), so there is no distinction between the two definitions. With nonlinear tire models, this is not necessarily the case and a distinction must be made. In Figure 1.7, a typical handling diagram for a heavy truck is shown. Notice how the vehicle transitions from understeer to oversteer. The transition point occurs well before the steer angle drops below the Ackerman angle. US/OS/NS within the nonlinear tire force regions will be discussed later in this thesis.
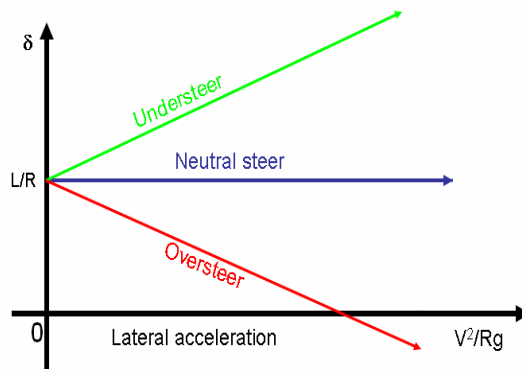
Figure 1.6: Handling diagram for US/OS/NS using linear tire model.

1.3 State space, system stability, and phase portraits

The models used in this research are presented in state-space format. System states are the essential parameters required to describe the system dynamics. Furthermore, all of the systems presented are autonomous, meaning that the governing
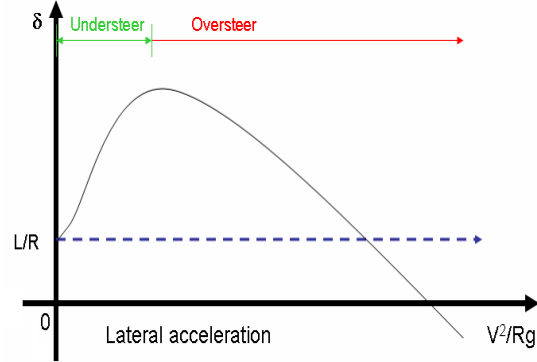
Figure 1.7: Handling diagram for nonlinear tire forces.

differential equations are completely a function of the current state. Autonomous system equations can be put into the form $\dot{x} = F(x; M)$, where x is the state vector, M is a vector of system parameters and F is a vector function.
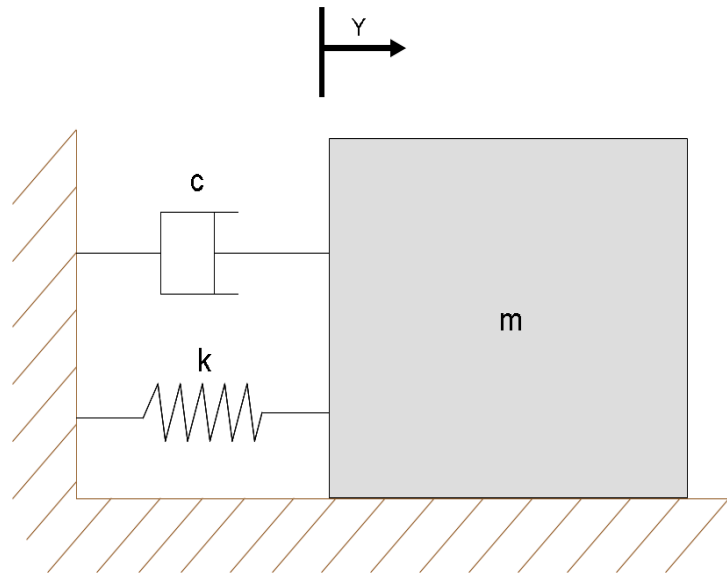
Figure 1.8: Spring-mass-damper system.

In the spring mass system depicted in Figure 1.8, system operation can be defined by the one-dimensional position and velocity of the mass (y and $\dot{y}$). The

11

state vector x can be defined as in Eq. (1.3). The governing equation for the unforced system is shown in Eq. (1.4). This represents an autonomous system, since the governing equation is expressed in state space as in Eq. (1.5), where M is a vector of the system parameters (m, c, and k), and the vector function F is defined according to Eq. (1.6).

$$x = \begin{pmatrix} y \\ \dot{y} \end{pmatrix} \tag{1.3}$$

$$m\ddot{y} + c\dot{y} + ky = 0 \tag{1.4}$$

$$\dot{x} = \begin{pmatrix} \dot{y} \\ \ddot{y} \end{pmatrix} = F(x; M) \tag{1.5}$$

$$F(x; M) = \begin{pmatrix} \dot{y} \\ (-ky - c\dot{y})/m \end{pmatrix} \tag{1.6}$$

Equilibrium solutions in state space refer to solutions where the states hold steady through time. In analytic terms, an equilibrium solution, x_0, is a state where the rate of change of the state vector $\dot{x}_0 = F(x_0; M) = 0$. The local stability of an equilibrium solution can be determined by observing the behavior of the linearized vector function F at the equilibrium solution [17]. If the state vector x has n dimensions, x can be expressed as $x = [x_1, x_2, x_3, \cdots, x_n]$ and F as $F = [F_1, F_2, F_3, \cdots, F_n]$, where $F_i = \dot{x}_i \quad \forall i \in Z, 1 \leq i \leq n$. Linearization is accomplished by first determining the Jacobian matrix, A, which is defined as $A = D_x F(x; M)$ at $x = x_0$, where $D_x F(x; M)$ is defined by Eq. (1.7). If the eigenvalues of the Jacobian matrix A have all nonzero real parts, the equilibrium point, x_0 is considered to be hyperbolic. For a hyperbolic equilibrium point, if all the eigenvalues have negative real parts, then all local perturbations away from the equilibrium solution, x_0, decay with time and the solution is stable. If one or

more of the eigenvalues of A have positive real parts, then perturbations in some directions away from x_0 will increase with time and the solution is unstable. If an unstable point has some eigenvalues with negative real parts and the rest with positive real parts, perturbations away from x_0 in certain directions will decay while perturbations in other directions will increase, and the solution is called a saddle point [17].

For the simple spring-mass-damper example, the equilibrium solution can be found by solving $F(x; M) = 0$. The only equilibrium solution is $y = 0$, $\dot{y} = 0$. The Jacobian matrix can be defined according to Eq. (1.8). The eigenvalues at $x_0 = \begin{pmatrix} 0 \\ 0 \end{pmatrix}$ can be shown to always be negative for positive values of m, k, and c. Therefore, x_0 can be considered locally stable (and globally stable since the system is linear). Another way to visualize this is to look at a phase portrait of the system. Figure 1.9 is a phase portrait of the spring-mass-damper system with $m = 1$, $k = 1$, and $c = 1$. The phase portrait is a graphical representation of the state space, with the abscissa as the velocity value ($\dot{y}$) and the ordinate as the position value (y). The trajectories shown in blue represent the evolution of the states from the initial conditions (represented by the red x's) for velocity and position. The phase portrait clearly shows that trajectories initiated throughout the phase plane are attracted to the equilibrium point at $(0,0)$. This demonstrates the stability of the solution, since perturbations away from the equilibrium point will propagate back toward the equilibrium point. Phase portraits can be used as visualization tools to describe system state progression and assess qualitative

stability, and will be used throughout this research.

$$D_x F(x; M) = \begin{pmatrix} \frac{\partial F_1}{\partial x_1} & \frac{\partial F_1}{\partial x_2} & \cdots & \frac{\partial F_1}{\partial x_n} \\ \frac{\partial F_2}{\partial x_1} & \frac{\partial F_2}{\partial x_2} & \cdots & \frac{\partial F_2}{\partial x_n} \\ \vdots & \vdots & \ddots & \vdots \\ \frac{\partial F_n}{\partial x_1} & \frac{\partial F_n}{\partial x_2} & \cdots & \frac{\partial F_n}{\partial x_n} \end{pmatrix} \tag{1.7}$$

$$A = D_x F(x; M) = \begin{pmatrix} 0 & 1 \\ -k/m & -c/m \end{pmatrix} \tag{1.8}$$
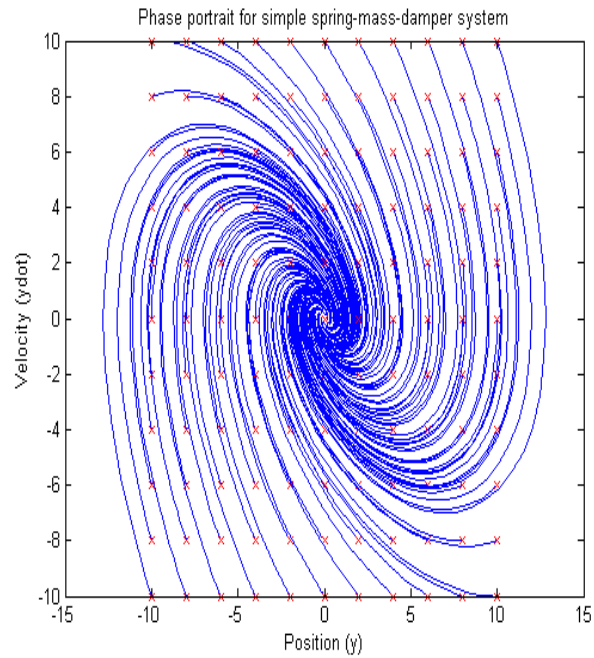
Figure 1.9: Phase portrait for simple spring-mass-damper system with $m = 1$, $k = 1$, $c = 1$.

1.4 Literature review

1.4.1 Handling classifications

Several vehicle dynamic handling classifications have been developed. Most commonly, the classifications refer to steady state handling conditions and US/OS/NS. Detailed discussions can be found in the text books [8] [15]. One such treatment was presented in Gillespie [8] and accounted for several different influencing factors, including tire cornering stiffnesses, camber thrust, roll steer, lateral force compliance steer, aligning torque, and lateral load transfer. The analysis addressed many different parameters that affect the handling classification, but treatment of individual terms was somewhat simplified. For instance, tire forces were only considered in the linear range, and lateral load transfer effects were simplified at each axle using a second order polynomial function.

Milliken also provided some discussion about US/OS/NS for the linear tire case, but recognized that the linear model only applied up to about 0.3 g of lateral acceleration [15]. Nonlinear tire and vehicle characteristics were addressed using the Milliken Research Associates (MRA) Moment Method. This method characterized steady-state handling by examining the charts of vehicle yaw moment versus lateral acceleration. The analysis is somewhat obscure since it deals with quantities not directly linked to physical parameters.

Gillespie and Milliken also discussed the idea of critical speed for oversteering vehicles. The critical speed is the speed (for a constant radius test) where the steer angle has decreased back to zero. In the handling diagrams, this is the speed that corresponds to the lateral acceleration where the plot crosses the x-axis (Figure 1.6).

Karnopp briefly tackled the issue of nonlinear tire forces in the US/OS/NS classification [10]. A similar method is presented later in this thesis. Karnopp also mentioned the capability of a vehicle to exhibit different US/OS behavior at or near limit conditions, depending on the tire saturation rates [10].

1.4.2   Stability notions

Handling classifications allow for stability limit definitions. For instance, US/OS/NS can be quantified using understeer and oversteer gradients (slope of handling diagram) [8] [15], and quantifiable limits can be defined. Gillespie uses critical speed (where the vehicle has turned back to zero steer) for oversteering vehicles as a stability limit [8].

Milliken provided some additional stability discussions using the linear vehicle model. The stability of steady-state operation was evaluated for US/OS/NS vehicles with respect to step sideslip inputs (at 0 steer). Also, steady-state stable operating conditions were calculated using the linear bicycle model for particular steer angles and sideslip values. This type of analysis is relatively simple for a linear system, since steer angle and sideslip can be directly superimposed to define overall tire forces. In the nonlinear case, Milliken's Moment Method was developed to determine steady-state operating conditions given a particular steer angle and sideslip.

A numeric bifurcation analysis is presented in [4] that studies the hunting motions of rail vehicles. Hopf bifurcations [17] and limit cycle stability are examined for railcars with four- and two-axle bogies, resulting in a simple bifurcation model that relates the onset of stable limit cycles (hunting motions) to vehicle speed.

Stability limits are also required to define loss of vehicle control during tran-

sient field testing procedures. Forkenbrock, in [6], presented a NHTSA-developed standard to define a spinout during a sine steer maneuver. Spinout or loss of vehicle control is defined using yaw rate drop-off following a maneuver. After the steer maneuver, if the vehicle yaw rate is not reduced to a percentage of the maximum within a certain time, a loss of control is determined.

1.4.3 State space approaches

Interestingly enough, little work has been done with vehicle stability using a state space system. For constant vehicle parameters, the state space vehicle models are time invariant systems. Karnopp used a state space approach to study the stability of a linear vehicle system (bicycle model with linear tire forces) [10]. Steady-state dynamic equilibrium solutions were calculated and the stability of dynamic equilibrium solutions were also assessed directly by linear stability methods.

Ono *et al.* presented a similar state space model in [18]. This model instead used nonlinear tire forces. Stability was briefly assessed, and changes in the stable solutions with respect to steer angle were studied. A front steer controller was also proposed that intended to keep the nonlinear system stable while maneuvering. Nevertheless, Ono's work was fairly brief and simplified in terms of stability analysis, since the focus of the work was on control.

1.5 Contributions and thesis organization

The main contributions of this thesis are the following:

- The nonlinear bicycle model for stability analysis presented in [18] was extended to include tandem-axle vehicle dynamics and independent four-wheel

17

dynamics.

- Bifurcations of equilibria were shown to occur with respect to vehicle velocity, in addition to steer angle.

- A Light Tactical Vehicle (LTV) four-wheel model was created, which included the development of a nonlinear tire model generated from limited experimental tire data.

- The vehicle model was extended to study operations beyond normal operating limits. This allowed analysis of overall system stability characteristics.

- A lateral load transfer model was also presented. This model included roll dynamics and tire force propagation.

- A detailed discussion about the physical insights and practical applications of the analysis are provided.

- A presentation of US/OS/NS for nonlinear tire models was created and is presented along with analysis results for US/OS/NS vehicles.

The rest of this thesis is organized as follows:

Chapter 2: In this chapter, all vehicle models are presented, beginning with the original model provided in [18]. Bifurcations, or qualitative changes in the phase portraits, are shown as front steer angle is varied. Similar bifurcations involving the loss of stable equilibrium solutions are demonstrated with respect to velocity as the control parameter. The model is then extended for use with tandem-axle vehicles. Model parameters were adjusted to provide similar results as with the two-axle bicycle model. An independent four-wheel (non-bicycle) model is

then presented for a two-axle vehicle. Advantages are discussed, and results for the four-axle case are shown.

Chapter 3: In this chapter, the creation of a vehicle-based LTV model is outlined. A tire model is first developed using a semi-empirical formulation along with a genetic optimization algorithm. Four-wheel LTV model results obtained with the new tire model are presented. The model is then expanded to allow for accurate results at broader operating ranges. Domains of attraction for stable points are also studied. Lateral load and roll dynamics are discussed, and a lateral load LTV model is developed and results are presented.

Chapter 4: In this chapter, the physical insights gained from the analysis are discussed. The practical meanings of the phase portraits and the equilibrium solutions are discussed, as well as the domains of attraction for the stable points. Bifurcation diagrams with respect to steer angle and the velocity are investigated and tied to physical behavior. The expanded phase portraits are discussed in terms of practical stability and analytical system stability. US/OS/NS classifications are presented for nonlinear vehicle models, and US/NS/OS vehicles are studied using the nonlinear analysis. Lateral load model results are also examined.

Chapter 5: Concluding remarks along with suggestions for future work are collected and presented in this chapter.

Chapter 2

Development of theoretical models

In this chapter, an effort is made to systematically describe the basic concepts and stability and bifurcation analysis techniques presented in this thesis. First, earlier work by Ono *et al.* [18] is reproduced for a bicycle model of a two-axle vehicle to explain and develop the basic concepts. Then, the simple bicycle model is extended to tandem rear-axle vehicles. Finally, a four-wheel vehicle model and associated analysis is presented, neglecting lateral weight transfer and roll dynamics. In Chapter 3, a case study is presented for a four-wheel general purpose utility vehicle, using real tire data. This new model is further developed to include lateral weight transfer and roll dynamics. A detailed discussion of physical insights and the utility of this stability approach is given in Chapter 4.

2.1   Bicycle model

The bifurcation analysis presented by Ono *et al.* [18] was based on a simple "bicycle" model. In this approach, the actual forces acting on the vehicle are approximated by modelling each axle as a single unit (single wheel). As such, individual tire slip angles or individual tire loading during cornering, were not

account for. Ono's model was setup in non-SAE standard coordinates, as shown in Figure 2.1. The variables a_f and a_r represented the distance from the front and rear axles to the center of gravity (cg) of the vehicle. Positive front steer was defined in the left direction, and positive vehicle sideslip, β, was defined to the left of the vehicle center line. The same model in standard SAE coordinates is shown in Figure 2.2. Due to the orientation of the original system and the symmetry of the "bicycle model" approach, both system coordinate representations are equivalent in terms of the system equations, Eq. (2.3).
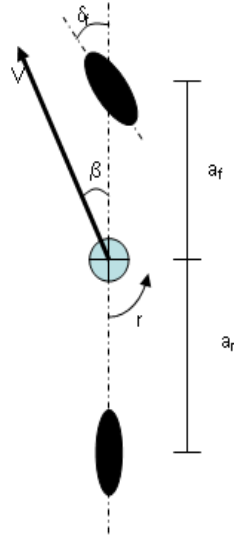
Figure 2.1: Bicycle model presented in [18].

$$mv(\frac{d}{dt}\beta + r) = F_f + F_r \tag{2.1}$$

$$I_z\frac{d}{dt}r = (a_fF_f - a_rF_r)cos(\beta) \tag{2.2}$$

$$\begin{pmatrix} \dot{\beta} \\ \dot{r} \end{pmatrix} = \begin{pmatrix} \frac{F_f+F_r}{mv} - r \\ \frac{(a_fF_f - a_rF_r)cos(\beta)}{I_z} \end{pmatrix} \tag{2.3}$$

Only constant vehicle characteristics were considered in this analysis, meaning
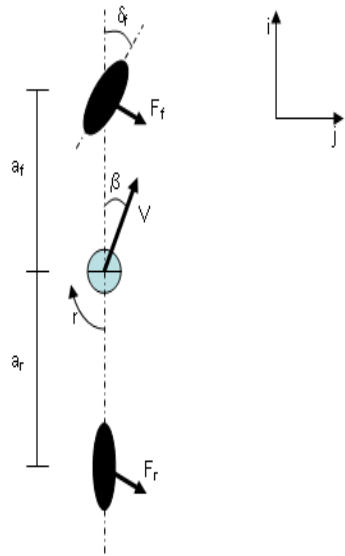
Figure 2.2: SAE representation of bicycle model.

there was no acceleration in the direction of the velocity and the front steer angle, δ_f, remained constant. Motion was described with two states: β, representing vehicle sideslip and r, representing vehicle yaw rate.

In this formulation, the overall axle forces (F_f and F_r) are defined in a direction perpendicular to vehicle velocity at the cg. The "bicycle model" approach treated each axle as a single tire with a single slip angle. Axle forces were calculated using an empirical tire formula, which was a simplified general form of the well known "magic tire formula" [19]. The tire equation used by Ono *et al.* is shown in Eq. (2.4). The slip angle, α, and the direction of the force were defined according to Figure 2.3. The parameters B, C, D, and E were all constant parameters based on empirical tire data, with slip angles as the only variable. The parameters used for the front and rear tires were different, accounting for the tires themselves as well as suspension setup and the weight distribution effects. A list the coefficients

used are shown in Table 2.1. In Figure 2.4 the tire force versus slip angle diagrams
are shown for the front and rear tires. Note that the nonlinear characteristics of
the tires prior to, during and after saturation were represented.

$$F = D \cdot \sin \left[C \cdot \tan^{-1} \left\{ B \cdot \alpha - E \cdot \left(B \cdot x - \tan^{-1}(B \cdot \alpha) \right) \right\} \right] \qquad (2.4)$$
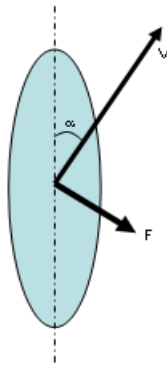
Figure 2.3: Tire force diagram.

Table 2.1: Bicycle model tire parameters.

	B	C	D	E
Front	11.275	1.56	-2574.7	-1.999
Rear	18.631	1.56	-1749.7	-1.7908

Slip angles at each of the tires were calculated by resolving the i and j components of the velocity vectors based on the vehicle coordinate system, as shown
in Eqs. (2.5) and (2.6). The vehicle was assumed to be rigid in the yaw direction.
Eqs. (2.7), (2.8), (2.9), and (2.10) give the front and rear slip angles of the states.
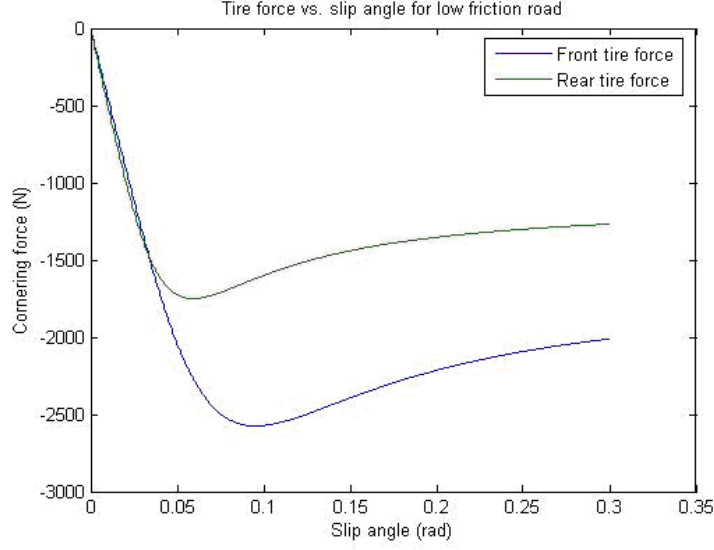
Figure 2.4: Tire force versus slip angle for front and rear tires in bicycle model.

The terms β_f and β_r are the sideslips at each of the wheels, and α_f and α_r are the associated slip angles.

$$V_f = V\cos(\beta)\vec{i} + (V\sin(\beta) + a_r r)\vec{j} \tag{2.5}$$

$$V_r = V\cos(\beta)\vec{i} + (V\sin(\beta) - a_r r)\vec{j} \tag{2.6}$$

$$\beta_f = \tan^{-1}\left(\frac{V\sin(\beta) - a_f r}{V\cos(\beta)}\right) = \beta - \tan^{-1}\left(\frac{a_f r\cos(\beta)}{V}\right) \tag{2.7}$$

$$\beta_r = \tan^{-1}\left(\frac{V\sin(\beta) - a_r r}{V\cos(\beta)}\right) = \beta - \tan^{-1}\left(\frac{a_r r\cos(\beta)}{V}\right) \tag{2.8}$$

$$\alpha_f = \beta_f - \delta_f \tag{2.9}$$

$$\alpha_r = \beta r \tag{2.10}$$

At any given state of β and r, front and rear tire slip angles were calculated using Eqs. (2.7) through (2.10). The slip angles were then used in the tire force model, Eq. (2.4), to generate the tire forces, F_f and F_r. These forces were then

24

used in the state equations, Eq. (2.3), to determine the time gradients of both state variables. Numerical integration was preformed to determine the propagation of the state variables from any given initial condition.

2.1.1   Bifurcation in steer

Using the vehicle parameters presented in the literature [18], specifically $a_f = 1.2m$, $a_r = 1.3m$, $I_z = 3000kgm^2$, $V = 20\ m/s$, and $m = 1500kg$, the phase portrait at 0 radians of front steer angle is shown in Figure 2.5. These phase portraits describe the propagation of the states for a relatively wide range of initial states. Each trajectory begins at the blue x's (the initial state) and propagates through time. The red o's represent solutions for equilibrium points. Equilibrium solutions are the roots of the state space equations. In other words, they are states where Eq. (2.3) equals zero ($\dot{\beta} = \dot{r} = 0$). In this portrait, a stable equilibrium solution at $\beta = 0$ and $r = 0$ clearly exists. Stability of this solution can be qualitatively determined as multiple trajectories propagate toward this point. There also exists two saddle point equilibrium solutions.

Figure 2.6 shows the phase portrait at 0.015 radians of front steer angle. The stable equilibrium point has migrated towards a positive yaw rate and a negative vehicle sideslip. All three equilibrium points are still present. At 0.030 radians of front steer (Figure 2.7), the stable equilibrium point and one saddle point have disappeared, leaving only the other saddle point. This represents a bifurcation with respect to steer angle somewhere between 0.015 and 0.030 radians. A bifurcation is a qualitative change in the system with respect to a certain variable. In this case, the qualitative change was a loss of two equilibrium solutions. Physical interpretations of the bifurcations are discussed in Chapter 4. All trajectories

were solved using an ODE solver in Matlab.

Figures 2.8 and 2.9 are the bifurcation diagrams for front steer angle as the varying parameter. Figure 2.8 shows the values of sideslip, β, for each of the equilibrium points in the phase portrait as δ_f is varied. Figure 2.9 shows the corresponding diagram for yaw rate, r, as δ_f is varied. Stable equilibrium solutions are identified in blue, and non-stable points (saddle points in this case) are identified in red. At a front steer angle of 0 radians, there are three equilibrium points. As front steer angle is increased the stable point and one saddle point converge and disappear forming a saddle node bifurcation [17]. As front steer angle is increased past the bifurcation point, only one saddle point remains.
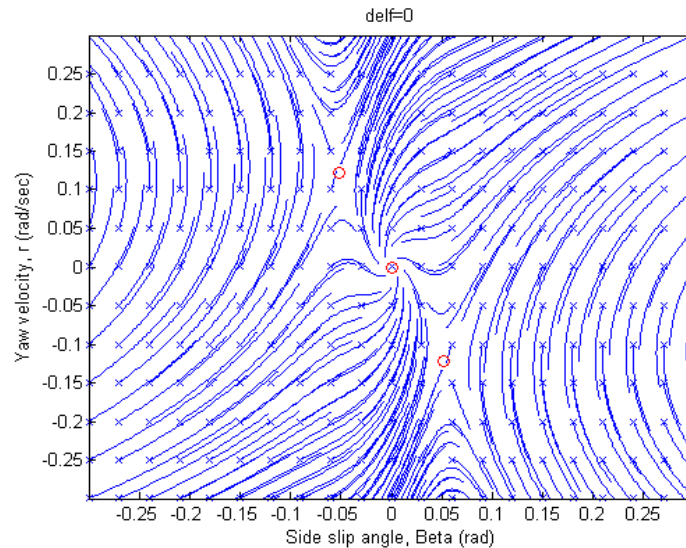
Figure 2.5: Phase portrait for bicycle model at $\delta_f = 0$ radians and $V = 20$ m/s.
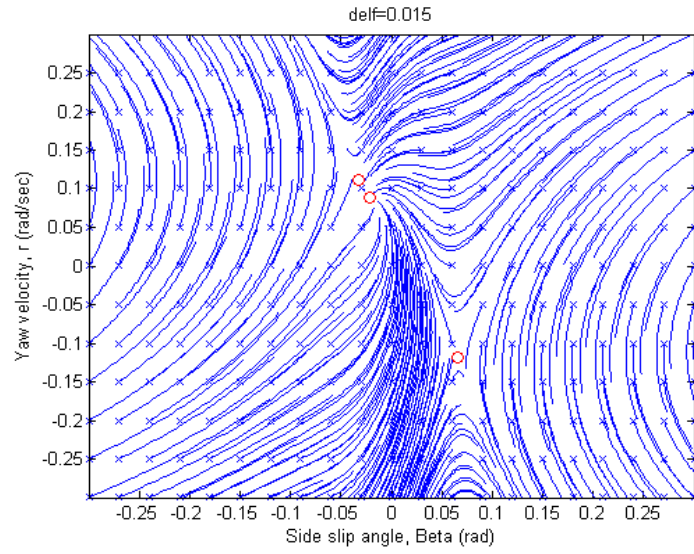
Figure 2.6: Phase portrait for bicycle model at $\delta_f = 0.015$ radians and $V = 20$ m/s.
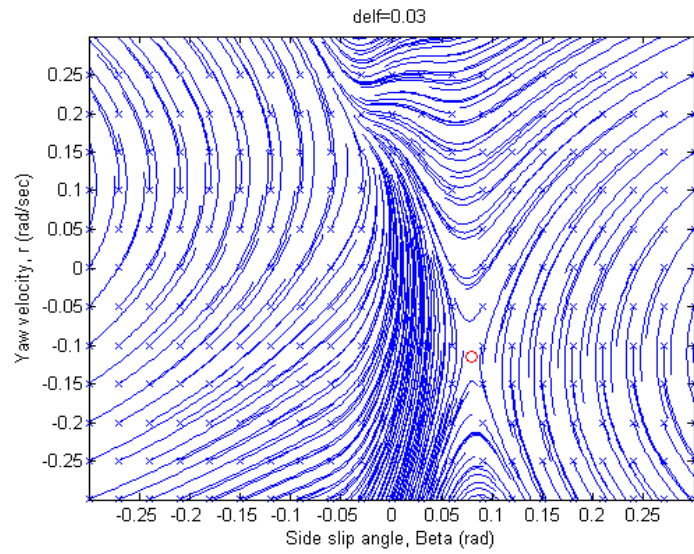
Figure 2.7: Phase portrait for bicycle model at $\delta_f = 0.030$ radians and $V = 20$ m/s.
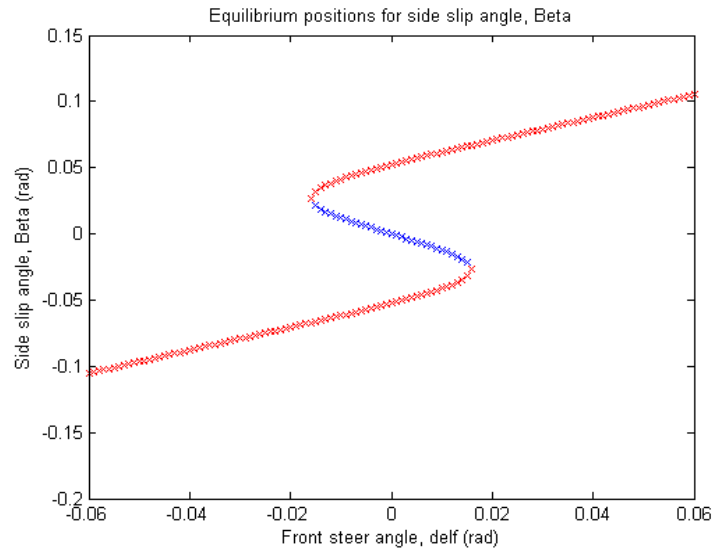
Figure 2.8: Bicycle model bifurcation diagram. Equilibrium values of β versus steer angle.
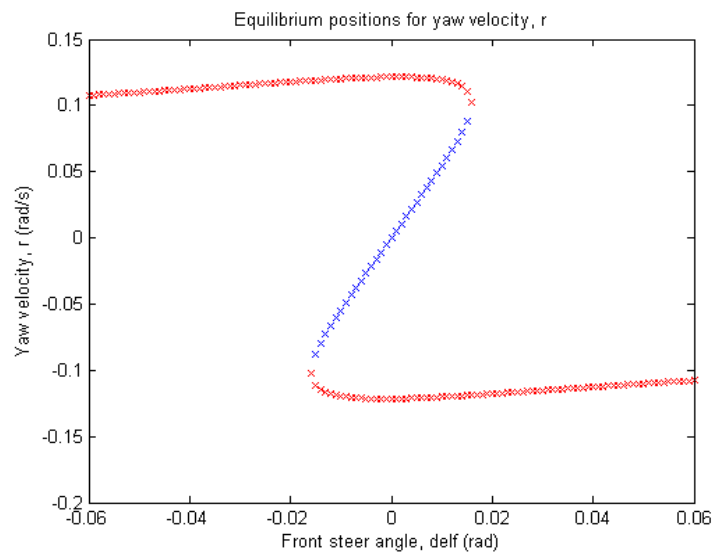
Figure 2.9: Bicycle model bifurcation diagram. Equilibrium values of r versus steer angle.

2.1.2 Bifurcation in velocity

A similar bifurcation analysis was done in this research with velocity as the control parameter. Setting δ_f to 0.015, the velocity (V) was varied. Figure 2.10 shows the phase portrait at $V = 10 \ m/s$. As before, trajectories begin at the blue x's and propagate through time. Equilibrium points are designated as red o's. At $\delta_f = 0$ and $V = 10 \ m/s$ there exists the three equilibrium points, as before. At the same steer angle with velocity increased to $20 \ m/s$, the equilibrium points begin to migrate (Figure 2.11). As velocity is increased further, a bifurcation (similar to the one seen with increased steer angle) occurs. Figure 2.12 shows the phase portrait at $V = 30 \ m/s$. The stable and one saddle node equilibrium point converged and disappeared, leaving only the other saddle node equilibrium point. Figures 2.13 and 2.14, are the bifurcation diagrams with velocity as the control parameter. Again the red points designate unstable equilibrium points and the blue points are stable.
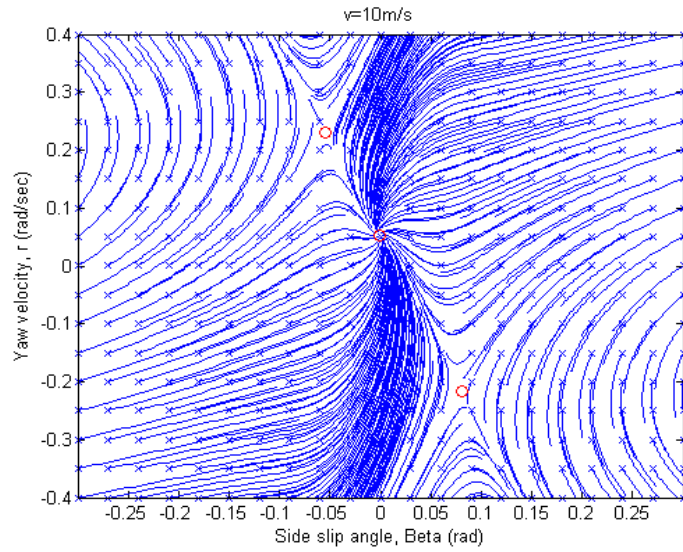
Figure 2.10: Phase portrait for bicycle model at $V = 10\ m/s$ and $\delta_f = 0.015$ radians.
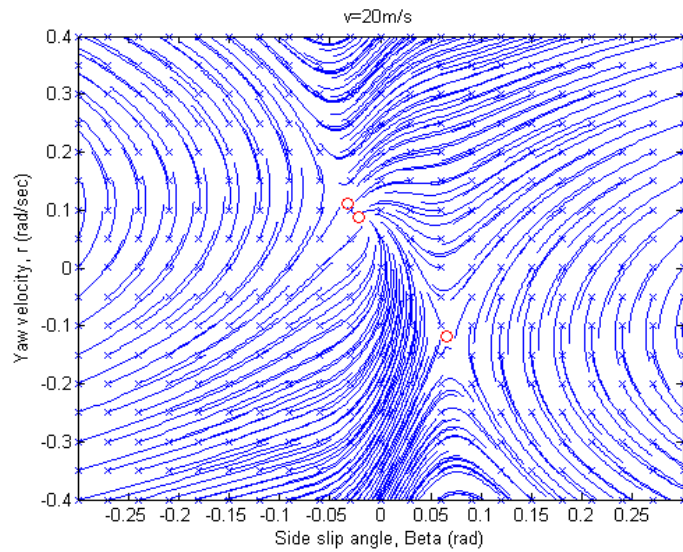
Figure 2.11: Phase portrait for bicycle model at $V = 20\ m/s$ and $\delta_f = 0.015$ radians.

Figure 2.12: Phase portrait for bicycle model at $V = 20\ m/s$ and $\delta_f = 0.015$ radians.
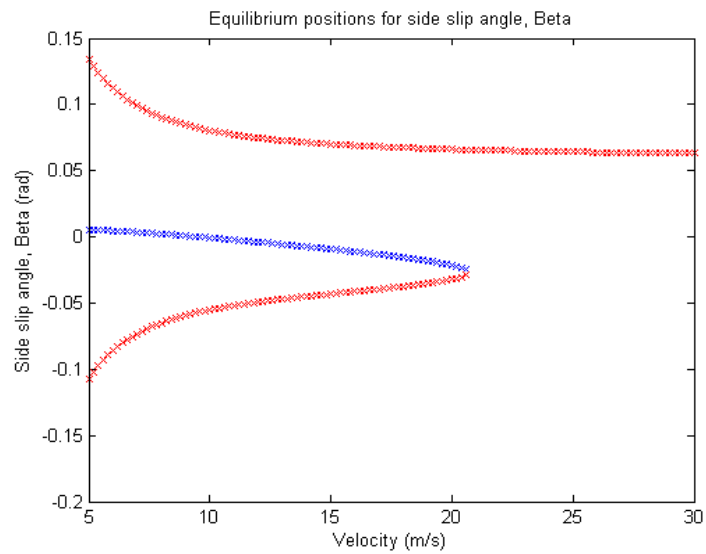
Figure 2.13: Bicycle model bifurcation diagram. Equilibrium values of β versus velocity.
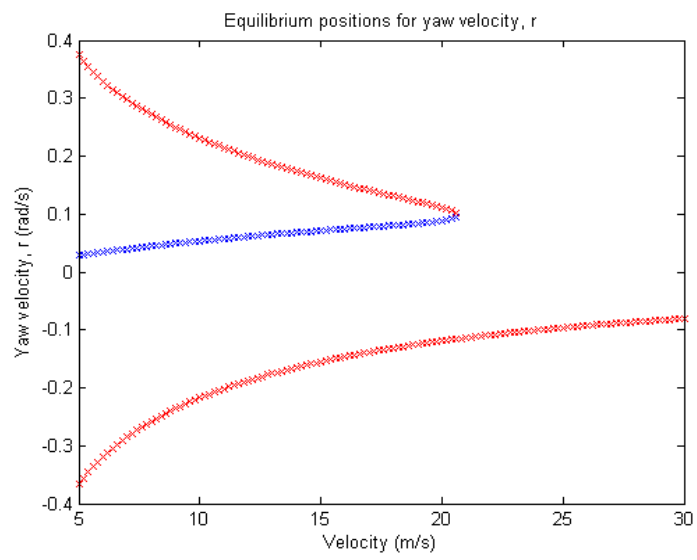
Figure 2.14: Bicycle model bifurcation diagram. Equilibrium values of r versus velocity.

2.2 Tandem-axle model
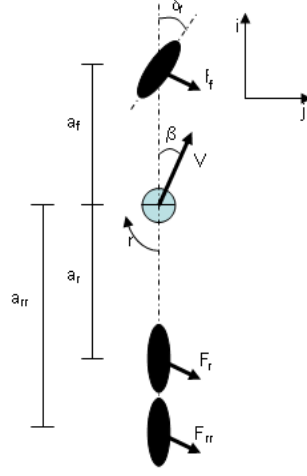
Figure 2.15: SAE representation of bicycle model for a tandem-axle vehicle.

The previous analysis was extended in this research to different vehicle configurations, including tandem-axle vehicles. Tandem axles are normally found on heavier trucks to distribute the rear load over multiple axles. Figure 2.15 shows the bicycle model of a tandem-axle vehicle using SAE coordinates.

Again, all tire forces were oriented perpendicular to vehicle velocity. The representative state equations are given in Eq. (2.11). All tire slip angles were resolved in the same fashion as the two-axle bicycle model. Eq. (2.12) gives the slip angle for the rearmost axle. Rear tire force, F_{rr} was determined using the same tire force model as in the two-axle case.

$$\begin{pmatrix} \dot{\beta} \\ \dot{r} \end{pmatrix} = \begin{pmatrix} \frac{F_f + F_r + F_{rr}}{mv} - r \\ \frac{(a_f F_f - a_r F_r - a_{rr} F_{rr})cos(\beta)}{I_z} \end{pmatrix} \tag{2.11}$$

$$\alpha_{rr} = \beta - tan^{-1}\left(\frac{a_{rr} r cos(\beta)}{V}\right) \tag{2.12}$$

For the numerical analysis, the tandem-axle vehicle was based on the previous two-axle model in terms of vehicle parameters. This was done for comparison and validation of the model results. The distance from the center of gravity to the rearmost axle, a_{rr}, was set to $1.6m$. Initially, the rear tire force parameters from the two-axle model were used for both tandem axles. However, rear force saturation was not evident, since effective rear force was doubled (the rear stabilizing moment was more than doubled). Consequently, the original tire data was altered by halving the scaling term D for both the rear axles. This allowed overall magnitude for each tire to be scaled down while maintaining curve shape. Table 2.2 shows the new parameters used for the tires in the tandem-axle model.

Table 2.2: Tandem-axle bicycle model tire parameters.

	B	C	D	E
Front	11.275	1.56	-2574.7	-1.999
Rear	18.631	1.56	**-874.85**	-1.7908

Holding all other vehicle parameters the same, and setting $\delta_f = 0.015 \ rad$, Figures 2.16, 2.17, and 2.18 show the phase portraits of the system at three different speeds. Even though the total rear forces were about the same as in the two-axle bicycle model, the bifurcation point changed. This was because the system now had an additional rear axle which produced a slightly better stabilizing moment. As compared to the original system, higher velocities were achieved before the phase portrait showed a qualitative change from three equilibrium points to a single point.

Bifurcation diagrams were also generated for the tandem-axle case. Figures 2.19 and 2.20 show the bifurcation diagrams with steer angle as the control parameter.

Velocity was set to 35 m/s. The bifurcation diagrams are characteristically similar to the original system.
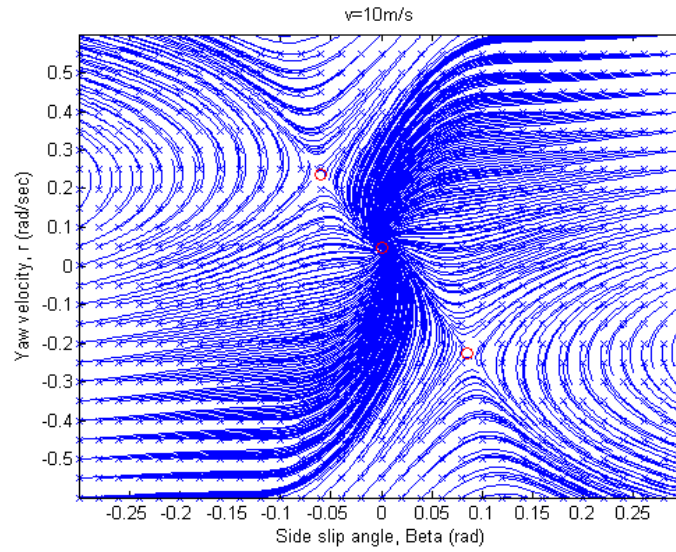
Figure 2.16: Phase portrait for tandem-axle model at $V = 10 \ m/s$ and $\delta_f = 0.015$ radians.
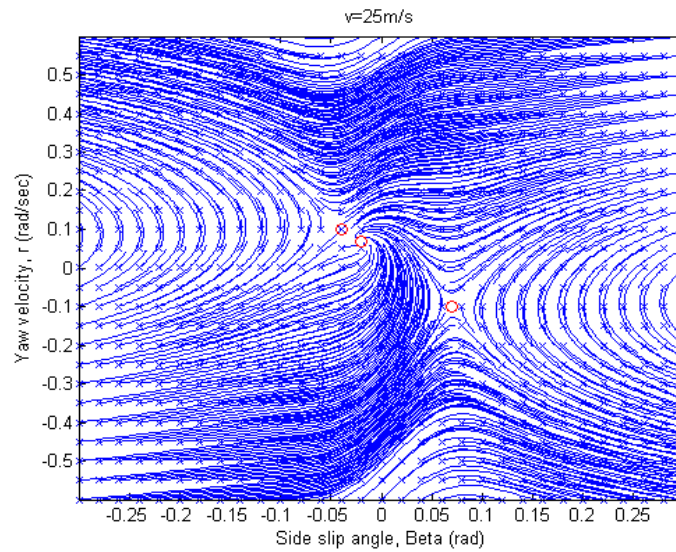
Figure 2.17: Phase portrait for tandem-axle model at $V = 25\ m/s$ and $\delta_f = 0.015$ radians.

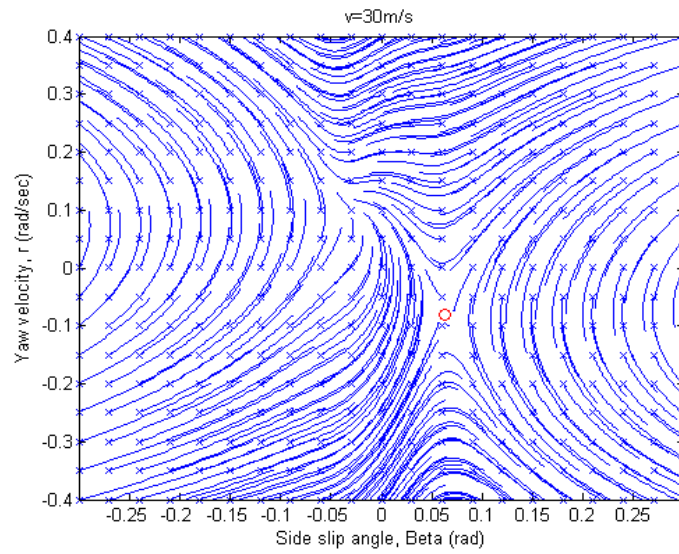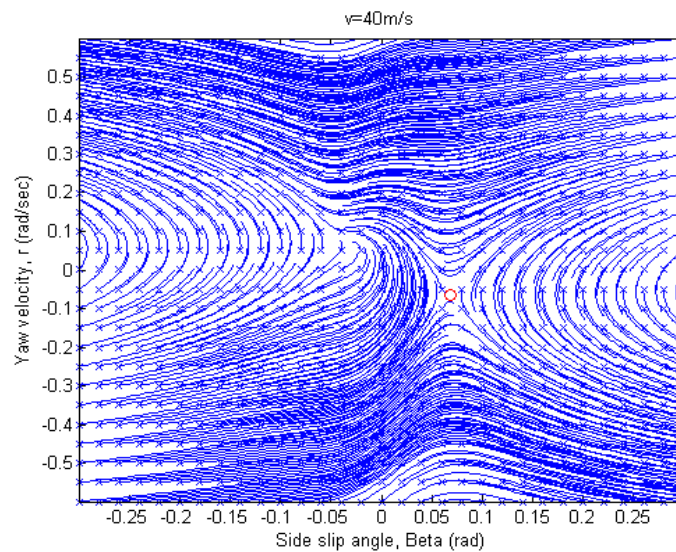Figure 2.18: Phase portrait for tandem-axle model at $V = 40\ m/s$ and $\delta_f = 0.015$ radians.
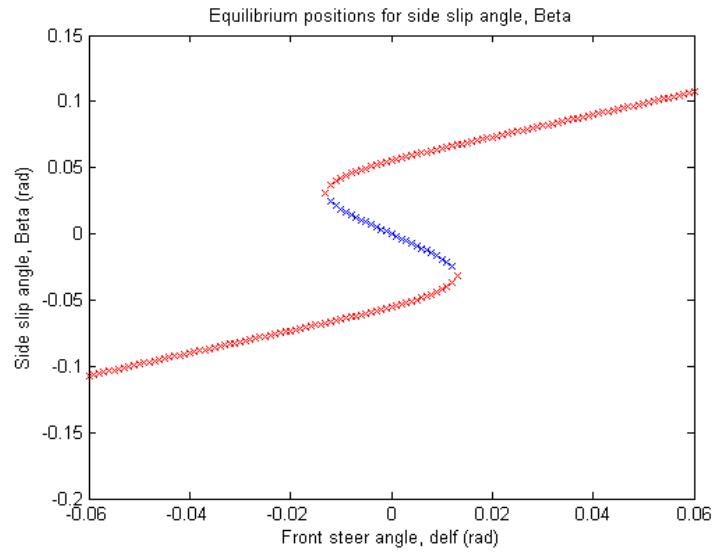
Figure 2.19: Bicycle model bifurcation diagram. Equilibrium values of β versus front steer angle.

Figure 2.20: Bicycle model bifurcation diagram. Equilibrium values of r versus front steer angle.

2.3   Four-wheel model
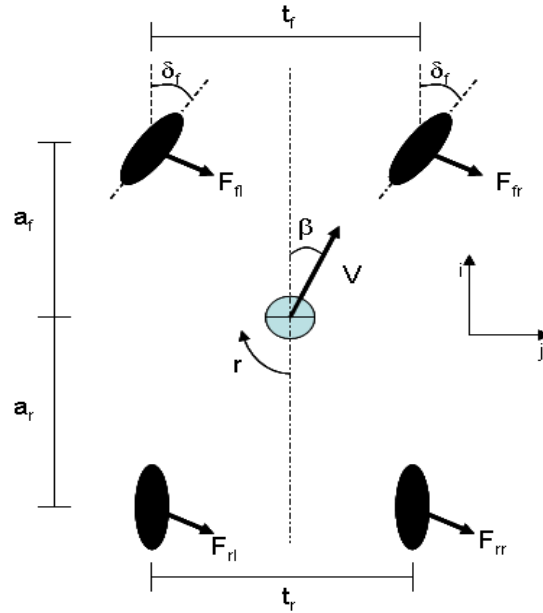
Figure 2.21: SAE representation of the 4 wheel model.

The original bicycle model was also extended to a four-wheel model, as a first step in the development of the vehicle model used in Chapter 3. In the bicycle model, errors were induced by characterizing the tire forces at each axle based on average slip angles. In the four-wheel model, individual wheel velocities and directions were calculated, allowing individual wheel slip angles to be used to calculate individual tire forces. The tire forces were then applied at the true tire location, accounting for the full geometry of the vehicle.

The four-wheel case does not share the same symmetry characteristics as the bicycle model, therefore equivalence did not exist between the SAE standard coordinate system and the coordinates used by Ono. Consequently, the coordinates were defined according to the SAE standard (Figure 2.21). Two additional vehicle

parameters were introduced, t_f and t_r, the front and rear track widths. Individual tire forces, sideslips and slip angles are distinguished with the subscripts fl , fr, rl, and rr, referring to the front left, front right, rear left, and rear right corners.

Eqs. (2.13), (2.14), (2.15), and (2.16) show the formulation of the individual sideslips. Eqs. (2.17), (2.18), (2.19), and (2.20) define the slip angles at each the wheel. Tire force was again based solely on slip angle and was determined using Eq. (2.4). Tire forces were taken as perpendicular to the velocity at each of the individual tires, rather than perpendicular to the velocity at the CG (as was done in earlier). This change removed a small yaw rate (r) assumption used in the bicycle models. Note that real-world tire force data is measured perpendicular to the tire velocity.

$$\beta_{fr} = tan^{-1} \left(\frac{V sin(\beta) + a_f r}{V cos(\beta) - \frac{t_f}{2} r} \right) \tag{2.13}$$

$$\beta_{fl} = tan^{-1} \left(\frac{V sin(\beta) + a_f r}{V cos(\beta) + \frac{t_f}{2} r} \right) \tag{2.14}$$

$$\beta_{rr} = tan^{-1} \left(\frac{V sin(\beta) - a_r r}{V cos(\beta) - \frac{t_r}{2} r} \right) \tag{2.15}$$

$$\beta_{rl} = tan^{-1} \left(\frac{V sin(\beta) - a_r r}{V cos(\beta) + \frac{t_r}{2} r} \right) \tag{2.16}$$

$$\alpha_{fr} = tan^{-1} \left(\frac{V sin(\beta) + a_f r}{V cos(\beta) - \frac{t_f}{2} r} \right) - \delta_f \tag{2.17}$$

$$\alpha_{fl} = tan^{-1} \left(\frac{V sin(\beta) + a_f r}{V cos(\beta) + \frac{t_f}{2} r} \right) - \delta_f \tag{2.18}$$

$$\alpha_{rr} = tan^{-1} \left(\frac{V sin(\beta) - a_r r}{V cos(\beta) - \frac{t_r}{2} r} \right) \tag{2.19}$$

$$\alpha_{rl} = tan^{-1} \left(\frac{V sin(\beta) - a_r r}{V cos(\beta) + \frac{t_r}{2} r} \right) \tag{2.20}$$

Removing the small r assumption and resolving the individual forces required more complicated system equations, given by Eqs. (2.21) and (2.22). The four-

wheel model parameters were again based on the two-axle bicycle model. As with the tandem-axle model, the four-wheel model was initially constructed for direct comparison to the original bicycle model by keeping all of the parameters the same (or at least roughly equivalent). This was done to help validate the four-wheel model results. The front or rear tire force coefficients were used for both tires on each axle, with the scaling factor D halved. This created approximately the same total axle force for front and rear axles while accounting for the different slip angles for the left and right sides. Table 2.3 shows the tire parameters used for the four-wheel model.

$$mv \left(\frac{d}{dt}\beta + r \right) = F_{fr}cos(\beta_{fr} - \beta) + F_{fl}cos(\beta_{fl} - \beta)$$
$$+F_{rr}cos(\beta_{rr} - \beta) + F_{rl}cos(\beta_{rl} - \beta) \qquad (2.21)$$

$$I_z \frac{d}{dt}r = F_{fr} \left(\sqrt{a_f^2 + (\frac{t_f}{2})^2} sin \left(\frac{\pi}{2} - \beta_{fr} + tan^{-1} \left(\frac{t_f/2}{a_f} \right) \right) \right) \qquad (2.22)$$
$$+F_{fl} \left(\sqrt{a_f^2 + (\frac{t_f}{2})^2} sin \left(\frac{\pi}{2} - \beta_{fl} - tan^{-1} \left(\frac{t_f/2}{a_f} \right) \right) \right)$$
$$-F_{rr} \left(\sqrt{a_r^2 + (\frac{t_r}{2})^2} sin \left(\frac{\pi}{2} + \beta_{rr} + tan^{-1} \left(\frac{t_r/2}{a_r} \right) \right) \right)$$
$$-F_{rl} \left(\sqrt{a_r^2 + (\frac{t_r}{2})^2} sin \left(\frac{\pi}{2} + \beta_{rl} - tan^{-1} \left(\frac{t_r/2}{a_r} \right) \right) \right)$$

Keeping all vehicle parameters the same and setting $t_f = t_r = 1.2m$, $\delta_f = 0.0154 \, rad$ and varying V, Figures 2.22, 2.23, and 2.24 show the four-wheel model phase portraits. Figures 2.25 and 2.26 show the associated bifurcation diagrams. As before, there exists a saddle node bifurcation as velocity is increased.

The results were very similar to the two-axle bicycle model. The four-wheel model does, however, offer several advantages over the standard bicycle model. Individual tire slip angles are generated, thereby reducing errors that may be caused

Table 2.3: 4 wheel model tire parameters.

	B	C	D	E
Front	11.275	1.56	**-1287.4**	-1.999
Rear	18.631	1.56	**-874.85**	-1.7908

by averaging the slip angles when using nonlinear tire force functions. Forces are now taken in directions perpendicular to the velocity at the tire, removing the small r assumption. Tire forces are also taken at their individual locations accounting for vehicle track width geometry. Axle force models (as used in the bicycle model) may also be difficult to obtain in relation to a single slip angle, and are at best approximations based on individual tire data. The four-wheel model lends itself to more practical application, since it allows for individual tire force generation. Also, individual tire data is more commonly available. This four-wheel model was the basis for the more advanced real-world models presented in the next chapter.
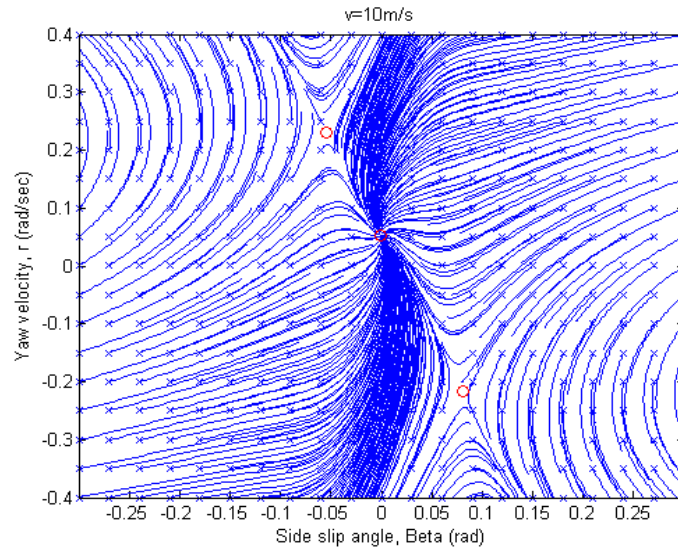
Figure 2.22: Phase portrait for 4 wheel model at $V = 10 \ m/s$ and $\delta_f = 0.015$ radians.
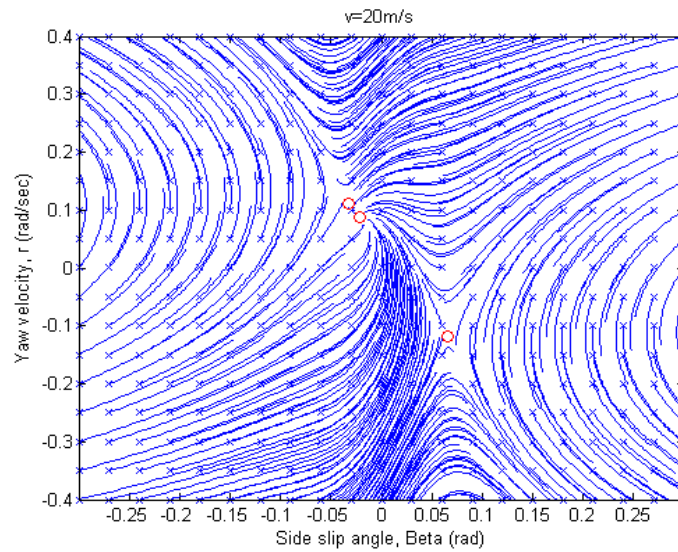
Figure 2.23: Phase portrait for 4 wheel model at $V = 20 \ m/s$ and $\delta_f = 0.015$ radians.
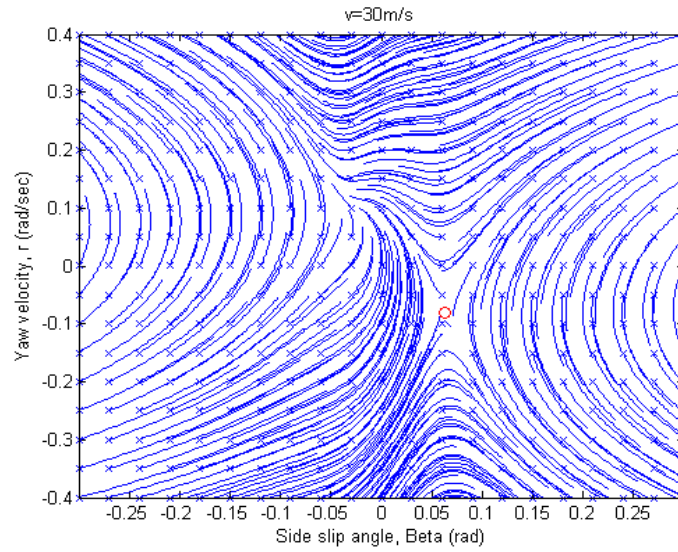
Figure 2.24: Phase portrait for 4 wheel model at $V = 30\ m/s$ and $\delta_f = 0.015$ radians.

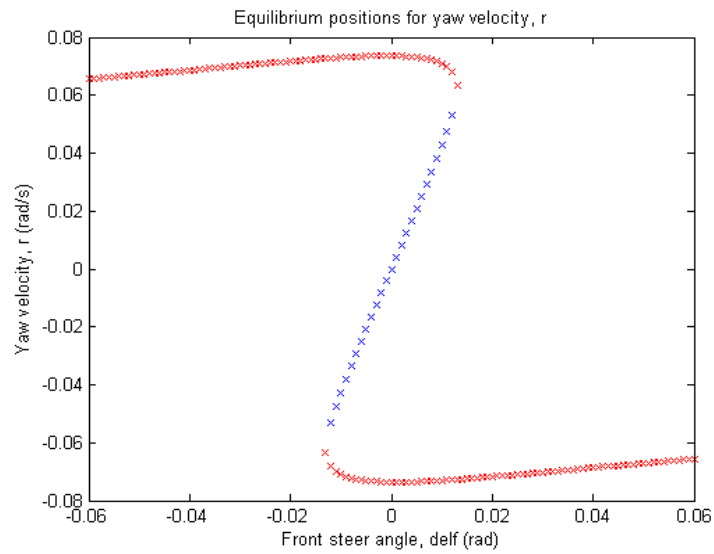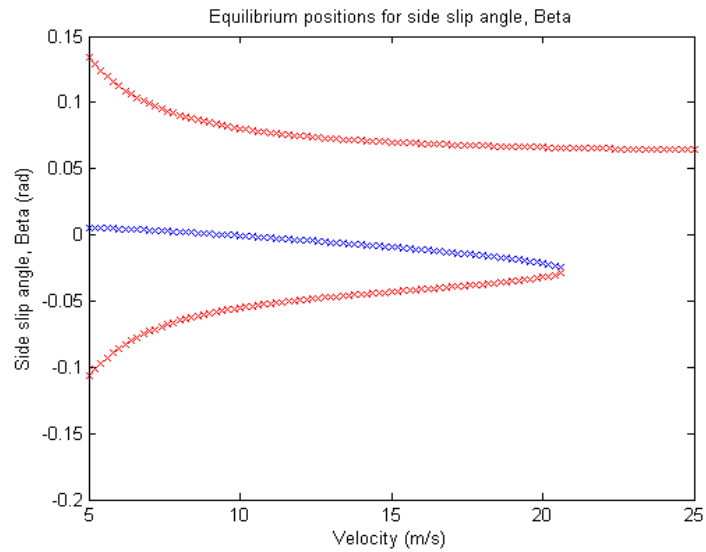Figure 2.25: Bicycle model bifurcation diagram. Equilibrium values of β versus speed.
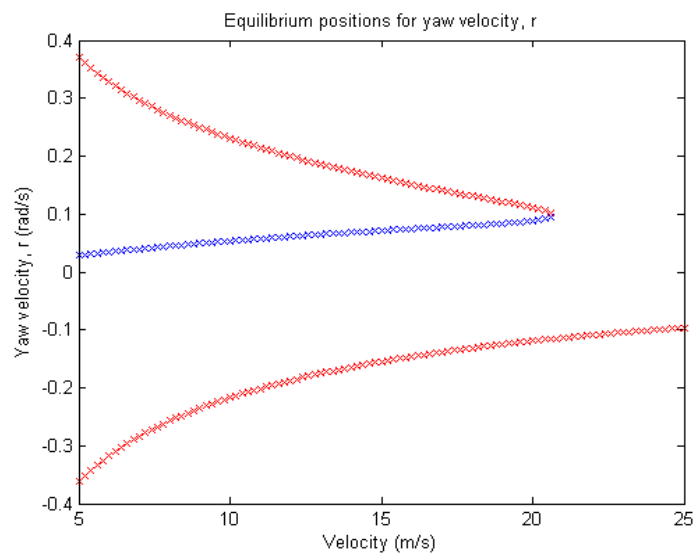
Figure 2.26: Bicycle model bifurcation diagram. Equilibrium values of r versus speed.

44

Chapter 3

LTV model

The four-wheeled model introduced in Chapter 2 removed some of the limitations of the original bicycle model, in that the tire data for the bicycle model needed the effects of weight transfer and differences in right and left tire slip angles embedded in the data. In practice, this is not easy to achieve. Because the four-wheel model uses true tire data (as tested on a tire test rig), the four-wheel model is more easily and accurately applied to real-world vehicles.

This chapter applies the four-wheel model to a Light-Duty Utility Military Tactical Vehicle (LTV), and extends the analysis over a broad range of the state space. The LTV was selected because extensive handling tests of over-weighted LTVs were recently conducted at the U.S. Army Aberdeen Test Center (ATC), which provided key vehicle and tire data. It was anticipated that this work might support and help explain the findings of the testing at ATC. In addition, development of an accurate and easily generated math model allows vehicle stability to be evaluated at all conceivable payload conditions, without the need for extensive and potentially dangerous field tests at the limits of performance. Lastly, a four-wheel model with lateral weight transfer is presented and briefly discussed.

3.1 Tire Model

The first step in creating a vehicle model is developing a realistic tire model. The tire model used by Ono *et al.* [18] was a very general form of a semi-empirical tire model commonly refereed to as "The Magic Tire Formula". A more advanced version of this formulation was used in the current LTV model. The new formulation allowed tire force to be characterized by both slip angle and vertical load (as opposed to slip angle alone) from a limited set of tire data obtained under specific loading conditions. The improved tire model also allowed for the creation of more complicated vehicle models that included roll motions and dynamic lateral loading conditions of the tires.

The following sections of the paper present the general formulation of the Magic Tire formula, a genetic algorithm for coefficient optimization, and a means to overcome shortfalls in the range of the available test data. More specifically, guidelines are presented to extend tire data limited below saturation to regions beyond saturation.

3.1.1 The Magic Tire Formula

The initial tire model considered for the LTV model used the full version of the magic tire formula [19]. This semi-empirical formula is regarded as the foremost tire force model for vehicle dynamic simulations to date [20], and has been shown to very accurately represent tire data [13] [3] [19]. The model used for this simulation was a pure slip model for tire lateral force, whereby tire lateral force was defined as a function of normal load and slip angle. Camber and combined longitudinal and lateral slip effects were neglected.

The Magic Tire Formula is re-written in general terms in Eq. (3.1), where X can

represent either longitudinal slip ratio or lateral slip angle, and Y represents the corresponding longitudinal or lateral forces. An additional offset term, Eq. (3.2) can also be included. The Magic Tire Formula produces the classic "S-shaped tire curves as shown in Figure 3.1.

$$y(x) = D \cdot \sin \left[C \cdot \tan^{-1} \left\{ B \cdot x - E \cdot \left(B \cdot x - \tan^{-1}(B \cdot x) \right) \right\} \right] \qquad (3.1)$$

$$Y_{pure}(X) = y(x) + S_v$$

$$x = X + S_h \qquad (3.2)$$
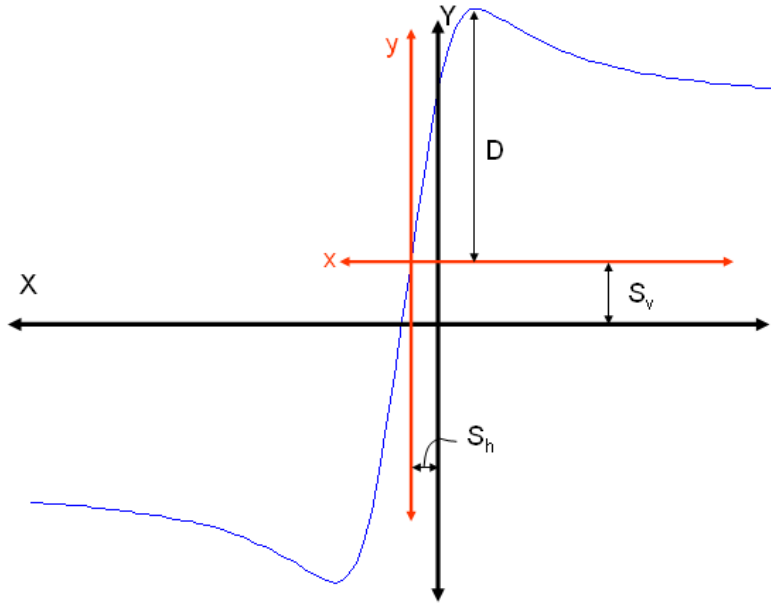
Figure 3.1: General Magic Tire Formula slip curve [19].

The coefficients B, C, D, E, S_h, and S_v are curve fitted parameters that describe the relationship between lateral force and slip angle at a given vertical load. Physically, D represents the maximum slip value, $B \cdot C \cdot D$ represents the

cornering stiffness at low slip angles (slope of the curve near the origin), and S_h and S_v represent offsets due to non-symmetric effects such as ply steer and conicity. C and E are shape factors that do not have obvious physical meaning. Mathematically, C defines the region of influence of the sin function, while E influences the curvature at the peak value [19].

Eq. (3.1) gives force solely as a function of the slip angle. Since tire lateral force is a function of both slip angle and vertical load, Eqs. (3.3) through (3.9) were used to account for vertical load (without camber effects). In the full formulation, the general coefficients, B, C, D, S_h, and S_v, are functions of vertical load, and E is a function of both vertical load and slip angle. There are now 12 coefficients, a_0, a_1, a_2, a_3, a_4, a_6, a_7, a_8, a_9, a_{11}, a_{12}, and a_{17}. These are curve-fitted parameters that capture the relationship of the general coefficients to vertical load. In the complete formulation, tire slip angle and vertical load were used in Eqs. (3.3) through (3.9) with the curve-fitted parameters,a_0, a_1, a_2, a_3, a_4, a_6, a_7, a_8, a_9, a_{11}, a_{12}, and a_{17}, to generate values for the general coefficients, B, C, D, E, S_h, and S_v. The values for the general coefficients were then used in Eqs. (3.1) and (3.2), with the slip angle, to calculate a lateral tire force.

$$D = a_1 \cdot F_z^2 + a_2 \cdot F_z \tag{3.3}$$

$$C = a_0 \tag{3.4}$$

$$B \cdot C \cdot D = a_3 \cdot \sin\left(2 \cdot \tan^{-1}(\frac{F_z}{a_4})\right) \tag{3.5}$$

$$B = (B \cdot C \cdot D)/(C \cdot D) \tag{3.6}$$

$$E = (a_6 \cdot F_z + a_7) \cdot (1 - a_{17} * sgn(\alpha + S_h)) \tag{3.7}$$

$$S_h = a_8 \cdot F_z + a_9 \tag{3.8}$$

$$S_v = a_{11} \cdot F_z + a_{12} \tag{3.9}$$

3.1.2 The genetic optimization algorithm

The 12 magic tire coefficients were fit to empirical tire data. The curve fit was a multi-parameter, single-objective, unconstrained optimization procedure. The optimization procedure converges upon parameter values that minimize the sum of the squared errors between the magic tire formula values and the tire data. A genetic optimization algorithm, developed in [3], was used. This procedure was found to produce accurate results without the need for precise initial guesses, while converging reasonably fast.

Genetic algorithms (GAs) are based on the principle of evolution. A basic GA starts with a set of randomly generated possible solutions. Each possible solution is treated as an individual in a population (the set). The population then goes through a series of selection, reproduction, and mutation processes, with the general tendency toward individuals with preferred solutions. Preferred solutions are solutions that are superior in terms of the objective function. In this case, preferred solutions are solutions that have lower mean squared errors.

Other algorithms considered for use involved items such as sub-populations that evolve somewhat independently, where limited inter-population contact is allowed [14]. These algorithms increase complexity and overall computation time. The more complicated algorithms were tested but did not consistently produce accurate results for this problem.

The curve fit is a multi-parameter optimization, since all 12 coefficients must be optimized for the single objective function. In the GA, each individual is comprised of a single possible solution to the optimization. Therefore, each individual is defined by only 12 values, or genes, one for each of the parameters.

In the algorithm used, each iteration begins with the selection of the best indi-

vidual from the entire population. The algorithm then processes each individual in the population. For each individual, two individuals from the population are randomly selected (population sample) and combined to create a perturbing vector. This perturbation is added to the best individual forming a reproduction candidate. Each individual may have a different reproduction candidate, since each has a different perturbation vector (created from a different population sample). The individual is then potentially crossed (mated) with the reproduction candidate. If crossing occurs, there is a potential for mutations in the genes being passed. The product of the crossing (the child) can then be used to form the subsequent generation.

The entire population is made up of NP individuals. Each individual can be represented as X_i where $i \in [1, NP]$. Each individual X_i, consists of a 12 element vector. $X_{i,j} : j \in [1, 12]$ represents the jth gene or coefficient of the possible solution X_i.

During each iteration, X_{best} represents the best solution in the population. For each individual a sample of two individuals from the population is selected (X_{r1} and X_{r2}). The reproduction candidate is then created by Eq. (3.10). F is a real valued parameter and represents the amount of perturbation applied to X_{best}.

$$V = X_{best} + F \cdot (X_{r1} - X_{r2}) \tag{3.10}$$

Each individual is then potentially crossed with their reproduction candidate. Crossing (mating) occurs with a probability of CP. If crossing occurs, genes are randomly selected (with equal probability) from each parent to form the child. The child is then compared to the original individual. If the child is a preferred solution, the individual is replaced.

If crossing occurs, there is also a possibility of mutation as the genes are passed

from parent to child. MP represents the mutation probability of each gene. For a rapidly converging solution, MP is often chosen to be much less than CP ([3]). When mutation occurs, the gene that is passed is adjusted within a range proportional to the value of the gene. If gene y is passed, and mutation is occurring, Eq. (3.11) represents the equation for the mutated gene, y_m. MR is a real-valued parameter that adjusts the mutation range. The lower the value of MR, the larger the allowed mutation range (compared to the value of the original gene). The expression $rand(i,j)$ represents a random number generated from a uniform random distribution function between values i and j.

$$y_m = y + rand(-y/MR, y/MR) \tag{3.11}$$

Iterations run until the best individual (solution) converges within an acceptable error, the solution does not change within several iterations (algorithm stalled), or the maximum number of iterations is exceeded. For this curve fit, the acceptable error was set very low to allow the algorithm to fully converge. Also, F, CP, MP, and MR were chosen to keep the algorithm from stalling away from the optimal solution. Computational time was not of great significance. So, the run termination was mainly based on the maximum number of iterations. A flowchart depicting the algorithm is shown in Figure 3.2.

For iter = 1 to itermax

Solve Xbest

For i = 1 to NP

Select Xr1 Xr2

Form V

Crossover — No

Yes

For j = 1 to 12

Parent selection (X,V) for gene j

Mutation — No

Yes

Mutate

Create gene j

Child > X — No — Keep X

Yes

Replace X

Next iteration

End
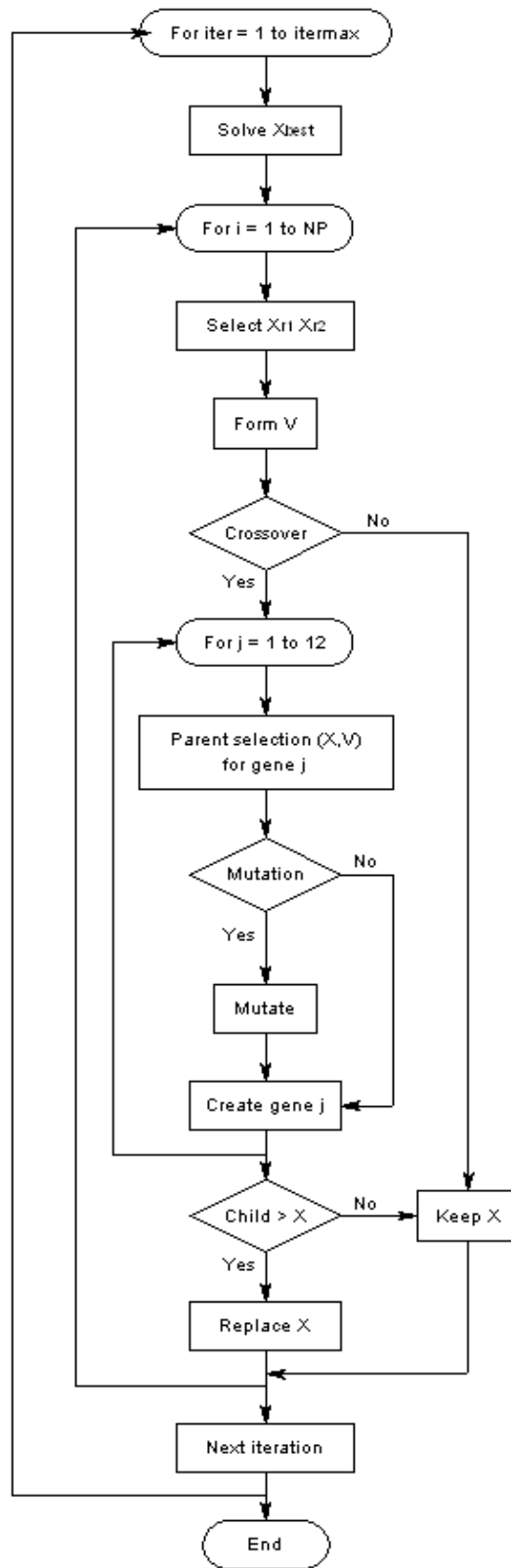
Figure 3.2: GA flowchart.

3.1.3   Results of the algorithm

The algorithm was first tested using data found in the literature [3]. The GA was run with the following parameters: $NP = 50$, $CP = 0.6$, $MP = 0.1$, $F = 0.4$, $MR = 4$, and $itermax = 1000$. Figure 3.3 shows the mean square error of the best individual of the population vs. the number of iterations. Figure 3.4 shows the results from the output of the algorithm versus the actual data. Actual data points are represented in this Figure by the x's, and algorithm results are plotted as solid lines. The algorithm was trained on the lowest and the highest vertical loads. Results for the middle loading condition showed good match to the actual data, demonstrating the accuracy of the formulation as well as the optimization algorithm. The algorithm periodically failed to converge fully. But aside from the obvious qualitatively bad fits, the results were consistent and repeatable in terms of the values of the formula output (often the coefficients would not be exactly the same but formula outputs were consistent).
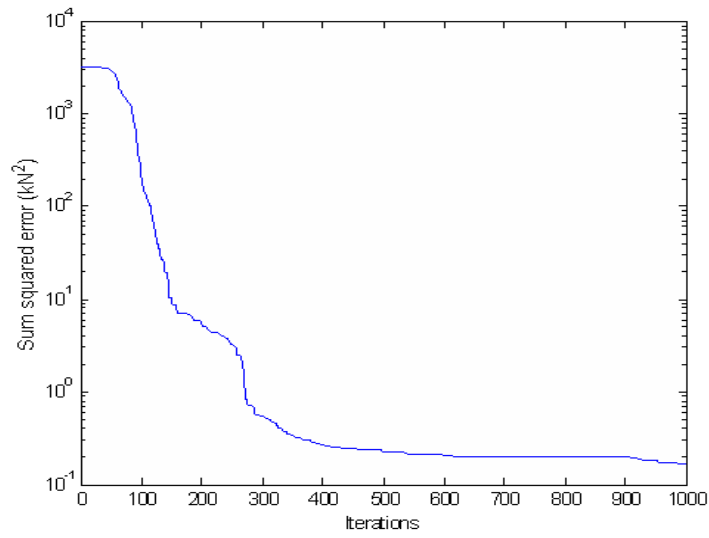
Figure 3.3: Genetic algorithm mean square error vs. iterations.
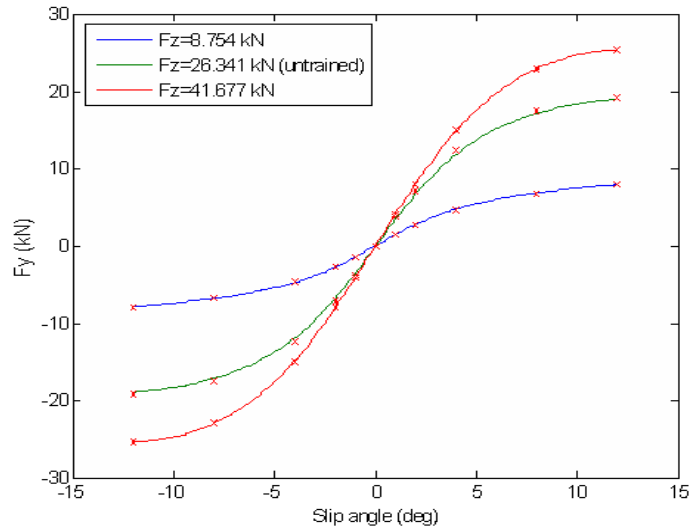
Figure 3.4: Tire force vs. slip angle, GA results.

3.1.4 Modified formulation

In practice, tire data at high slip (peak and past saturation) is not always taken. In addition to being destructive to the tires, excessive wear and inconsistent temperatures make the high slip data less repeatable [22] [21] [20] . Near the friction limit of the tire, forces also become dependent on speed as well as temperature, again leading to unrepeatable data [21] [20]. Nevertheless, lack of high-slip data can lead to unpredictable model behavior at the higher slip angles.

The LTV tire data obtained for this research suffered from this shortfall, in that it generally did not include results up to or beyond tire saturation. Figures 3.5, 3.6 and 3.7 are plots of measured values for lateral tire forces vs. slip angle at several vertical loads, while the actual values are given in Tables 3.1.4, 3.1.4 and 3.1.4. This section describes the approach developed to overcome this shortfall.

Initially all of the curve fits were run with the following parameters: $NP = 50$, $CP = 0.6$, $MP = 0.1$, $F = 0.4$, $MR = 3$, and $itermax = 1000$. The parameters were chosen to provide quick convergence and few occurrences of stalling at poor fit local minimums. The early algorithm produced fairly consistent and well fitting results (low square errors). However, repeatability of lateral force values at higher slip angles (past the slip angle span of the data) was poor. This was attributed to the tradeoff between the parameters C and E, called the shape factors.

For data with limited slip ranges, one shape factor can be traded for the other without affecting fitment of the unsaturated data [21]. Accordingly, C values can be fixed without effecting fitment to the data [21] [23]. Sharp showed when high lateral slip data is unavailable, the creation of a normalized combined slip curve (taking into account both longitudinal and lateral slip) can be eased by setting the C value for lateral force to the value optimized for longitudinal slip [21]. In

Table 3.1: LTV lateral tire force data @ 20 psi.

		Vertical Force (N)					
		14482	12642	10840	9020	7177	5312
Wheel slip	-6.05	7218	7081	6695	6034	5206	3838
angle (deg)	-5.03	6515	6521	6304	5853	5177	4053
	-4.03	5616	5745	5630	5294	4734	3821
	-2.97	4273	4681	4731	4538	4090	3354
	-1.96	2686	3148	3318	3268	3013	2538
	-0.95	1216	1480	1618	1658	1585	1404
	0.02	-378	-284	-227	-163	-115	-61
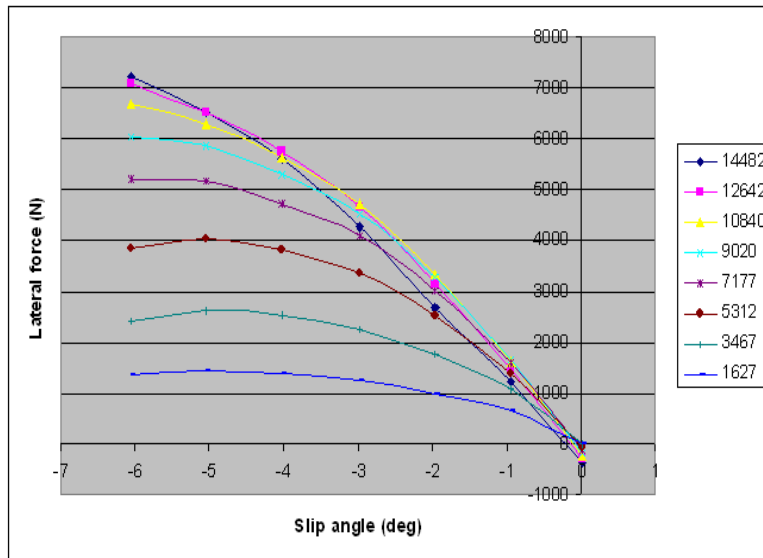
Figure 3.5: LTV tire lateral force vs. slip angle at 20 psi.

Table 3.2: LTV lateral tire force data @ 35 psi.

		Vertical Force (N)							
		21805	19055	16335	13605	10899	8164	5434	2750
Wheel slip	-6.05	9488	9688	9360	8713	7743	6187	3978	1997
angle (deg)	-5.03	8434	8801	8673	8182	7355	5985	3978	1965
	-4.03	7159	7607	7593	7244	6548	5397	3671	1809
	-2.97	5501	6085	6190	5979	5449	4531	3131	1544
	-1.96	3654	4140	4299	4199	3875	3268	2325	1170
	-0.95	1518	1817	1972	1982	1874	1634	1226	696
	0.02	-673	-623	-542	-466	-399	-294	-185	-61
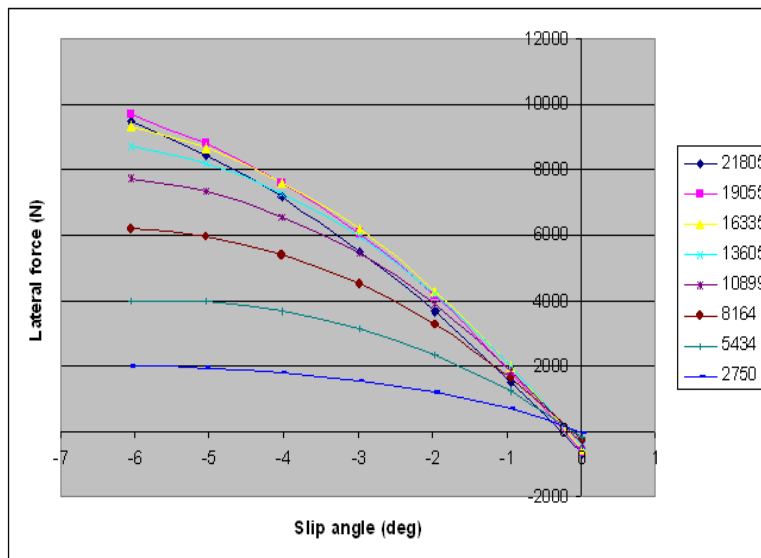
Figure 3.6: LTV tire lateral force vs. slip angle at 35 psi.

Table 3.3: LTV lateral tire force data @ 50psi.

		Vertical Force (N)							
		27744	24263	20809	17345	13861	10406	6966	3503
Wheel slip	-6.05	11853	11926	11497	10674	9393	7452	4846	2357
angle (deg)	-5.03	10625	10900	10643	9966	8821	7100	4751	2292
	-4.03	9217	9488	9329	8762	7793	6353	4300	2108
	-2.97	7217	7574	7535	7145	6409	5270	3608	1778
	-1.96	4859	5217	5273	5048	4549	3764	2640	1319
	-0.95	2050	2305	2418	2387	2191	1873	1397	748
	0.02	-803	-717	-619	-541	-450	-324	-197	-50
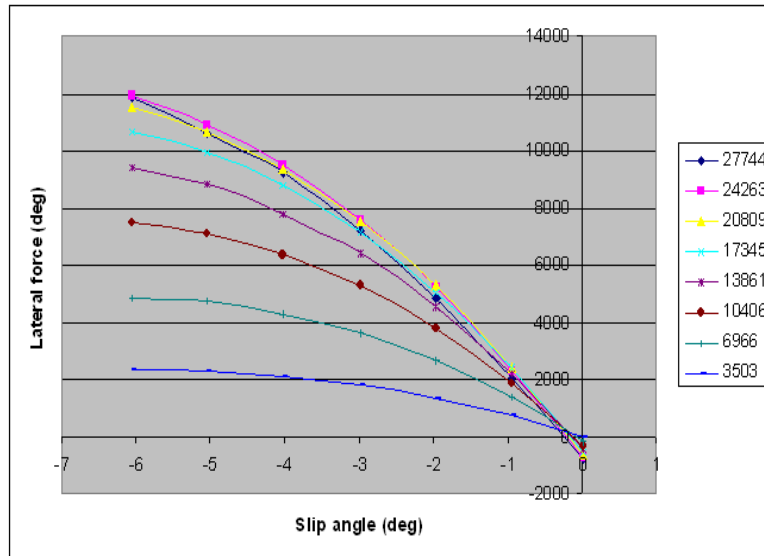
Figure 3.7: LTV tire lateral force vs. slip angle at 50 psi.

this case, since there was no saturation slip data available, a general shape was assumed. In order to provide more consistent results, a typical lateral slip C value of 1.30 was chosen [22].

Figure 3.8 shows the initial algorithm results for lateral force at the highest vertical load and relatively high slip angle (past saturation) for each tire pressure. Figure 3.9 shows the results after holding $C = 1.3$. Both are plotted against the sum of the mean square errors so that the values can be compared against their quality of fit. The y axes are scaled the same to allow direct comparison. The majority of the solutions fell within the $[0, 10]$ kN^2 range for the mean square error. Solutions having a sum square error of less than 10 kN^2 for 56 points (roughly $13N$ error per point) can be said to have very good fits. Both cases show a good clustering of data in terms of fit quality (the majority had very good fit). However, holding $C = 1.3$, only provided marginally better clustering in the high slip values showing marginally better repeatability.

The major issue with the curve fit was that the test data showed some unexpected results for the highest load at each of the tire pressures. Lateral force data were, for some slip angles, lower than those for the lower vertical load conditions. This can be seen in Figures 3.5, 3.6 and 3.7. Figures 3.10 and 3.11 show typical qualitatively poor solutions converged upon by the GA. Fitment to the data was, however, good in both examples. In the full magic tire formulation, E was allowed to change with vertical load. The poor solutions were attributed to the change in E, in order to better fit the data for the highest load condition. Figures 3.12 and 3.13 show the sharp drop in lateral force at the corresponding value for the highest load. Again, this was due to the algorithm attempting to match the unexpected data.
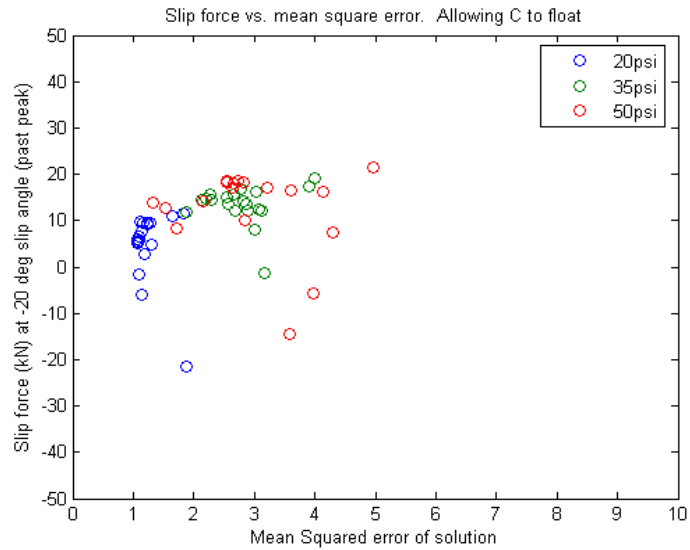
Figure 3.8: Original GA results for lateral force at the highest vertical load tested, performed for 20 runs at each tire pressure.
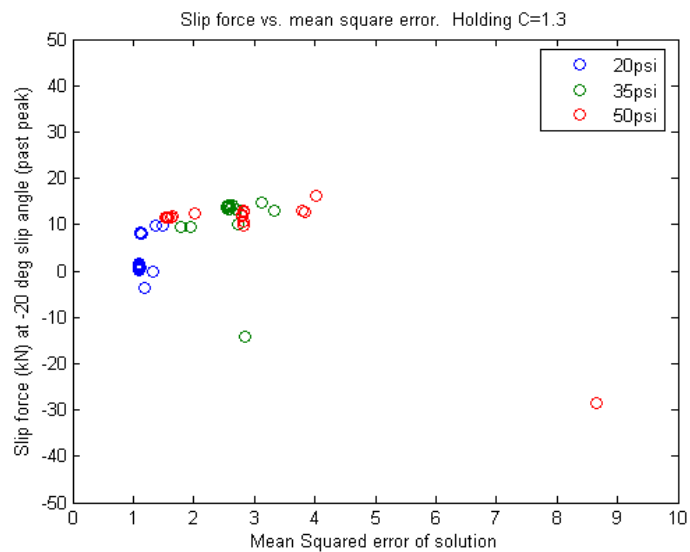
Figure 3.9: GA results when holding $C=1.3$ for lateral force at the highest vertical load tested, performed for 20 runs at each tire pressure.
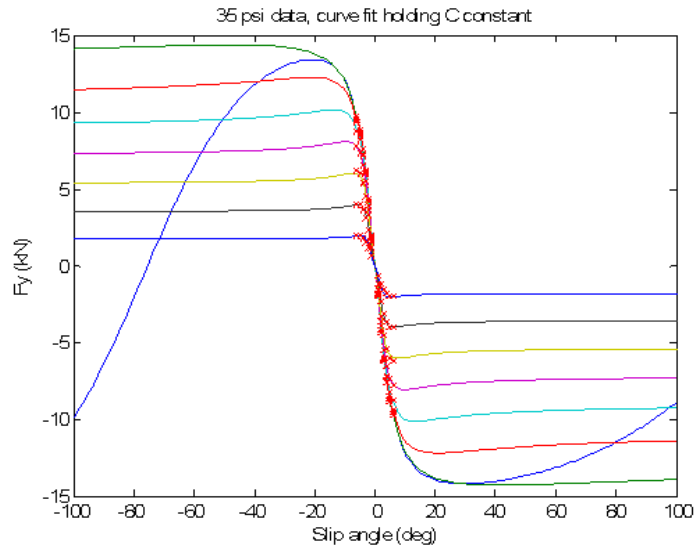
Figure 3.10: Example of undesirable GA solution for 35 psi, C=1.3, E allowed to float according to full tire model formulation.
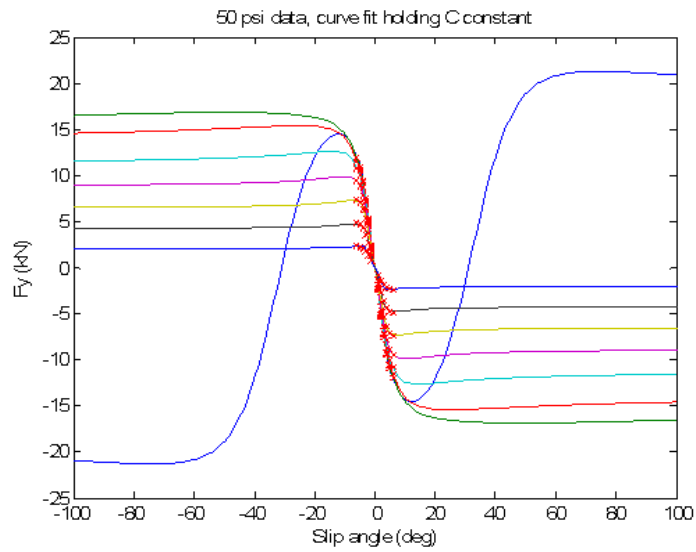
Figure 3.11: Example of undesirable GA solution for 50 psi, C=1.3, E allowed to float according to full tire model formulation.

61
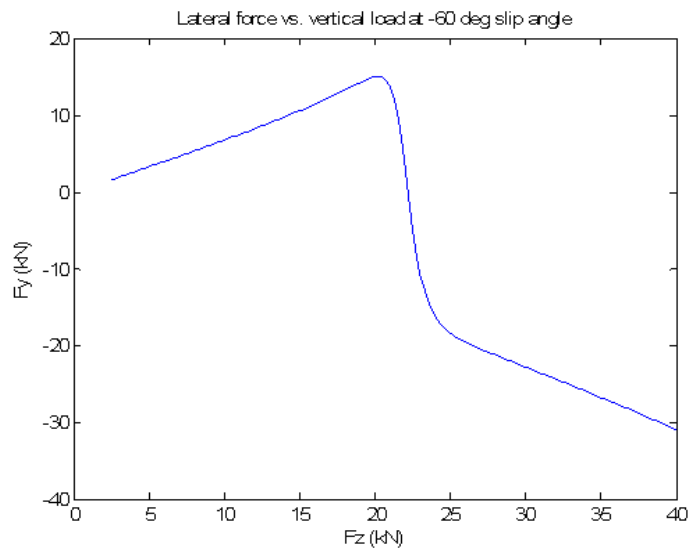
Figure 3.12: Lateral force vs. vertical load for undesirable solution at 35 psi.
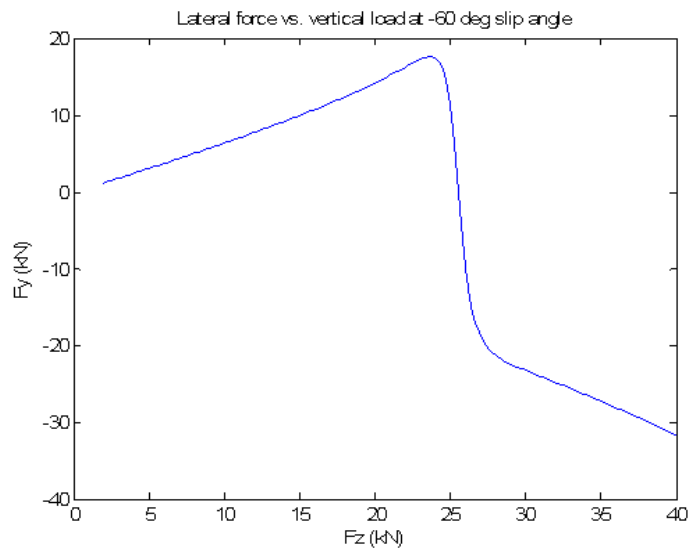
Figure 3.13: Lateral force vs. vertical load for undesirable solution at 50 psi.

If E was allowed to vary with the algorithm, but held as a constant with respect to vertical load and slip angle (in contrast to the magic tire formulation), the shape characteristics were more consistent at the higher slips for all of the loads. A constant E value is used in many formulations of the magic tire formula [22] [23] [21] [20]. In fact, for the normalization procedure for combined slip, the E was not only constant but was set at a certain value determined by the solution of the pure slip cases [22] [23] [21] [20].

Figures 3.14 and 3.15 show the results of the algorithm where $C = 1.3$ and E was constrained to be a constant. Since E was not allowed to vary with load, the shape of the highest load curve was forced to resemble that of the lower load curves. This led to a slightly poorer fit, but more consistent and repeatable results. With a mean squared error of about $4\ kN$ for the 56 points, the fit was still very good. This method was used with similar results for all of the tire pressures. All of the curves generated for the LTV tire model were generated in this fashion.

Figures 3.16 and 3.17 show the curve fits for the data using the modified strategy of setting $C = 1.3$ and constraining E as a constant. Table 3.1.4 summarizes the results of the algorithm for the LTV tire data. The parameter E was optimized as a constant, and no longer followed the full formulation as defined in Eq. (3.3). Instead, E was simply defined as $E = a_6$. In this case a_7 and a_{17} were dummy variables that were not optimizable and did not effect the solution.
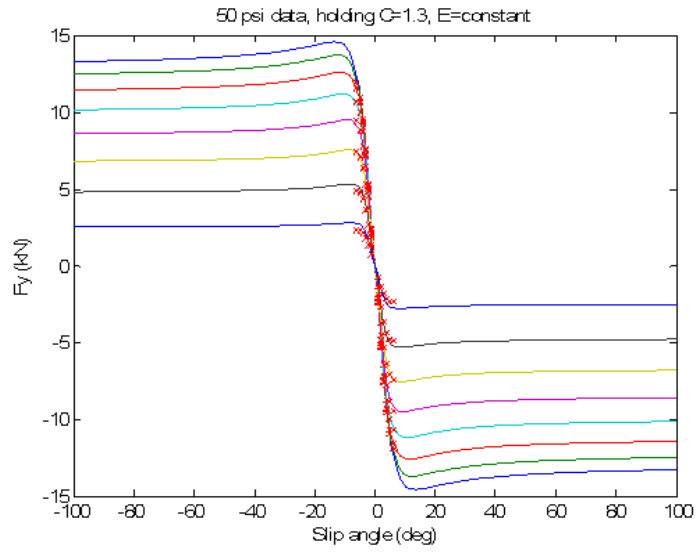
Figure 3.14: Example of a desirable GA solution for 50 psi, C=1.3, E=optmized constant.
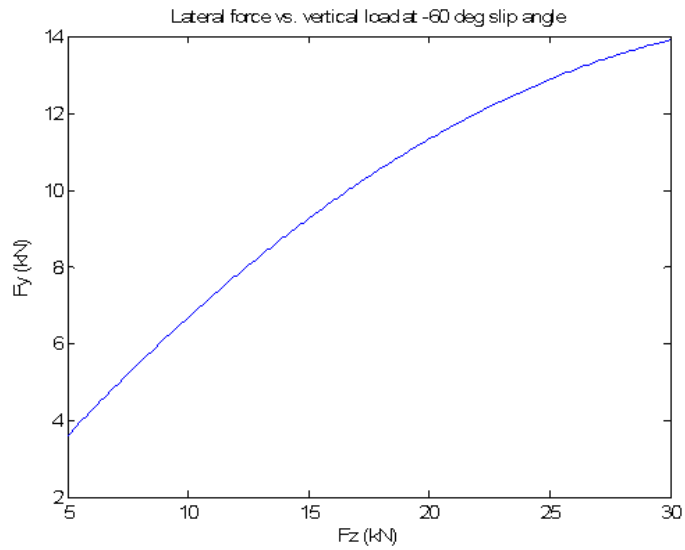
Figure 3.15: Lateral force vs. vertical load for desirable solution at 50 psi.
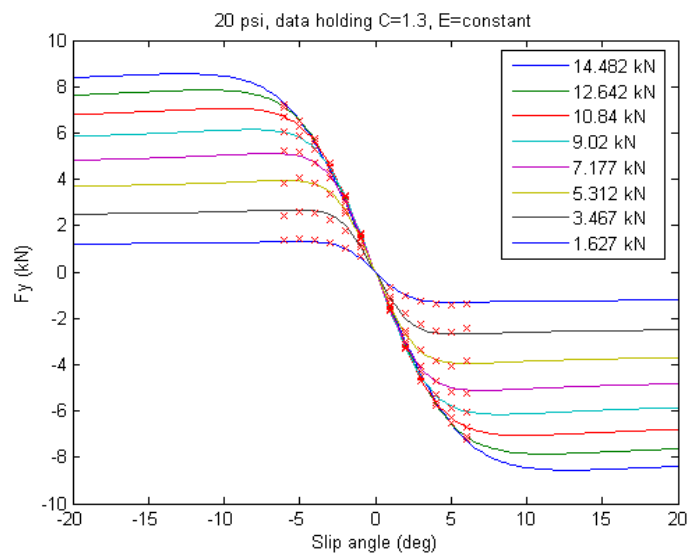
Figure 3.16: Lateral force vs. slip angle for 20 psi data.
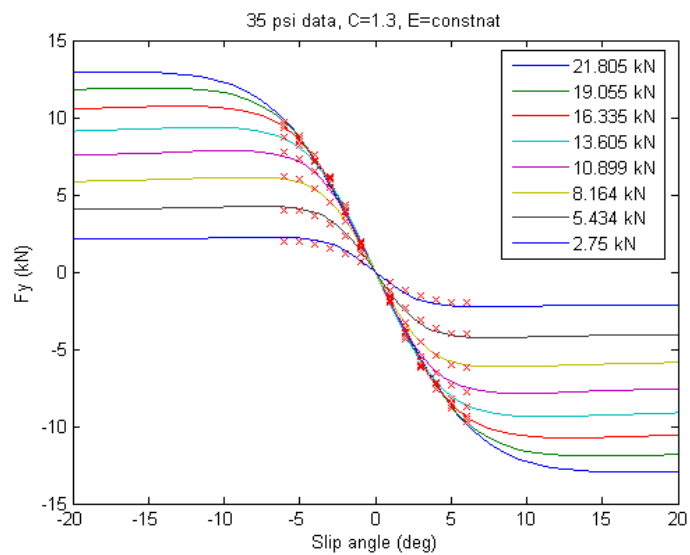
Figure 3.17: Lateral force vs. slip angle for 35 psi data.

65

Table 3.4: LTV GA coefficient results.

	20 psi	35 psi	50 psi
MSE	1.1087	3.2904	4.3422
a_0	1.3000	1.3000	1.3000
a_1	-0.0166	-0.0115	-0.0116
a_2	0.8315	0.8447	0.8460
a_3	97.7925	-123.6505	-152.1290
a_4	-8.9904	14.2730	22.0333
a_6	-1.2362	-0.8073	-1.0117
a_7	3.2413	0.0272	0.3653
a_8	0.0000	0.0000	0.0000
a_9	-0.0000	-0.0000	-0.0000
a_{11}	0.0000	0.0000	0.0000
a_{12}	-0.0000	0.0000	-0.0001
a_{17}	0.1213	0.0594	-3.2834

3.2 LTV four-wheel model results

A heavily loaded LTV was modelled with the following vehicle parameters: $a_f = 1.8059m$, $a_r = 1.4961m$, $I_z = 6237kg \cdot m^2$, $m = 3182kg$, and $t_f = t_r = 1.7907m$. Front steer was set to a constant, $\delta_f = 0.015rad$. The tire model was run with 35 psi pressure up front, and 50 psi in the rear. Tire pressures were selected according to the manufacturers recommendations based on the static wheel loading conditions. In this initial model, lateral weight transfer was neglected, so the vertical wheel loads were held constant. As such, tire forces were dependent on the individual tire parameters and slip angle alone, just as with the earlier theoretical model.

The LTV vehicle configuration was similar to the theoretical models in that the normalized rear tire forces were generally less than that of the fronts. Figures 3.18, 3.19, and 3.20 show the phase portraits for the LTV model as velocity was increased. Again a saddle node bifurcation is evident.

In this model a symbolic expression of the Jacobian matrix of the state equations was created. Solving for the eigenvalues of the Jacobian at each equilibrium point allowed for a quantitative characterization of the stability at each point. In these phase plots, the saddle points are marked by a red diamond while the stable point is marked with a red square.

As expected, the real parts of the saddle point eigenvalues were positive and negative. This meant that along certain directions each saddle point was attractive (stable) and along other directions the point was repulsive (unstable). The eigenvectors correspond to the local (linearized) stable and unstable directions. Perturbing the equilibrium point slightly in the direction of the eigenvector associated with the unstable eigenvalue, and integrating forward through time, produced the

67

trajectory along which the saddle point is repulsive. These are trajectories that are directly leaving the saddle point. Perturbing slightly in the direction of the eigenvector associated with the stable eigenvalue, and integrating backward through time produced the trajectory on which the saddle point is attractive. These correspond to trajectories that travel into the saddle point. Trajectories that go into and out of the saddle point are called homoclinic orbits. The homoclinic orbits are plotted on the phase portraits in green. The dotted lines are the orbits heading toward the saddle point and the solid lines are moving away from the point. These orbits are interesting because the plots are full phase portraits of a time invariant system. None of the trajectories cross, so the homoclinic orbits define the stable manifold (domain of attraction) of the stable focus (in the pre-bifurcation portraits).

Figures 4.9 and 4.10 are the bifurcation diagrams for the system. Again, a saddle node bifurcation was evident.

3.3   Expanded model

So far, the phase portraits have been viewed within a window of practical stability limits. Any trajectory that travels outside of the window may in a practical sense be considered unstable. However, additional insight into system stability can be gained by expanding the window and allowing for a full cycle of β. To accomplish this, all small angle assumptions had to be removed. Although the four-wheel system equations made no such assumptions, the tire model assumed small slip angles. Consequently, changes to the tire force model were required.
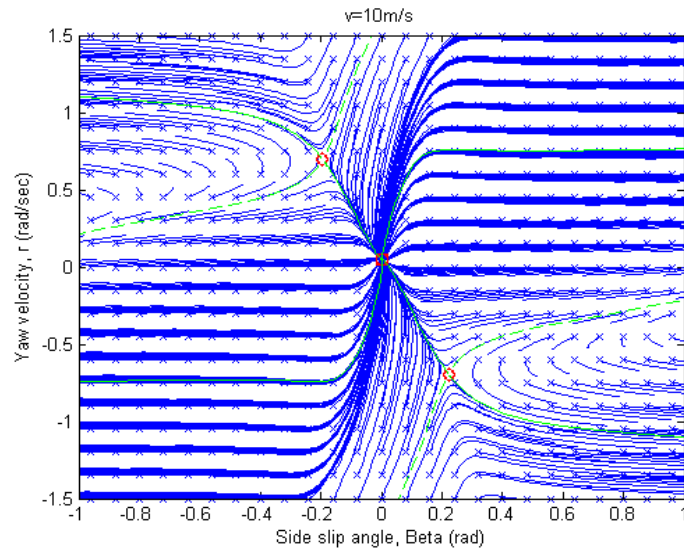
Figure 3.18: Phase portrait for LTV 4 wheel model at $V = 10 \ m/s$ and $\delta_f = 0.015$ radians.
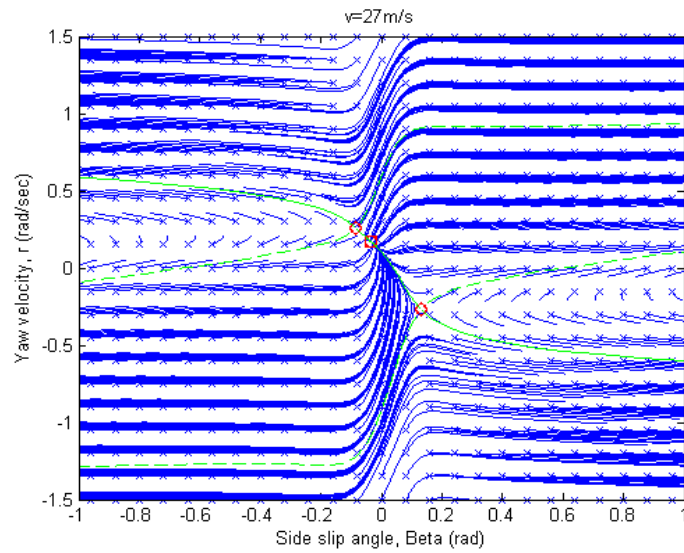
Figure 3.19: Phase portrait for LTV 4 wheel model at $V = 27 \ m/s$ and $\delta_f = 0.015$ radians.
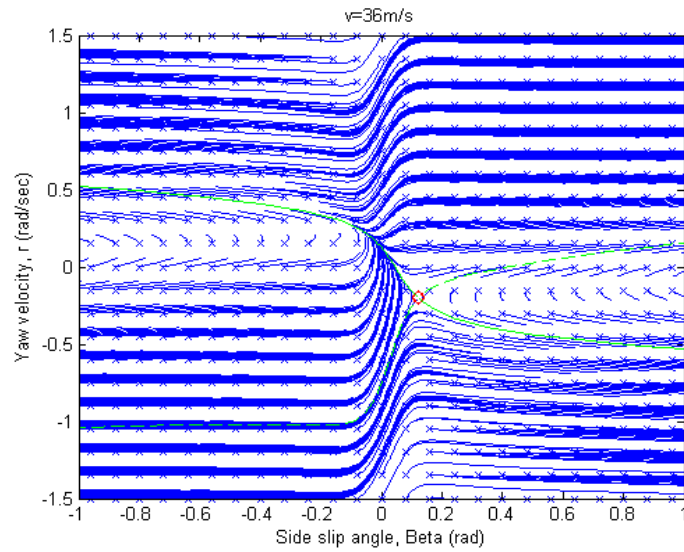
Figure 3.20: Phase portrait for LTV 4 wheel model at $V = 36 \ m/s$ and $\delta_f = 0.015$ radians.
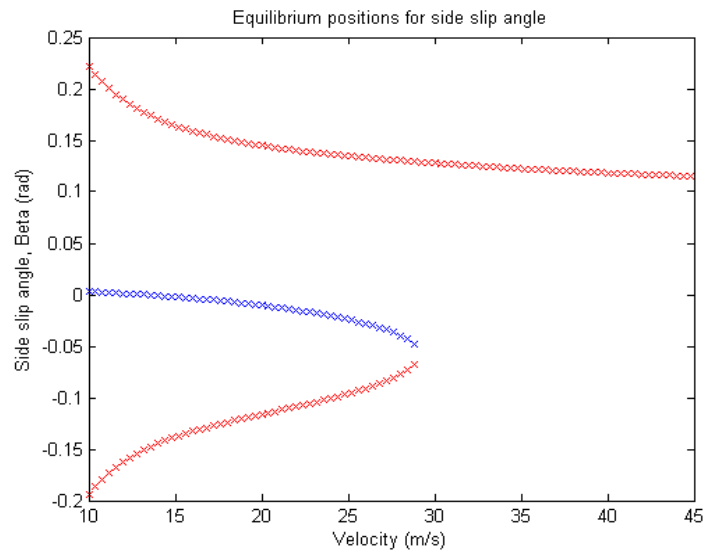
Figure 3.21: Bifurcation diagram for LTV 4 wheel model, equilibrium values of β versus speed.
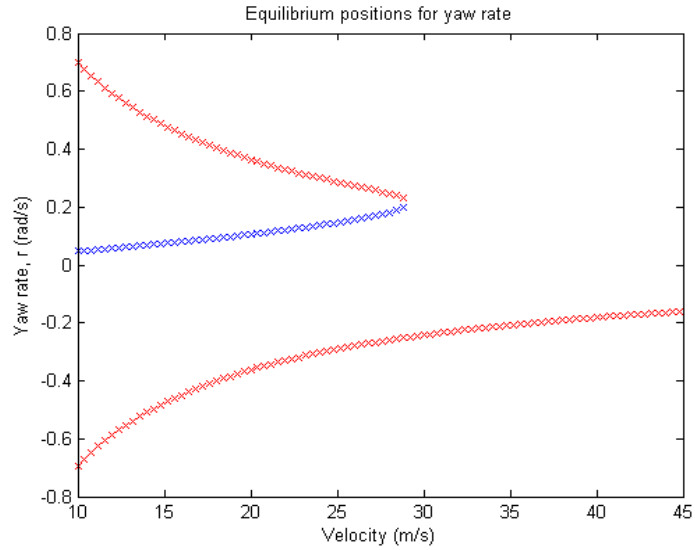
Figure 3.22: Bifurcation diagram for LTV 4 wheel model, equilibrium values of r versus speed.

3.3.1 High-slip tire force model

The tire force direction in the previous models was defined normal to velocity (Figure 3.23). This is consistent with how the empirical tire data is usually collected. However, this assumption breaks down at slip angles approaching 90°. If the tire is oriented perpendicular to the velocity (Figure 3.24), the expected force in the normal direction to velocity should be zero. Yet, with the magic tire formulation, at $\alpha = 90°$ the tire is in the saturation region and is still producing lateral force. Instead, if tire force were defined perpendicular to the tire heading (Figure 3.25), the saturated force model would still be accurate. This approach is consistent with the assumption that the tire is not producing force in the rolling direction. The tire data was not measured in this manner, but since the slip angle values for the data did not exceed 6.05° of slip, differences in the two force conventions was less

than 0.6%. The new force definition was used with the old tire data and the GA curve fits.

Another issue arises as slip angles approach 180°. As the tire starts to turn back inline with the velocity, the tire should begin to re-grip. Assuming lateral force geometry in both the forward and backward rolling directions, the tire lateral force curve can be wrapped and mirrored across 90°. A similar treatment can be applied at −90°. Figure 3.26 shows the output of the tire lateral force function versus slip angle after the wrapping is taken into consideration. The wrapping and mirroring was achieved by some manipulation using the *mod* function in Matlab. The *mod* function also allowed the lateral force function to accommodate inputs outside the [−180°, 180°] range. Tire slip angles should not exceed the [−180°, 180°] range due to the output limits of the *atan2* function. However, slip angle may go slightly outside the range due to the subtraction of the steer angle for the front tires.
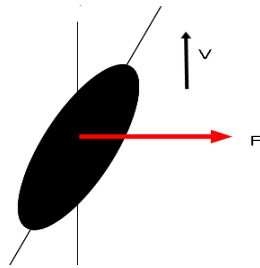
Figure 3.23: Tire force for "small" tire slip angle with force resolved perpendicular to velocity direction.
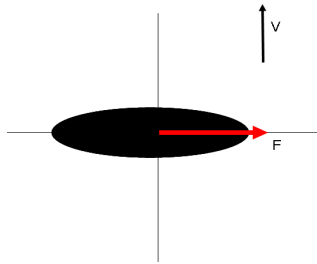
Figure 3.24: Tire force direction for 90° tire slip angle with force resolved perpendicular to velocity direction.
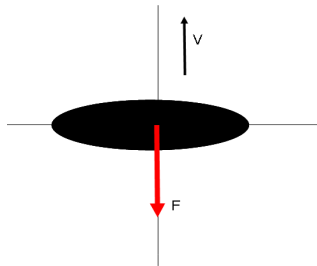
Figure 3.25: Tire force direction for 90° tire slip angle with force resolved perpendicular to tire heading.
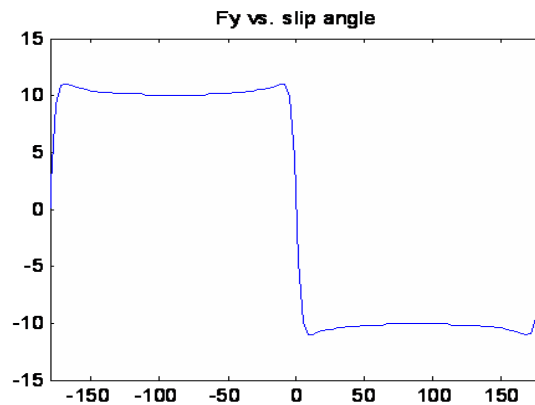
Figure 3.26: Wrapped tire lateral force function.

3.3.2   Expanded model homoclinic orbit generation

The symbolic solution to the Jacobian matrix in the expanded phase portraits was handled differently than in the four-wheel case. In the expanded model, the $atan2$ function was used for resolving slip angles, since angles outside the range of $\pm 90°$ were expected. The $atan2$ function determined the actual quadrant location of the angle in question. However, $atan2$ was not capable of dealing with symbolic entries. The mod function was also not capable of being symbolically manipulated. Consequently, the mod function was replaced (for a bounded range) by a series of conditionals. These provided a bounded range of wrapping for the lateral force function. However, even with a bounded range, model results were valid since the tire slip angles did exceed the $\pm 180°$ range by more than the maximum front steer angle. The $atan2$ function was replaced by the $atan$ function and some conditionals. Conditionals cannot be symbolically manipulated, but instead real-valued parameters were solved at each equilibrium point in order to determine the results of the conditionals. These were used to specify the proper symbolic expressions for the Jacobian matrixes. Again, eigenvalues were used to quantitatively determine the stability of the equilibrium points and eigenvectors were used to create the homoclinic orbits for the saddle points.

3.3.3   Expanded model results

State variable equations also changed due to the new direction definition of the tire forces Eq. (3.12). Using the new tire force model and the new state equations Eqs. (3.12), Figures 3.27, 3.28, and 3.29 show expanded phase portraits. In the 10 m/s phase portrait (Figure 3.27), the rear or backward facing direction ($\beta \approx \pm\pi$) also includes a stable focus and two saddle points. In addition, there exists two

unstable foci marked in the diagram by a red star. As velocity is increased to 27 m/s (pre-bifurcation in the forward facing direction), the saddle points and stable foci in the rear facing direction disappeared. This demonstrated bifurcations occurring in the rear facing directions at a point prior to the one occurring in the forward direction (with respect to velocity). As velocity was increased to 36 m/s (post-bifurcation in the forward direction) the stable focus still existed in the rear.

$$\begin{pmatrix} \dot{\beta} \\ \dot{r} \end{pmatrix} = \begin{pmatrix} \frac{F_{fr} \cdot cos(\beta - \delta_f) + F_{fl} \cdot cos(\beta - \delta_f) + F_{rr} \cdot cos(\beta) + F_{rl} \cdot cos(\beta)}{mv} - r \\ \frac{(F_{fr} + F_{fl})cos(\delta_f)a_f + (F_{fr} - F_{fl})sin(\delta_f)\frac{t_f}{2} - (F_{rr} + F_{rl})a_r}{I_z} \end{pmatrix} \qquad (3.12)$$
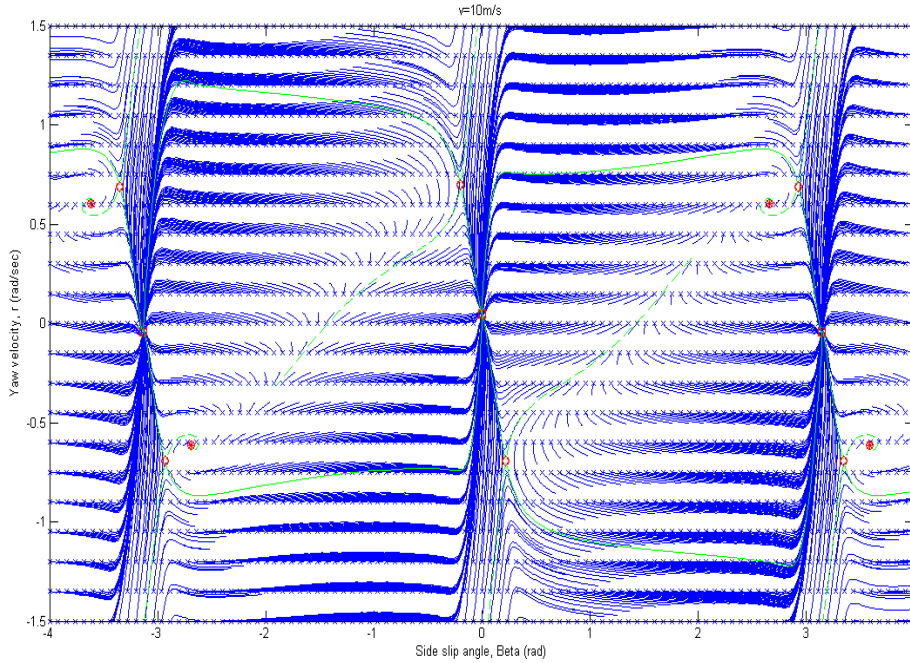
Figure 3.27: Expanded phase portrait for LTV 4 wheel model at $V = 10\ m/s$ and $\delta_f = 0.015$ radians.
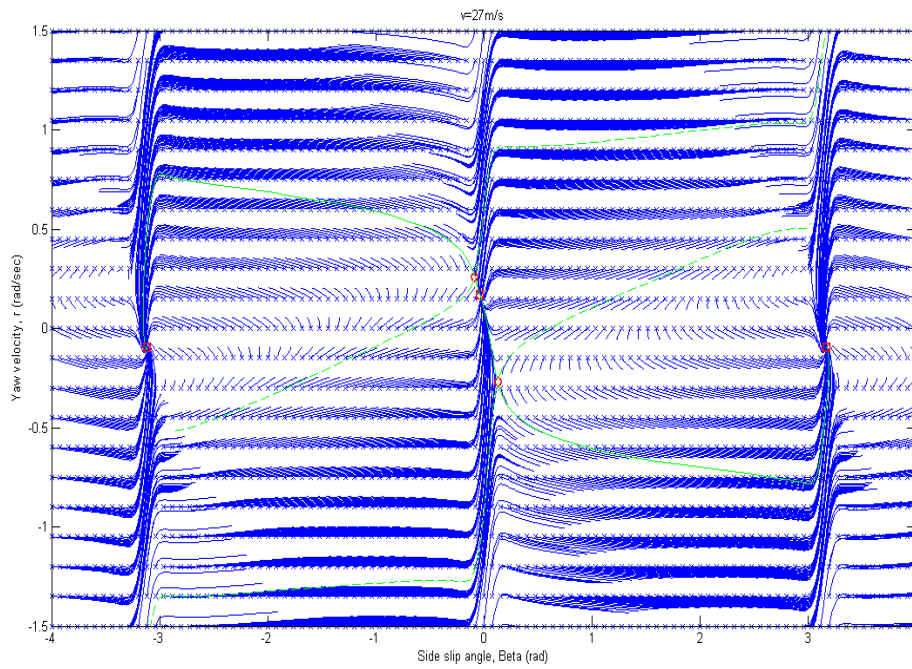
Figure 3.28: Expanded phase portrait for LTV 4 wheel model at $V = 27\ m/s$ and $\delta_f = 0.015$ radians.
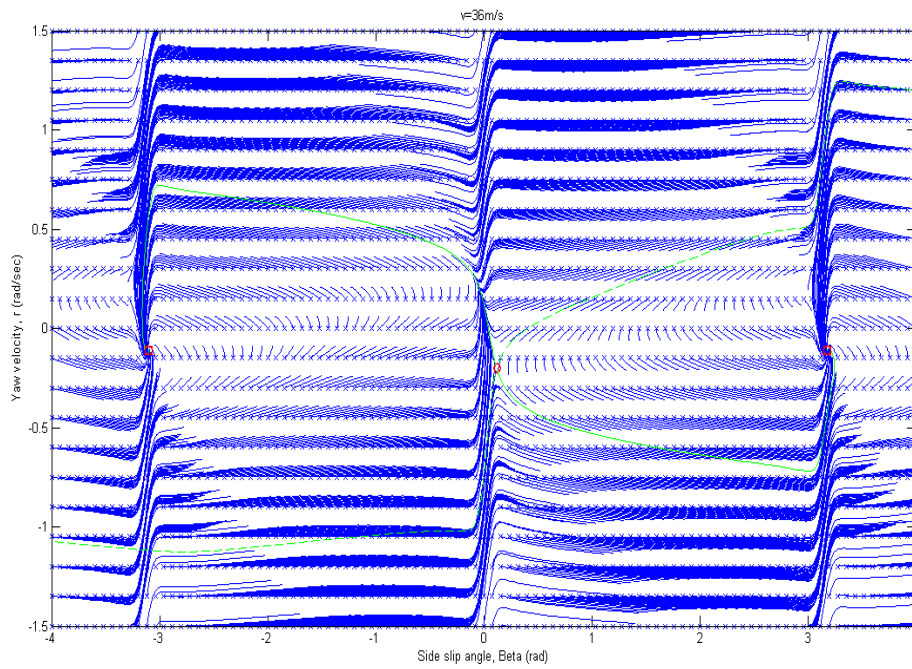
Figure 3.29: Expanded phase portrait for LTV 4 wheel model at $V = 36\ m/s$ and $\delta_f = 0.015$ radians.

3.4 Lateral load transfer model

So far, lateral weight transfer and roll dynamics have not been considered. A final model was developed to include their effects. In doing so, additional states were introduced in the system.

3.4.1 Additional states

The lateral force model included six additional states. Two were for roll angle and roll rate, and four were for each of the tire forces. In order to describe the propagation of these new states, a detailed look at the vehicle roll dynamics was required.
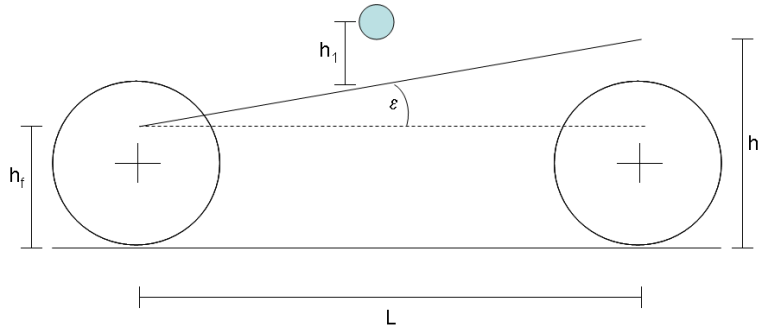
Figure 3.30: Vehicle roll axis.

The variable ϵ is defined as the inclination angle of the roll axis, illustrated in Figure 3.30, and can be described using Eq. (3.13). The terms h_f and h_r are the roll center heights at the front and rear axles, respectively. The roll axis is assumed to lie in the vehicle x-z plane. The term h_1 is the height of the CG above the roll axis.

$$\epsilon = \tan^{-1}(h_f - h_r)/L \tag{3.13}$$

Figure 3.31 shows the free body diagram for the unsprung mass at either axle. The system is in static equilibrium. Inertial forces from the body are treated as reactive forces through the theoretical pinned joint at the roll axis. F_y and F_z are the tire lateral and normal forces. The term ϕ is the roll angle of the body and the moments are the reaction moments due to the roll stiffness and roll damping of the vehicle.
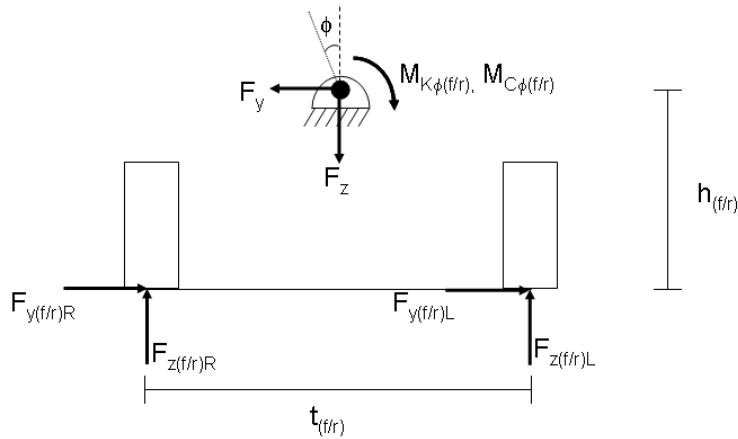
Figure 3.31: Unsprung mass free body diagram.

Figure 3.32 is the free body diagram of the sprung mass viewed as a longitudinal section at the center of gravity. Forces from the unsprung mass system are acted through the pinned joint at the roll axis, and reacted by inertial forces at the center of gravity. The term m is the vehicle sprung mass. Eq. (3.14) was obtained by balancing the forces in both free body diagrams. Roll stiffness (k_ϕ) and roll damping (c_ϕ) for the sprung mass equate to the sum of the front and rear roll stiffnesses and roll damping rates, Eq. (3.15). The reaction moments are shown in Eq. (3.16).

$$F_z = mg$$

$$F_y = ma_y = F_{yfl} + F_{yfr} + F_{yrl} + F_{yrr} \tag{3.14}$$

$$k_\phi = k_{\phi f} + k\phi r$$

$$c_\phi = c_{\phi f} + c\phi r \tag{3.15}$$

$$M_{k_\phi} = k_\phi \phi$$

$$M_{c_\phi} = c_\phi \dot{\phi} \tag{3.16}$$
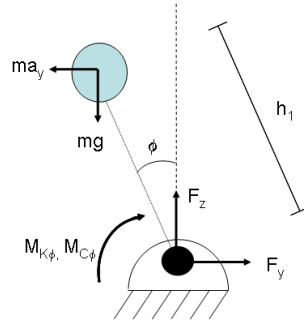
Figure 3.32: Sprung mass free body diagram.

Resolving moments about the roll axis location at the CG (Figure 3.32) yields Eq. (3.17), where I_ϕ is the full body roll moment of inertial. Equation (3.17) describes the propagation of the roll angle through time given the lateral tire forces. For the unsprung mass, it was assumed that rotational velocity and acceleration effects were negligible (low roll inertia of unsprung mass and wheels remain planted on the ground). Therefore, moments due to tire forces balanced the moment created by the roll stiffness and damping terms, Eqs. (3.18) and (3.19). With these equations, vertical load on each tire can be calculated when tire lateral forces, roll

angle and roll rate are known.

$$I_\phi \ddot{\phi} = -k_\phi \phi - c_\phi \dot{\phi} + [mg \cdot h_1 \cdot \sin \phi + F_y h_1 \cos \phi] \cdot \cos \epsilon \qquad (3.17)$$

The previous models assumed the tires would instantaneously produce their steady-state tire force output. In this case, lateral force is required to determine vertical load, which is in turn required in the tire model to determine lateral force. Therefore, a tire force propagation model was used. Eq. (3.20) depicts the tire lag model, which propagated the tire side force at each time step. The tire lag model was used to calculate transient tire forces from steady-state tire force values. $\tilde{F}_y$ is the steady-state tire force value and was determined using the magic tire formula, with the vertical load and slip angle as inputs. The term σ is the lag coefficient of the tire.

In terms of the numerical integration, at each time increment tire vertical load was determined using the roll angle, roll rate and the tire lateral force states Eqs. (3.18) and (3.19). Individual tire slip angles were calculated from β and r in the same manner as the four-wheel model. The vertical load combined with the individual tire slip angles was used to calculate $\tilde{F}_y$ from the magic tire formula. $\tilde{F}_y$ then determined the propagation of the lateral tire forces, Eq. (3.20). Roll angle and roll rate states were propagated using tire lateral force Eq. (3.17). The states β and r were propagated using the same method as the non-lateral load model, except that tire forces were no longer directly calculated. They are provided by the tire force states.

$$0 = -k_{\phi f} \phi - c_{\phi f} \dot{\phi} + [\frac{t_f}{2}(F_{zfl} - F_{zfr}) - h_f(F_{yfr} + F_{yfr})] \cos \epsilon \qquad (3.18)$$

$$0 = -k_{\phi r} \phi - c_{\phi r} \dot{\phi} + [\frac{t_r}{2}(F_{zrl} - F_{zrr}) - h_r(F_{yrr} + F_{yrr})] \cos \epsilon \qquad (3.19)$$

$$\dot{F}_y = \frac{v}{\sigma}(F_y - \tilde{F}_y) \tag{3.20}$$

3.5   Lateral load model results

For the phase portraits, roll angle, roll rate and all of the tire lateral forces were initially set to zero. This corresponded to a situation where the vehicle was initially translating and yawing at a rate corresponding to the initial values for β and r, but the tires are not making contact with the road. At time $t = 0$, the tires make contact and tire lateral force and body roll dynamics begin. This led to very busy phase portraits since each trajectory had to initially build up tire forces and roll angle.

To remove some of the "transient" dynamics in the additional states, better initial conditions were generated. Since each starting point was only defined in the β and r plane, the "steady state" values at each starting point were approximated for the additional states. Initial tire lateral forces were approximated by the steady-state value of the tire forces at the static loading condition and the initial slip angles given by the initial values for β and r. Roll angle was approximated by the initial tire lateral force values, and roll rate was set to zero. This simplified some of the "transient" responses as the simulation first began.

Figures 3.33, 3.34, and 3.35 are the phase portraits for the lateral load transfer model, using the same vehicle parameters and tire pressures as before. Because the β-r plane is only a projection in the full 8-degree-of-freedom (DOF) state space, the trajectories cross.

Equilibrium points were then calculated by setting the rate of change to zero for all the states (including the six new states). This corresponded to a situation where the body no longer rolled and the tires reached steady-state force (in addition

to the equilibrium conditions for β and r). Homoclinic orbits were not created in this case. The orbits would only represent a projection onto the β-r plane. The determination of the domain of attraction for the stable points can only be represented in the full state space. This can also be understood by observing the crossing of the trajectories. Since trajectories cross in the projected plane, the projected homoclinic orbits do no define regions of attraction.
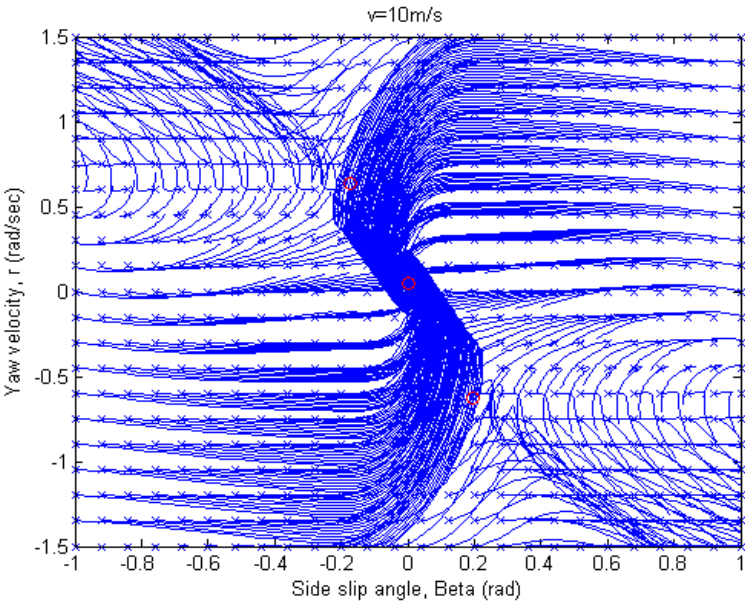
Figure 3.33: Phase portrait for lateral load transfer model at $V = 10\ m/s$ and $\delta_f = 0.015$ radians.
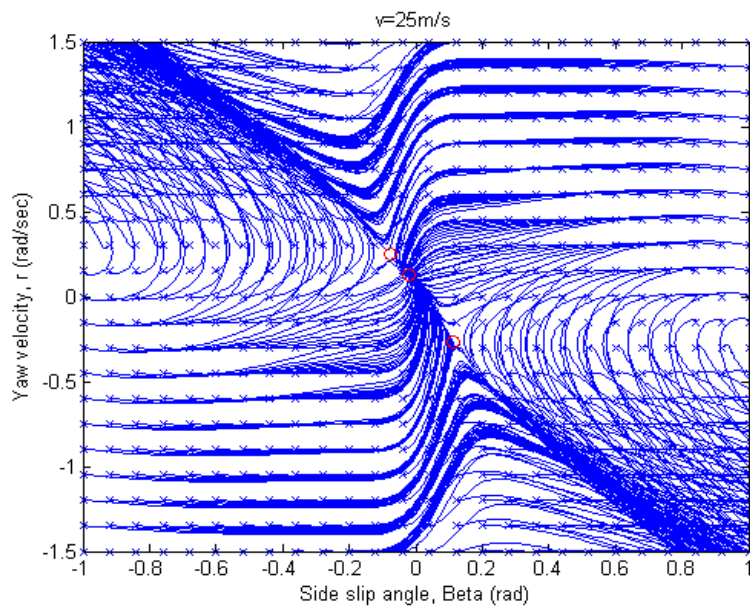
Figure 3.34: Phase portrait for lateral load transfer model at $V = 25$ m/s and $\delta_f = 0.015$ radians.
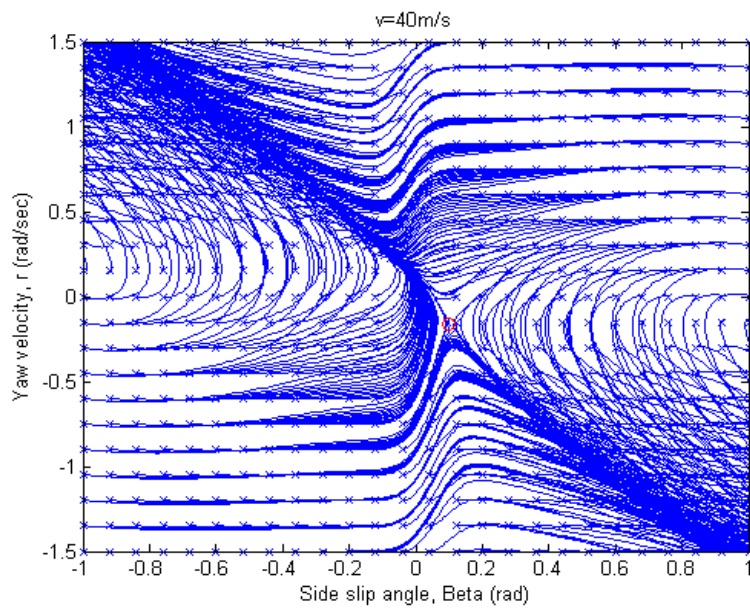
Figure 3.35: Phase portrait for lateral load transfer model at $V = 40 \ m/s$ and $\delta_f = 0.015$ radians.

Chapter 4

Analysis and observations

This chapter discusses the links between the analytical model and physical vehicle maneuvering. Interpretations of phase portraits are presented including physical meanings of equilibrium (steady-state) solutions. Bifurcation diagrams are examined and compared to vehicle handling tests. Analytic and physical stability differences are presented and some model limitations are discussed for the expanded model. US/OS/NS are discussed with respect to the nonlinear tire models, and bifurcation examples are presented for understeering and neutral steering vehicles. Finally, the lateral load model and its results are examined.

4.1   Phase portraits

Phase portraits provide a unique way to identify system behavior over a broad set of vehicle operating conditions. Their most basic interpretation relates to steady-state or quasi-steady-state behavior, though they can provide some insight into transient behavior as well. First, application to steady-state and quasi-steady-state conditions will be discussed by relating the portraits to the so-called slow input steer test.

Field tests often begin at some constant velocity and zero steer angle, meaning zero sideslip and zero yaw rate. This corresponds to the stable equilibrium condition for zero steer angle in the phase portraits. Steer angle is slowly increased (slow enough to make keep roll and yaw rate very small) until some limit in performance is reached. If steer angle were increased in small discrete steps (as is done in constant radius tests with velocity), the resulting dynamics would resemble the phase portraits at each step. Note that the steady-state field test only captures the equilibrium state at each condition. The phase portraits offer much more information.

The initial vehicle state after a step is made falls within the domain of attraction of the stable solution under the new vehicle conditions. The vehicle moves to the new stable solution, as shown by the vectors in the phase portraits. A new stable equilibrium point is created for each new step in steer angle. The different stable equilibrium points are shown in the associated phase portraits.

Thus far, only small perturbations from the stable equilibrium condition have been discussed. However, the rest of the phase portrait also contains valuable information. In contrast to the field tests, each phase portrait shows the propagation from any state other than the equilibrium solution towards the equilibrium solution. Any of the points on a given portrait can be reached by transient dynamics, whether induced by the driver or by an external disturbance, such as a sudden change in tire grip. Thus, the phase portrait shows how any disturbed state might propagate towards equilibrium given constant vehicle inputs of steer angle and velocity. It also shows how the perturbed state could progress towards instability. Domains of attraction, defined by the homoclinic orbit of the saddle points define the range of the state space that transient dynamics can return to equilibrium by

a constant vehicle parameter maneuver (holding steer and velocity constant). In Chapter 5, the idea of using the phase portraits for controlled response tests will be introduced.

4.2   Equilibrium points

Physically, for steady state handling analysis, the points of most significance in any of the phase portraits are the stable equilibrium points. Unstable equilibrium points are sensitive to slight disturbances, and any slight offset from the equilibrium point will lead to propagation away from the equilibrium solution. In practical applications, these operating points cannot be maintained without some external control of vehicle parameters (such as steer angle), which was not addressed in this research.

In all of the models presented thus far, the phase portraits began with three equilibrium positions in the forward direction, one stable and two unstable. These simulations were for oversteering vehicles. The stable point was discussed above. Aside from stability, the most notable difference between the equilibrium points were the directions and the rate at which the vehicle was turning, which can both be determined by yaw rate.

In all of the phase portraits (even post-bifurcation) in the forward direction, one equilibrium point existed in the negative yaw direction. This is unusual for a vehicle steering to the right. The negative yaw equilibrium point is unstable and relates to a "drifting" vehicle. This is a condition where the vehicle develops enough sideslip in the turn that steering the wheels in the opposite direction of the yaw rate will orient the wheels in the direction of velocity. Drifting has become a popular motorsport activity in recent years. Though drifting is commonly thought

of as an extreme case of oversteer, the phase plots show it more accurately as an unstable equilibrium condition with the vehicle turning in the opposite direction of the steer angle.

To better demonstrate the physical orientations of a vehicle as it moves through trajectories in the phase plane, a physical vehicle trajectory plot was applied. The plotter accounted for sideslip, yaw rate, and velocity versus time and displayed the vehicle path, and the vehicle orientations. The vehicle positions along the trajectory are shown by small rectangles. For clarity, the front of the vehicle is distinguished by the red line, while the rest of the vehicle is outlined in blue. The path is shown in black.

Figure 4.1 shows the orientation plot of a vehicle that is at the drift equilibrium point for a LTV model. A larger front steer angle was run for this plot in order to exaggerate the drifting motion of the vehicle. The vehicle wheelbase dimensions were augmented to better show the orientations. The vehicle is turning to the left, though the wheels are steered to the right. This behavior is due to high vehicle sideslip.

Pre-bifurcation (in the forward direction), two equilibrium points exist in the positive yaw direction. One is the stable equilibrium point and pertains to the steady-state handling dynamics, and the other is a non-stable saddle point. Physically, this point pertains to a vehicle that is overly turned (vehicle sideslip facing into the steer direction). This equilibrium point represents higher slip angles than in the stable equilibrium condition, and when not saturated, creates higher forces and tighter turns.

Figure 4.2 shows the orientation plots for the equilibrium positions from the LTV simulation done in chapter 3 at $V = 10 \ m/s$. Recall that this simulation was
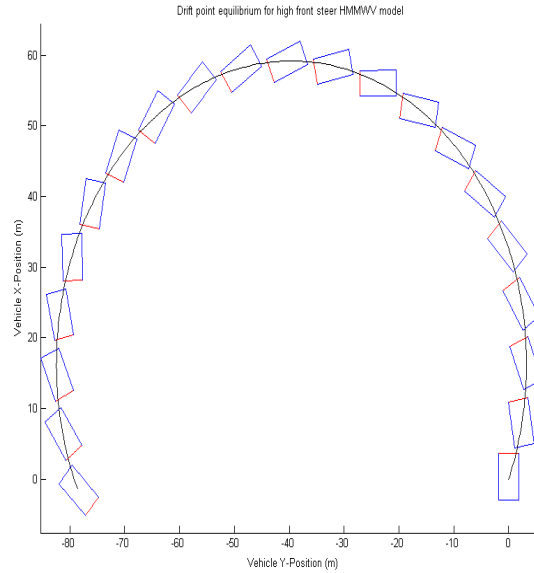
Figure 4.1: Vehicle orientation plot for a drift equilibrium point.

for a LTV in a oversteering condition. The overly turned equilibrium path creates a tighter turn due to the increased slip angles. Figure 4.3 shows the orientation plots for the equilibrium points at $V = 27 \ m/s$, a velocity closer to the bifurcation point. The stable equilibrium path and the overturned equilibrium path approach each other as the stable equilibrium point starts to generate increasing slip angles and forces. At the bifurcation velocity, the stable and unstable paths are the same (the equilibrium points converge) and the vehicle is at its handling limit (highest slip angles achievable under steady state for stable equilibrium).
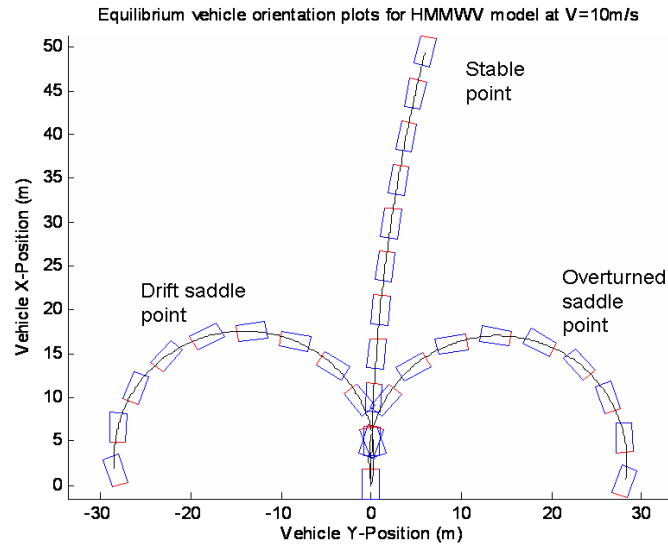
Figure 4.2: Vehicle orientation plot for equilibrium points of LTV model at 10 m/s.

Figure 4.3: Vehicle orientation plot for equilibrium points of LTV model at 27 m/s.

4.3 Bifurcation diagrams

For steady state handling tests, vehicles are expected to operate along the stable equilibrium conditions. Physical interpretations from bifurcation diagrams can be viewed with this in mind. The steer angle bifurcation diagrams such as in Figures 2.8 and 2.9 can be analogized to a slow input steer test. In this test, velocity is held constant and steer angle is slowly increased (as to allow for steady state development). At zero steer the vehicle is operating at the stable point shown on the diagra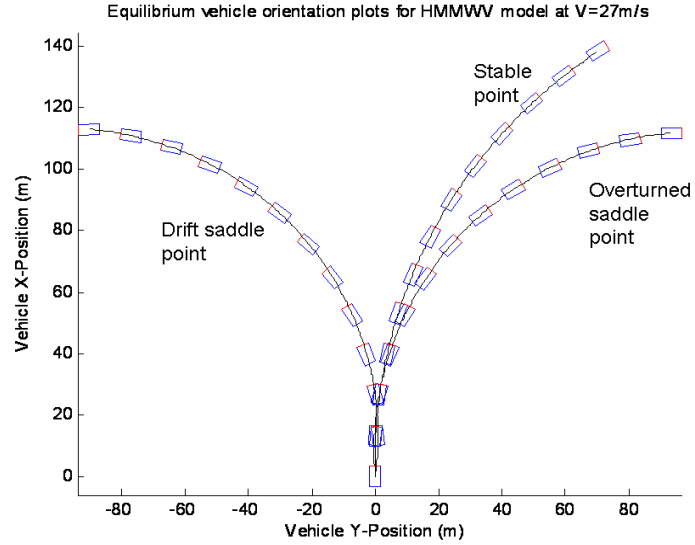ms at zero steer. As steer angle is increased the vehicle continues to operate along the stable branch of the diagrams. For an oversteering vehicle, if steer angle is increased past the bifurcation point, the vehicle can no longer maintain steady state. Characteristic differences between bifurcation plots of oversteering, understeering, and neutral steering vehicles will be described later.

Velocity bifurcation diagrams can be used to represent constant steer tests. This pertains to a test where steer angle is held constant and velocity is slowly increased (allowing for steady state). The vehicle will operate along the stable branches of the diagram until velocity passes the bifurcation point (for an oversteering vehicle). After the bifurcation point the vehicle will no longer be capable of maintaining the steady state turn. Figure 4.4 shows an enlarged view of the bifurcation diagram for sideslip for the LTV four-wheel model (Figure 4.9). Sideslip initially begins as positive (turned out of the turn) and switches to negative (turned into the turn) as velocity is increased.
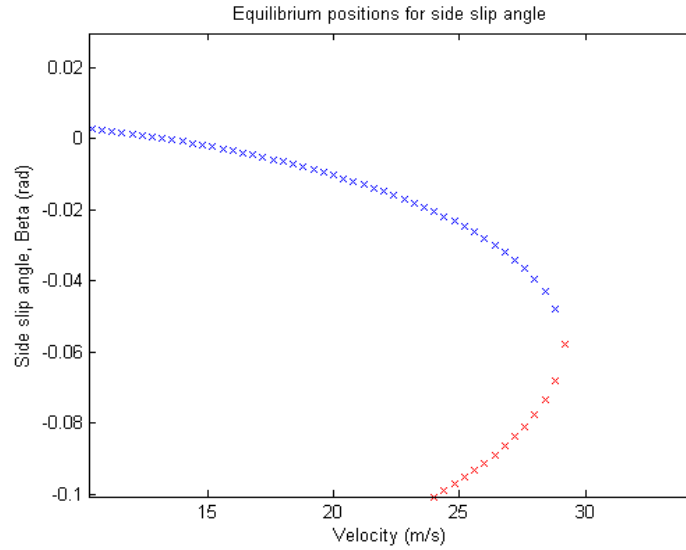
Figure 4.4: Zoomed in view of bifurcation diagram for LTV 4 wheel model, equilibrium values of β versus speed.

4.4 Understeer and neutral steer

The theoretical and LTV-based models presented thus far can be classified as oversteering (in the forward direction). The bifurcations observed intuitively agree with this classification. As steer angle or velocity was increased, the stable point disappeared and the vehicle exceeded the practical operating limits, causing spin out. Bifurcation behavior was found to be different for US and NS vehicles, as will be discussed in the following section. Supporting theory for understeer, oversteer, and neutral steer with nonlinear tire models is presented at the end of this chapter for clarity.

4.4.1 Understeer

To better understand understeering bifurcation dynamics, an understeering vehicle was created. The understeering model was based on the LTV four-wheel model. To simplify the modifications, the simulation was run with 50 *psi* front and rear tire pressure. The US/OS/NS classification is dependent on the normalized tire force curves which are dependent on the tire forces and the axle weights. With the same tires front and rear, US/NS/OS was controlled by simply adjusting the weight by changing the CG location.

The LTV model was run with the same vehicle parameters except for the longitudinal CG location. The dimensions a_f and a_r were interchanged, so $a_f = 1.4961$ and $a_r = 1.8059$. This moved the CG location closer to the front axle. Figure 4.5 shows a low-speed phase portrait for the understeering model with the same simulation parameters as in the earlier LTV model. Similar to the rear facing direction in the expanded model, there exists five equilibrium points at low-speed, one stable, two saddle and two unstable points. Figure 4.6 shows the same understeering model at higher speed. Only the stable point remains. Intuitively this agrees with the behavior of an understeering vehicle. As velocities and slip angles increase, the front tires reach their limits and are no longer able to produce sufficient force while the rear tires are still capable of creating a stabilizing moment. The vehicle can be thought of as 'plowing' out of the turn. Unlike the oversteering case, a stable equilibrium position in the forward direction was always present.
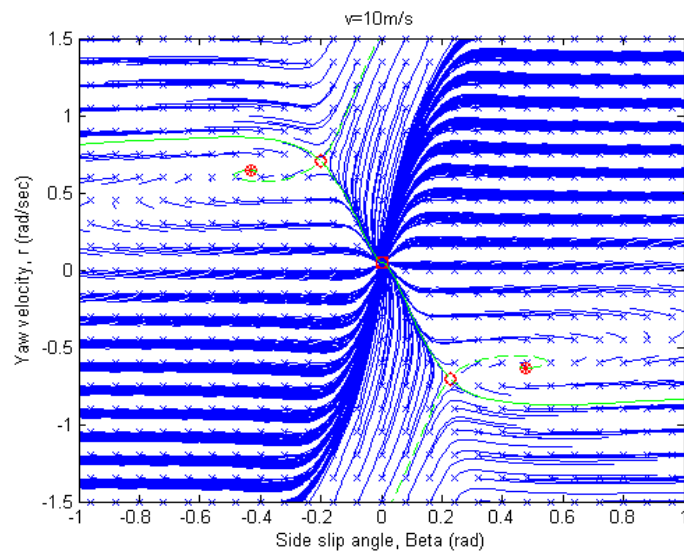
Figure 4.5: Low speed, understeering phase plot.
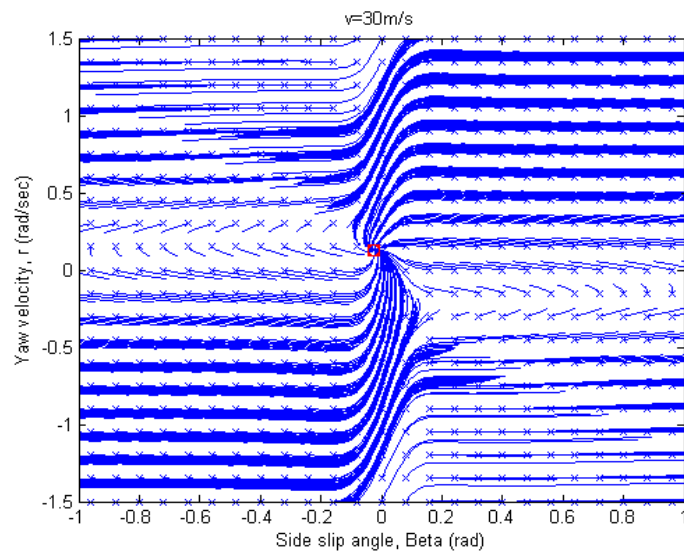
Figure 4.6: High speed, understeering phase plot.

4.4.2 Neutral steer

In a similar manner to the understeering case, a neutral steering vehicle was created from the LTV model. By setting $a_f = a_r = 1.651$ and running the 50 *psi* tire model for all four wheel corners, the front and rear normalized tire force curves were exactly the same. So, $\alpha_f = \alpha_r$ for any of the equilibrium points, and front steer angle was simply the Ackerman steer angle. Figure 4.7 shows the neutral steering phase plot at low speed. The plot is very similar to the oversteering case with the same three equilibrium points. Figure 4.8 shows the high-speed neutral steering case. Two equilibrium solutions still exist, however trajectories leading to the stable point are not apparent. This qualitatively means that the stable point is a weak attractor or a "weakly" stable point (small real part of the eigenvalues). More will be discussed about this in the following section.
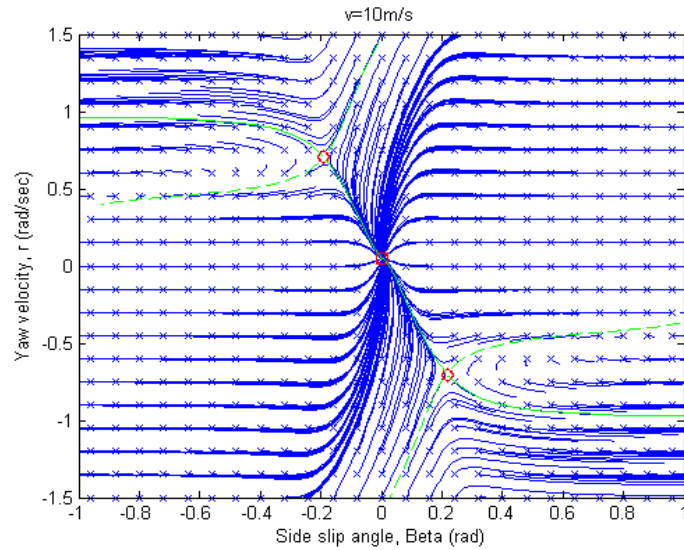
Figure 4.7: Low speed, neutral steering phase plot.
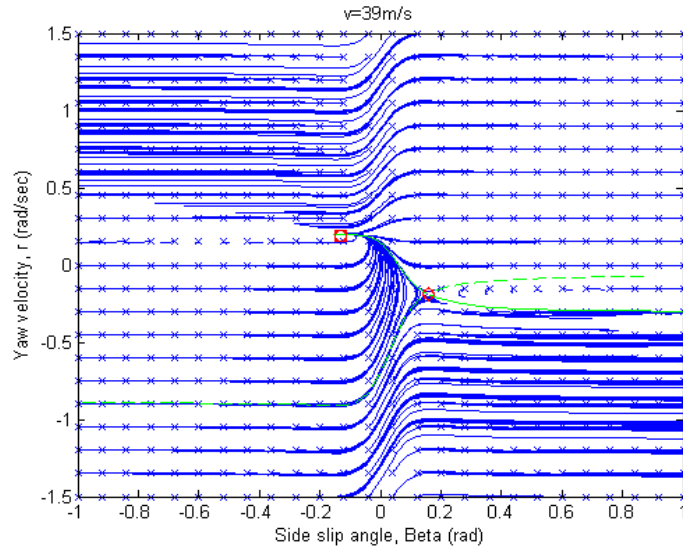
Figure 4.8: High speed, neutral steering phase plot.

4.4.3 US/OS/NS bifurcation diagrams

Figures 4.9 and 4.10 are the bifurcation diagrams presented for the four-wheel model presented in chapter 3. As mentioned earlier the vehicle parameters used in these models produce an oversteering vehicle. As velocity is increased past the bifurcation value for velocity, the stable equilibrium (the operating point for steady-state handling) disappears leaving no stable solution.

Figures 4.11 and 4.12 are the bifurcation plots for the understeering model. As velocity was increased, the saddle points and the unstable equilibrium points converge to form two separate saddle node bifurcations. Bifurcations occur at different values for velocity. However, since the bifurcations only involve the unstable/nonstable points, they are not as physically significant as the saddle node bifurcation found in the oversteering case. The most important note for the understeering model was that the stable equilibrium solution does not see a bifurcation,

so the system is inherently stable in pure understeer.

Figures 4.13 and 4.14 are the bifurcation diagrams for the neutral steering case. The stable equilibrium and one saddle node appear to converge. The branch that continues represents the weak attracting/repulsing equilibrium point seen in the phase portraits. The eigenvalues along the branch were shown to have real parts very close to zero. This refers to the "drift" condition for neutral steering vehicles when all four tires are saturated. The drop in the sideslip plot for the stable equilibrium (before converging with the saddle point) was attributed to an abrupt change in tire force characteristics. This was due to the front and rear tires saturating together, since in the neutral case the front and rear sideslips, for steady-state, are equal.

Figure 4.9: Bifurcation diagram for LTV 4 wheel model, equilibrium values of β versus speed.
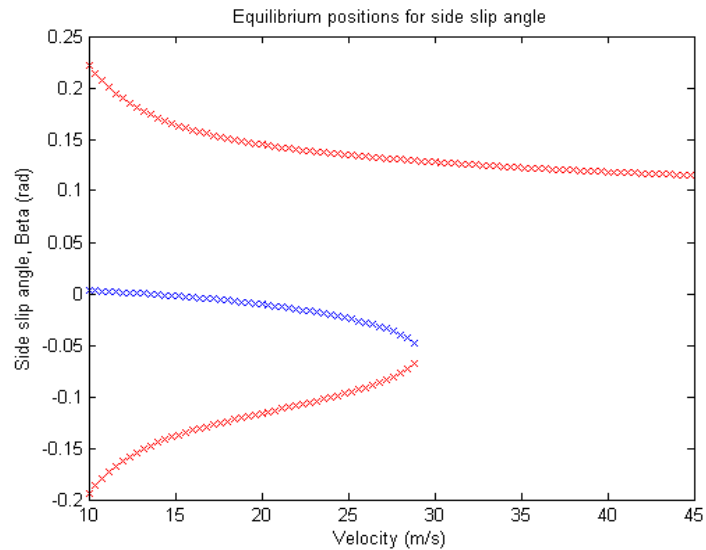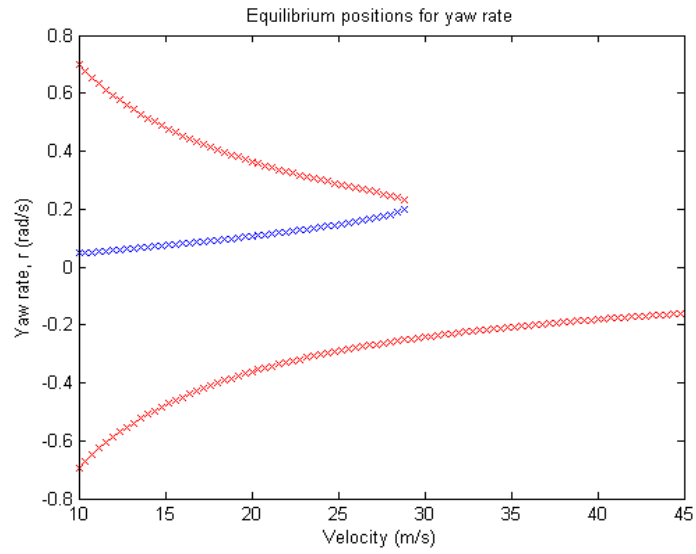
Figure 4.10: Bifurcation diagram for LTV 4 wheel model, equilibrium values of r versus speed.
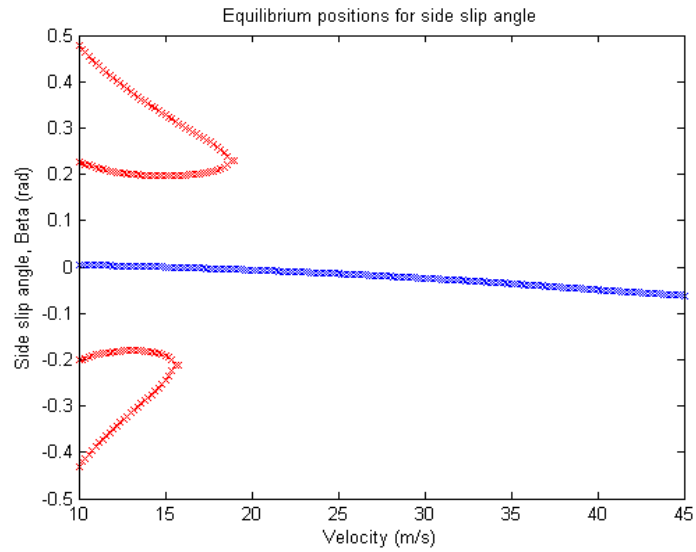

Figure 4.11: β Speed bifurcation diagram for understeering model.
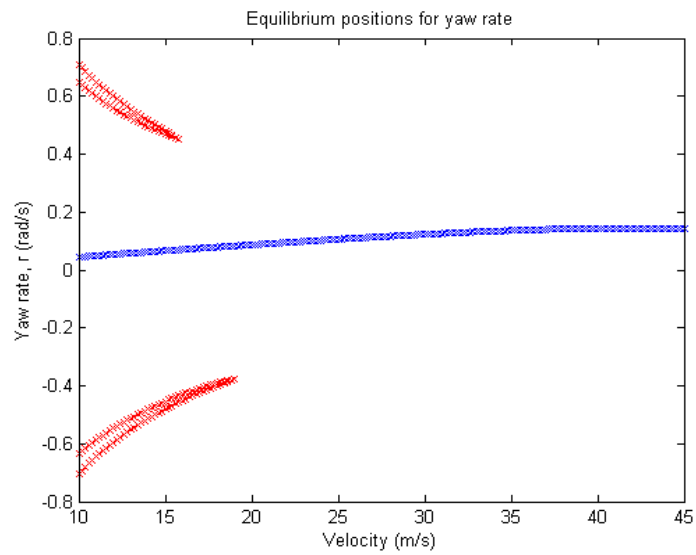
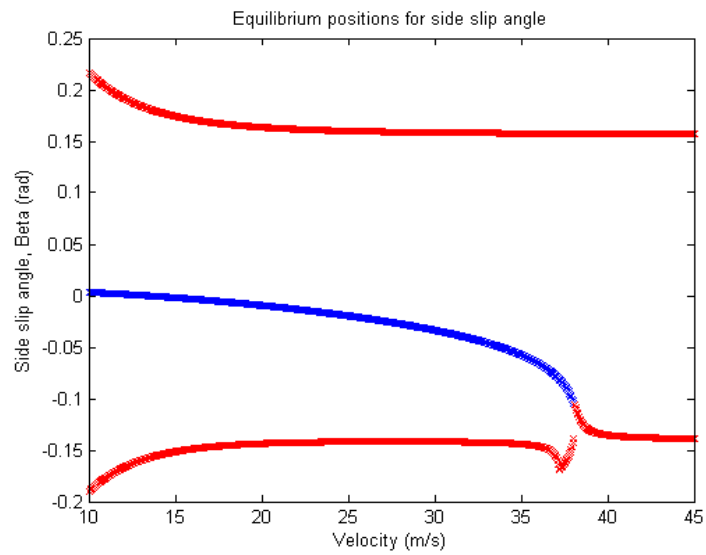Figure 4.12: r Speed bifurcation diagram for understeering model.

Figure 4.13: β Speed bifurcation diagram for neutral steering model.
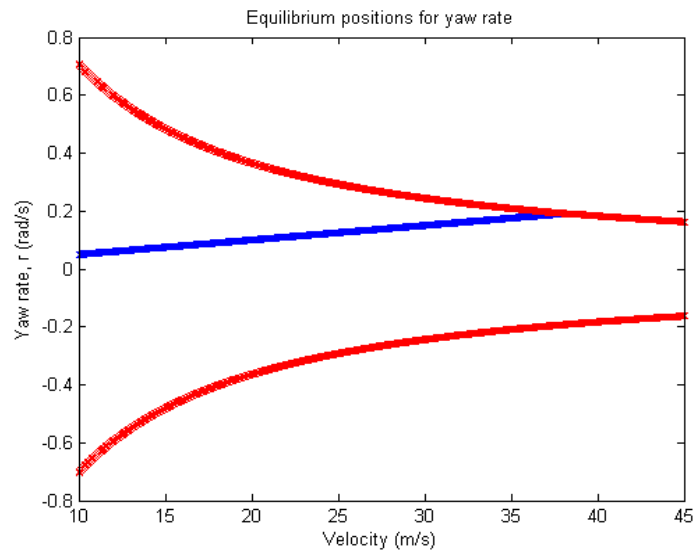
Figure 4.14: r Speed bifurcation diagram for neutral steering model.

4.5 Expanded model results

The rearward facing direction in the expanded model can be analogized to a forward facing understeering vehicle. Although the vehicle in this condition was in fact rear wheel steering, the tire and vehicle characteristics can still be used to define its steady-state behavior. The bifurcations observed in a conventional forward facing, understeering, front-steer vehicle can be seen in the rear facing direction of the expanded model. The most important similarity is that the stable equilibrium in the rear facing direction exists at all speeds. This section discusses stability notions for the expanded model and outlines some drawbacks in correlating this model to practical vehicle maneuvers.

4.5.1 General stability versus practical stability

The expanded model extended the phase portrait outside of normal operational limits to include dynamics such as backward-facing motion. The extended phase portraits allow for analysis regarding overall system stability in the analytic sense. Vehicles exceeding normal operating limitations may still be analytically stable. For instance, the trajectory highlighted in Figure 4.15 shows vehicle motion that would be considered unstable in the practical sense, but is still stable in terms of the system equations (bounded). The vehicle in this case begins outside the stable manifold for the forward facing stable equilibrium. The vehicle eventually rotates past $-90°$ of sideslip. In a system sense, the trajectory is stable since it remains bounded as it eventually ends up at a rear-facing stable equilibrium point. Figure 4.16 shows the orientation plot for the trajectory highlighted in Figure 4.15. The stable rear-facing equilibrium solution can be clearly seen as the vehicle eventually reaches steady-state.
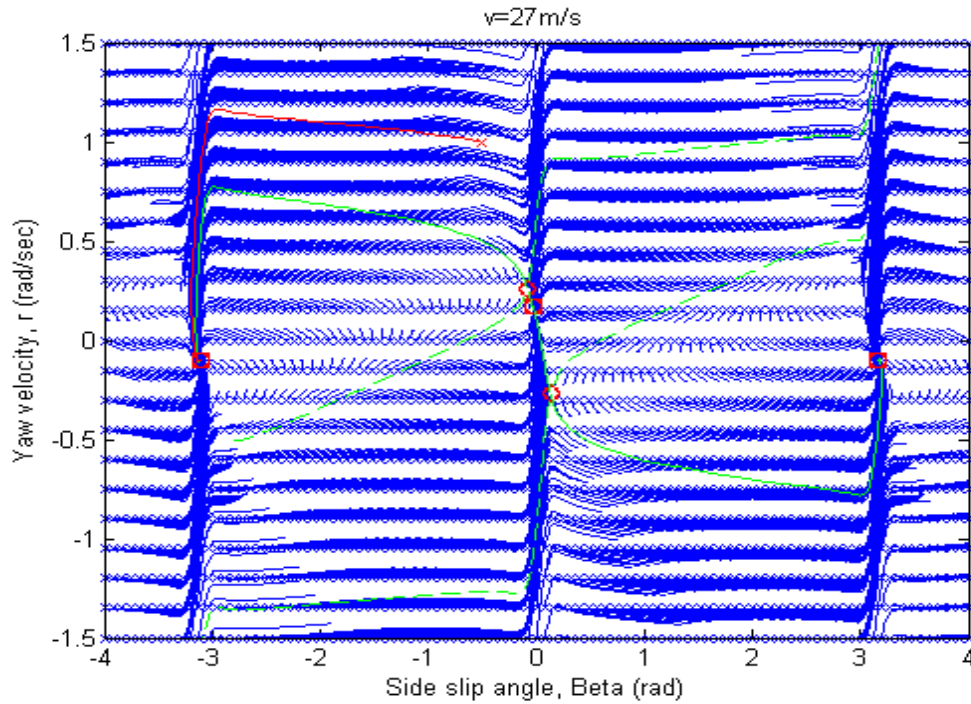
Figure 4.15: Phase portrait for extended LTV model at $V = 27\ m/s$.

Another example can be shown post-bifurcation in the forward direction. Figure 4.17 is the phase portrait for the model at $V = 36\ m/s$. In this case the highlighted trajectory is initiated under conditions where there exists no stable equilibrium in the forward direction. The trajectory then migrates to the rearward facing stable equilibrium. Figure 4.18 shows the orientation plot for the trajectory highlighted. The vehicle can be observed initially spinning and finally reaching a steady condition in the backward direction.

The phase plots are repeating along the β direction, so any bounded initial condition for β is analogous to the $[-\pi, \pi]$ window. However the phase plane is not repeated along the yaw rate direction. Figure 4.19 is an orientation plot for a vehicle that starts with a very high yaw rate. The vehicle spins a few times and
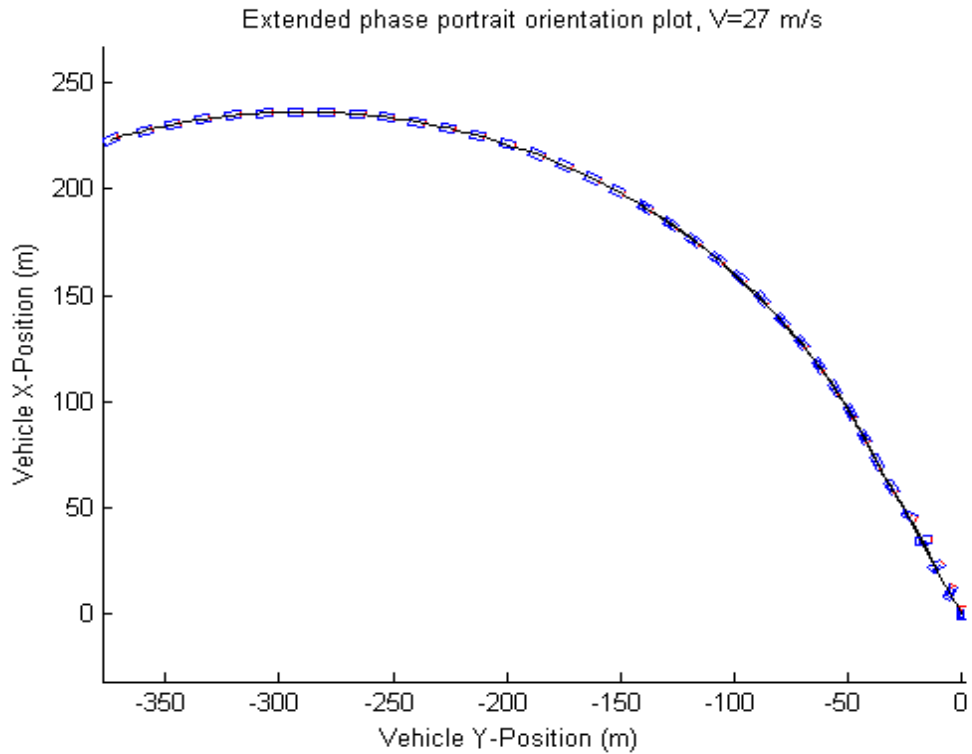
Figure 4.16: Orientation plot for trajectory highlighted in $V = 27\ m/s$ phase plot.

finally reaches steady state at one of the backward facing equilibrium points. This is an example of how bounded yaw rate initial conditions will eventually decay and end up at one of the stable equilibrium points. This can be attributed to the tires acting as yaw dampers slowing the rotational motion with time. This shows an overall qualitative system stability for bounded initial conditions.

Figure 4.17: Phase portrait for extended LTV model at $V = 36\ m/s$.

Figure 4.18: Orientation plot for trajectory highlighted in $V = 36 \ m/s$ phase plot.
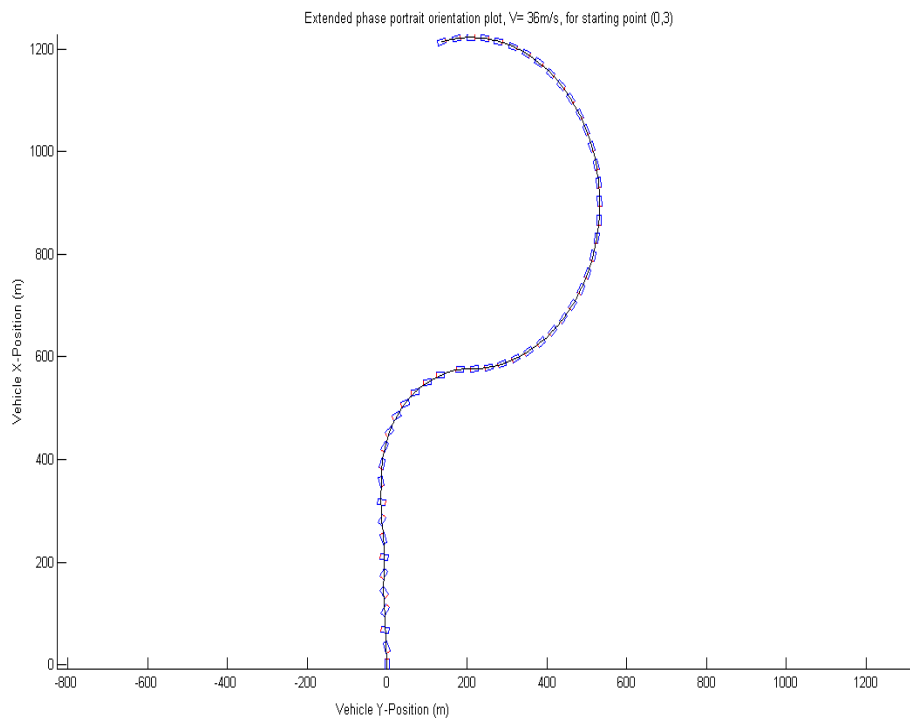
Figure 4.19: Orientation plot for a rapidly spinning vehicle.

4.5.2 Practicality of constant velocity assumptions

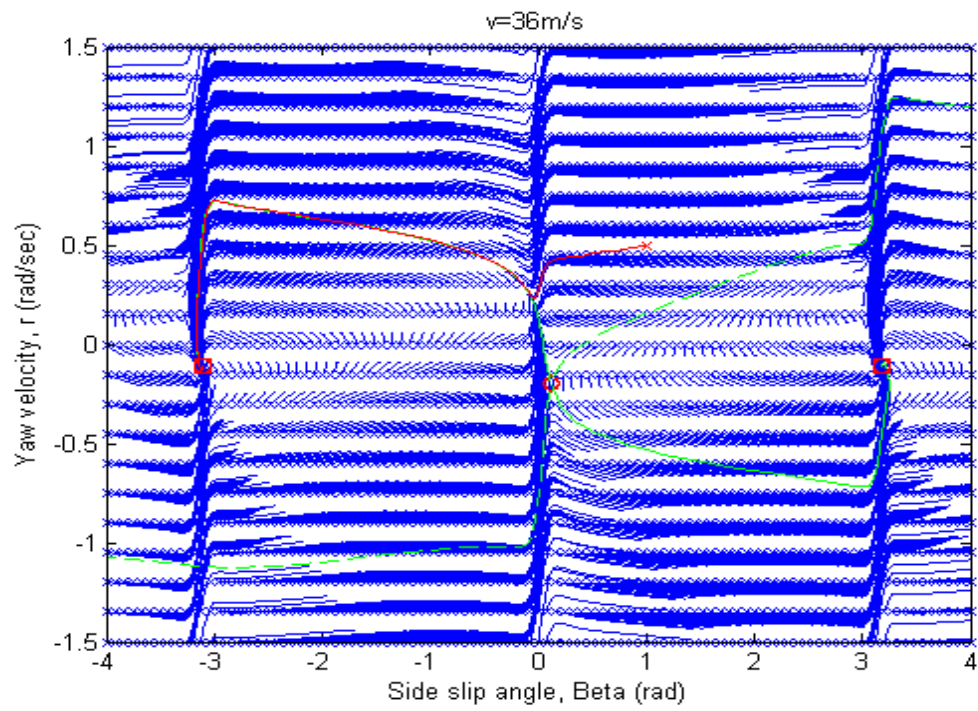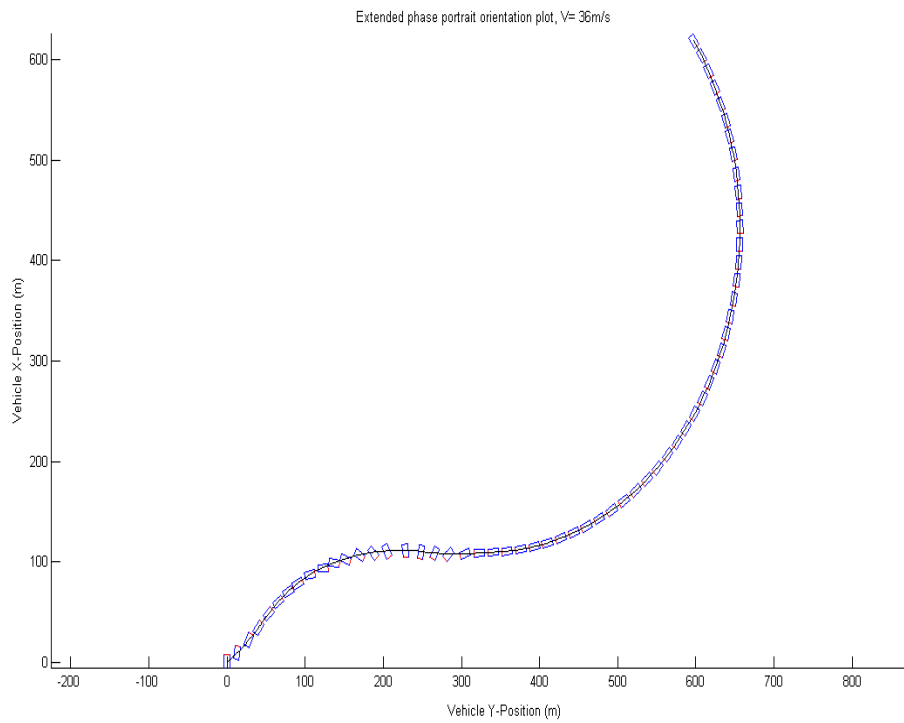Although the extended model shows the vehicle system as being overall stable (for bounded initial conditions), there are some drawbacks to viewing the vehicle with this model. Vehicle motion in the state space is bounded, but the state approach only considers motion relative to the vehicle reference frame. In practice, a fixed reference frame, such as the one used for the orientation plots (motion with respect to the road coordinates), is more practical. Also, when considering forward motion, excessive sideslips and backward motion should not be considered as a "stable" motions.

Another drawback to the method is the constant velocity magnitude condition. In all of the models, the velocity magnitude was considered constant. Tire forces in the direction of the velocity are neglected. As with yaw, tire forces (unless balanced) are expected to reduce velocity when slip angles are present. This is due to the fact that slip angles generate tire force components that oppose velocity. The deceleration in the direction of velocity is assumed to be balanced by the driving torque of the vehicle. When vehicle sideslip is small, forward drive torque can adequately oppose the tire force. As sideslip increases (and ultimately at $\pm 90°$ sideslip for a RWD vehicle) the drive torque can no longer be expected to provide any appreciable force in the direction of velocity. Also, drive torque cannot be expected to provide force solely in the direction of velocity. When the vehicle begins to face backward, the driving force must switch from forward to backward in order to counter tire resistance. In a real-world maneuver, reaching a rearward facing equilibrium from a forward facing initial condition requires switching from forward driving torque to reverse driving torque. These conditions are not practical. Instead, these trajectories can be thought of as pertaining to transient

spinouts, where the vehicle carries speed through the maneuver (tire forces don't appreciably reduce the velocity magnitude).

4.6   Lateral load model

The lateral load model is difficult to analyze using only the β-r plane. The state space plane is only a projection of the entire set of system states. β and r no longer fully define the vehicle operating state. A vehicle operating at a particular β and r can still be operating at an infinite number of roll angles, roll rates, and tire lateral forces. However, even with propagations external to the projected plane, system tendencies can still be observed in the phase portraits. Trajectories can be observed migrating towards the stable equilibrium and travelling towards and away from the saddle points. Equilibrium solutions in this model show vehicle motion (β and r) at steady state under a dynamic lateral loading condition.

Further exploration of the lateral load model is left for future work, where a time animation might help describe and visualize system dynamics for different initial conditions. In addition, a possible alternative model is presented later in Chapter 5.

4.7   Nonlinear steady-state handling classification

For the nonlinear regimes of performance, the qualitative definitions of steady-state US/OS/NS are the same as in the linear model presented in chapter 1. US/OS/NS can be physically described when requiring more or less steer angle as (as compared to the Ackerman steer angle) velocity is increased. In this analysis, steady-state classification is performed in only the positive yaw direction, although the analysis

can be applied in a similar manner to the opposite direction. Again practical US/OS/NS definitions relate to local rate of change of steer angle. If steer angle is increasing (regardless of it's relationship to the Ackerman steer angle) when velocity increases, the vehicle can be considered as understeering. If the steer angle is decreasing, the vehicle is oversteering.

As with the classification presented in chapter 1, it is easiest to work with a bicycle vehicle model. Revisiting equations (2.7) and (2.9) for the bicycle model, front steer angle can be rewritten as Eq. (4.1). From Eqs. (2.8), and (2.10), β can be written as Eq. (4.2). Eqs. (4.1) and (4.2) can then be combined to create a representation of front steer angle in terms of α_f and α_r, as given in Eq. (4.3). For a constant radius turn, $r = V/R$ describes the relationship between velocity, V, turn radius, R, and yaw rate r. Substituting this relationship into Eq. (4.3) puts all the terms in a form similar to the analysis in chapter 1, as shown in Eq. (4.4).

$$\delta_f = \beta - tan^{-1}\left(\frac{a_f r cos(\beta)}{V}\right) - \alpha_f \tag{4.1}$$

$$\beta = tan^{-1}\left(\frac{a_r r cos(\beta)}{V}\right) + \alpha_r \tag{4.2}$$

$$\delta_f = tan^{-1}\left(\frac{a_r r cos(\beta)}{V}\right) - tan^{-1}\left(\frac{a_f r cos(\beta)}{V}\right) + \alpha_r - \alpha_f \tag{4.3}$$

$$\delta_f = tan^{-1}\left(\frac{a_r cos(\beta)}{R}\right) - tan^{-1}\left(\frac{a_f cos(\beta)}{R}\right) + \alpha_r - \alpha_f \tag{4.4}$$

The first terms in the expression for front steer angle, $tan^{-1}\left(\frac{a_r cos(\beta)}{R}\right) - tan^{-1}\left(\frac{a_f cos(\beta)}{R}\right)$, can be thought of as the Ackerman steer angle. With a few small angle approximations for β and $a_{(f/r)}/R$, and the Ackerman steer angle simplifies to the familiar L/R (the same form used in the linear tire analysis). With either representation, the Ackerman steer angle is constant with respect to the vehicle and turn parameters, therefore the only term of interest is $(\alpha_r - \alpha_f)$.

The sign of this term is opposite from the analysis in Chapter 1. This can

be attributed to the tire force direction definition used (Figure 2.3) for the state equations. In contrast to the definition used in Chapter 1 (where a positive slip angle created a positive tire force) for the analytical models, a negative slip angle produced a positive tire force. So, in the state equations a positive yaw (positive net tire forces) is created by negative slip angles. If the vehicle is understeering, $(\alpha_r - \alpha_f)$ is positive (α_f is more negative than α_r), so the magnitude of the slip angle of the front tires is greater than that of the rears. If the vehicle is oversteering, $(\alpha_r - \alpha_f)$ is negative (α_r is more negative than α_f), and the magnitude of the slip angle at the rear is greater than that of the fronts. Thus, when comparing the slip magnitudes, the nonlinear analysis is the same as in Chapter 1. The only difference was the tire force/slip angle convention used in each method.

Steady-state US/OS/NS characteristics refer only to stable equilibrium points in the state space models. Solving the state equations, Eq. (2.3), for the equilibrium points, yields Eqs. (4.5) and (4.6). These equations can then be combined to create representations for F_f and F_r for steady-state conditions, given by Eqs. (4.7) and (4.8). Not surprisingly, these are the same equations found by force and moment balance in Chapter 1.

$$F_f + F_r = m \cdot v \cdot r \tag{4.5}$$

$$F_f a_f = F_r a_r \tag{4.6}$$

$$F_f = \frac{W_f}{g} V \cdot r \tag{4.7}$$

$$F_r = \frac{W_r}{g} V \cdot r \tag{4.8}$$

Since tires are nonlinear, the relationship between the tire forces required for equilibrium, and the individual slip angles is more complicated. For simplicity, the magic tire formulation used in any of the models (the general form in the

111

theoretical models or the more complex form used in the LTV model) can be simply represented as a function: $MTF(\alpha) = F$. For a given load on the tire, the MTF function describes the relationship between the tire force and the slip angle of the tire. Equilibrium tire force equations can than be rewritten, substituting expressions for α_f and α_r from an inverse magic tire function (MTF^{-1}), Eqs. (4.9) and (4.10).

Since the tire force representation for equilibrium conditions are represented in terms of the respective axle weights, the forces can be represented by a normalized magic tire function, $NMFT(\alpha) = \frac{MTF(\alpha)}{W/g}$. This function outputs the normalized tire force (tire force divided by the mass over the axle, $\frac{F}{W/g}$). Taking the inverse of this function yields $NMTF^{-1}(NTF) = MTF^{-1}(NTF \cdot W/g)$, where NTF is the normalized tire force. Substituting this into Eqs. (4.9) and (4.10) gives Eqs. (4.11) and (4.12), where $NTF = V \cdot r$ for both front and rear. Therefore, for a given value of V and r the equilibrium conditions dictate that the normalized tire forces, front and rear, must be equal.

$$\alpha_f = MTF_f^{-1}(\frac{W_f}{g}V \cdot r) \tag{4.9}$$

$$\alpha_r = MTF_r^{-1}(\frac{W_r}{g}V \cdot r) \tag{4.10}$$

$$\alpha_f = NMTF_f^{-1}(V \cdot r) \tag{4.11}$$

$$\alpha_r = NMTF_r^{-1}(V \cdot r) \tag{4.12}$$

Figure 4.20 shows the normalized tire force for the front and rear tires for the bicycle model. Figure 4.21 shows an enlarged view of the normalized tire force diagrams near limit conditions. For the equilibrium conditions to be satisfied, the normalized tire forces (lateral acceleration) must be the same for front and rear tires and equal to $V \cdot r$. Figure 4.21 shows the value for $(\alpha_f - \alpha_r)$ for the stable

equilibrium point for a given value of $V \cdot r$. In this near limit condition, $\alpha_r < \alpha_f$, so $(\alpha_r - \alpha_f)$ is negative and the vehicle is steered less than the Ackerman steer angle (exhibiting oversteer). It can also be noted that as lateral acceleration is increased ($V \cdot r$ is increased), $(\alpha_r - \alpha_f)$ becomes even more negative ($\alpha_f - \alpha_r$ on the diagram grows wider). Figure 4.22 is a plot of $(\alpha_r - \alpha_f)$ versus lateral acceleration. Near the limit (high lateral accelerations) the slope of the curve is negative, indicating that increases in lateral acceleration lead to decreases in $(\alpha_r - \alpha_f)$ which in turn means decreases the front steer angle (Eq. (4.4). The vehicle, near limit, can also be considered oversteering in the practical sense (showing increasing oversteer). One interesting note is that for the theoretical bicycle model, at the lower lateral accelerations, both $(\alpha_r - \alpha_f)$ and the slope are positive. This means that the vehicle initially understeers in the analytical and practical sense. The vehicle then transitions into oversteer near limit. The remaining theoretical models are based on the bicycle model tire forces, so similar analysis provides the same oversteering results for the tandem, and four-wheel theoretical models.

Figure 4.23 shows the normalized tire force curves for the tires and vehicle parameters used in the LTV four-wheel model. Figure 4.24 shows the $(\alpha_r - \alpha_f)$ versus lateral acceleration plot. The values for $(\alpha_r - \alpha_f)$ are negative so the vehicle is always exhibiting oversteer. Furthermore the slope of the curve is also always negative, so the vehicle shows increasing oversteer and can also be considered always oversteering in the practical sense.
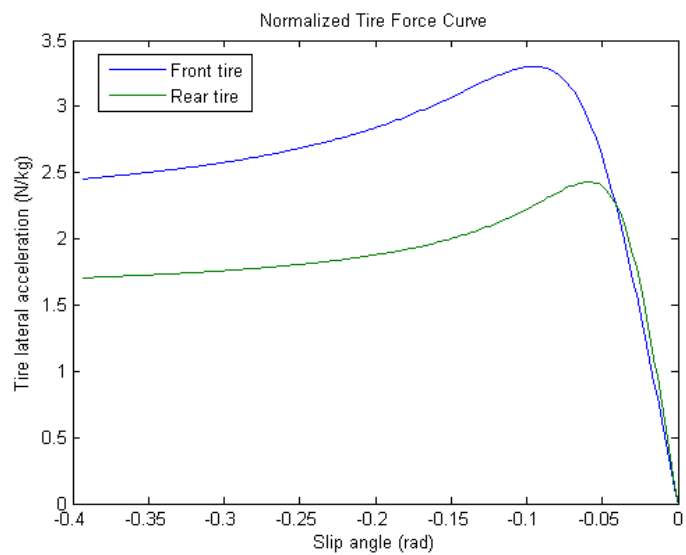
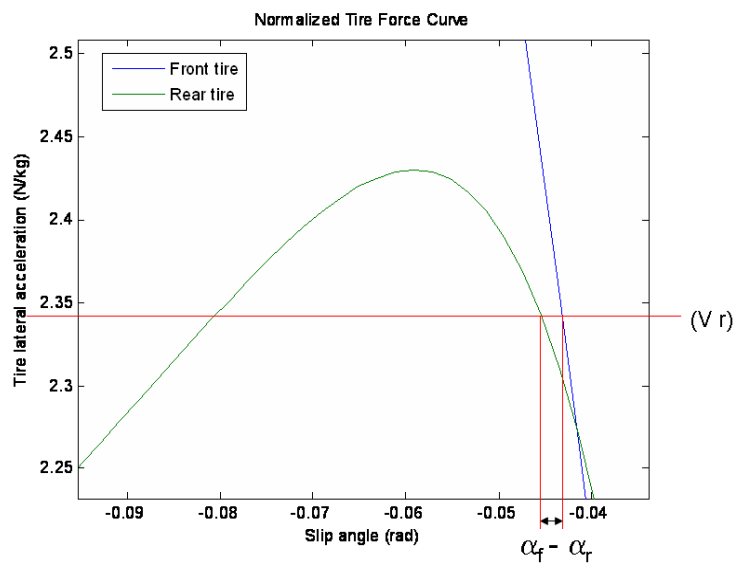Figure 4.20: Normalized tire force for bicycle model.

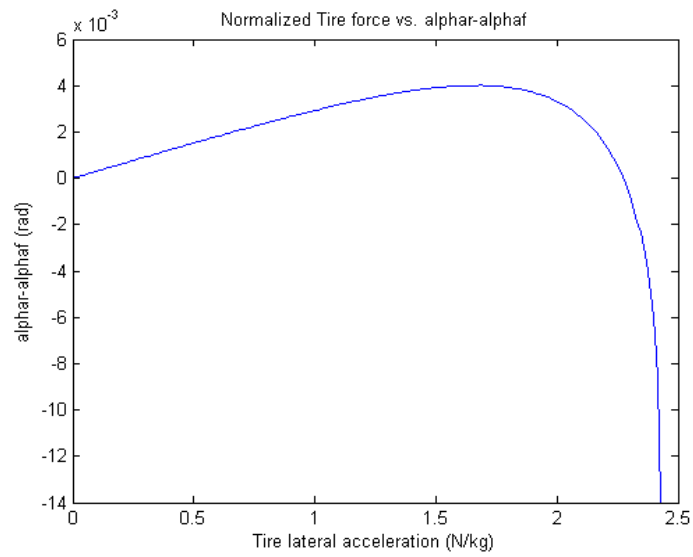Figure 4.21: Zoomed in view of normalized tire force forbicycle model.

114

Figure 4.22: $(\alpha_r - \alpha_f)$ versus normalized tire force for theoretical bicycle model.
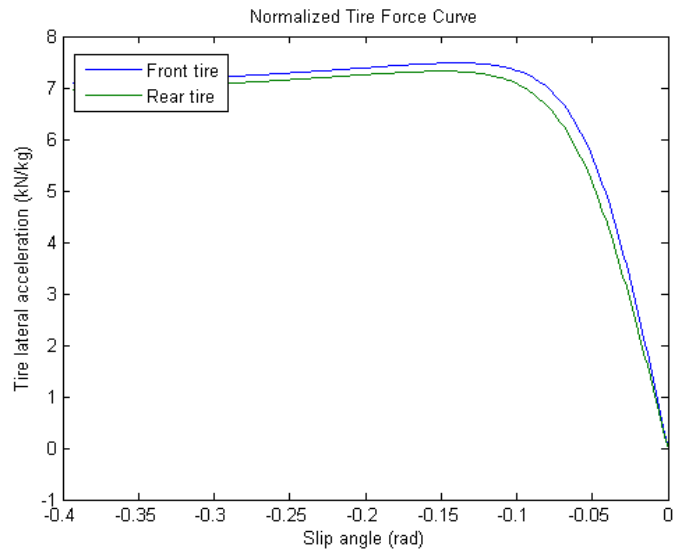

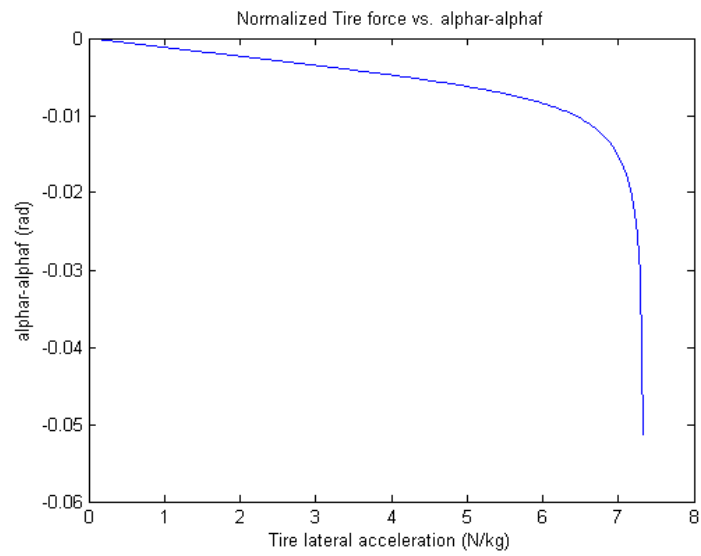Figure 4.23: Normalized tire force for LTV four-wheel model.

Figure 4.24: $(\alpha_r - \alpha_f)$ versus normalized tire force for LTV four-wheel model.

Chapter 5

Summary and recommendations for future work

This research presented a new method to study vehicle handing performance. Vehicle models evolved from a simple bicycle model to models allowing for wide operating ranges and lateral load transfer. US/OS/NS was explored for the nonlinear case, and examples of bifurcation analysis were applied.

In addition to characterizing vehicle handing performance, this method can also be used (to an extent) to predict vehicle motions for particular steering maneuvers. For example, Figure 5.1 shows a graph provided by Ivan Tong from the US Army Aberdeen Test Center (ATC) that shows a phase portrait overlayed with a curve of stable equilibrium points at several other steer angles (black line). Trajectories crossing the black line represent initial responses to a step steer input from the equilibrium steering state at each point on the black line to the steer angle of the phase portrait. Phase portraits also provide responses of steady vehicle parameters after transient maneuvers.

Bifurcation plots can be used to determine stability limits for different vehicle conditions. Vehicle specifications can be varied, and changes in handling behavior can be easily evaluated. The lateral load model is especially powerful in this regard, since simple changes such as roll bar adjustments can be examined. Homoclinic

orbits also show regions of stability on individual phase portraits and can also be used to help quantify stability limits.
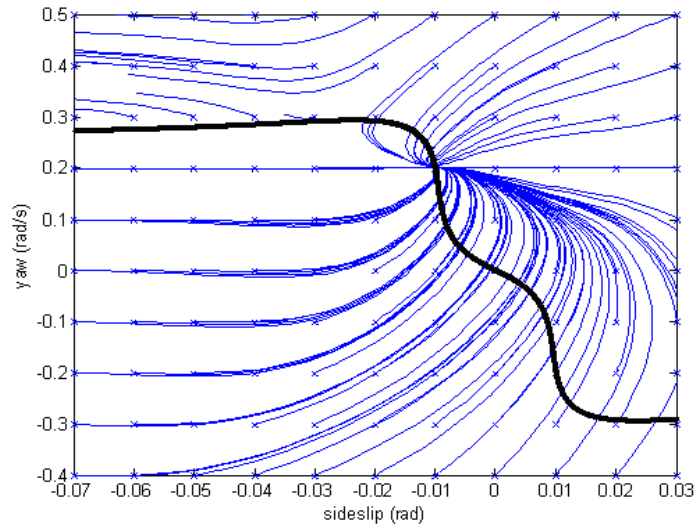
Figure 5.1: Phase portrait with overlaying plot of stable equilibrium at several other steer angles. Provided by ATC.

5.1   Recommendations for future work

Recommendations for future work include:

- Reformulating a vehicle model to allow for drive torque and combined slip effects (lateral and longitudinal)

- Investigating neutral steer bifurcation behavior in particular the apparent discontinuity observed in Figure 4.13 near convergence.

- Further examination of bifurcations with respect to steer angle and at higher steer angles with respect to velocity bifurcations.

- Further development of the lateral load model, by perhaps removing initial roll angle propagation or using animation in three dimensions for improved visualization of system dynamics.

BIBLIOGRAPHY

[1] Ahmadi, J., Ghaffari, A., and Kazemi, R., 2005, "Fuzzy logic based vehicle stability enhancement through combined defferential braking and active front steering," ASME DETC2005-85340, pp. 1-7.

[2] 2005, "Auto Alliance, Driving Innovation," http://www.autoalliance.org/safety/.

[3] Cabrera, J. A., Ortiz, A., Carabias, E., and Simon, A., 2004, "An Alternative Meathod to Determine the Magic Tyre Model Parameters Using Genetic Algorithms," Vehicle System Dynamics, **41**(2), pp. 109-127.

[4] Chengrong, H., Feisheng, Z., 1994, "The numerical bifurcation method of nonlinear lateral stability analysis of a locomotive," Vehicle System Dynamics, **23**, pp. 234-245.

[5] Forkenbrock, G., and Garrott, R., 2005, "NHTSA Vehicle Research and Test Center CRASH AVOIDANCE RESEARCH Vehicle Dynamic Rollover Propensity", http://www-nrd.nhtsa.dot.gov/vrtc/ca/rollover.htm.

[6] Forkenbrock, G., 2005, "An overiew of NHTSA's 2005 ESC research program," Ninteenth International Confrence on Enhanced Safety of Vehicles, presentation notes.

[7] Ghaffari, A., Ahmadi, J., and Kazemi, R., 2005, "Fuzzy logic based vehicle stability enhacement through active rear steering," ASME DETC2005-85350, pp. 1-7.

[8] Gillespie, T.D. 1992, *Fundamentals of Vehicle Dynamics*, Society of Automotive Engineers, Warrendale, PA.

[9] Huh, K., Kim, J., Hong, J., 2000, "Handling and driving characteristics for six-wheeled", Proc. Instn. Mech. Eng. Vol. 214 Part D, pp. 159-170.

[10] Karnopp D., 2004, *Vehicle Stability* (New York: Marcel Dekker).

[11] Klaps, J., Day, A. J., 2005, "Steering drift and wheel movements during rbaking: static and dynamic measurements," Proc. Instn. Mech. Eng. Vol. 219 Part D:J. Automobile Engineering, pp. 11-19.

[12] Lv, H. M., Chen, N., Li, P., 2004, "Multi-objective H∞ optimal control for four-wheel steering vehicle based on yaw rate tracking," Proc. Instn. Mech. Eng. Vol. 218 Part D:J. Automobile Engineering, pp. 1117-1123.

[13] M. van Oosten, J. J., and Bakker, E., 1993, "Determination of Magic Tyre Model Parameters," *Tyre Models For Vehicle Dynamics Analysis*, H. B. Pacejka eds., Offsetdrukkerij Kanters, Netherlands, pp. 19-29.

[14] Matlab Tutorial, 2005, Matlab ver. 7.0.4.365 (R14).

[15] Milliken, W.F., Milliken, D.L., 1995, *Race Car Vehicle Dynamics*, Society of Automotive Engineers, Warrendale, PA.

[16] Mokhiamar, O., Abe, M., 2002, "Combined lateral force and yaw moment control to maximize stability as well as vehicle responsiveness during evasive maneuvering for active vehicle handing safety," Vehicle System Dynamics, supplement 37, pp. 246-256.

[17] Nayfeh, A. H., Balachandran, B., 1995, *Applied Nonlinear Dynamics, analytical, computational, and experimental methods*, John Wiley & Sons, Inc., New York, Chap. 1-2.

[18] Ono E., Hosoe S., Tuan H. D., and Doi S., 1998, "Bifurcation in vehicle dynamics and robust front wheel steering control," IEEE Transactions on Control Systems Technology, **6**(3), pp. 412-420.

[19] Pacejka, H. B., Bakker, E., 1993, "The Magic Formula Tyre Model," *Tyre Models For Vehicle Dynamics Analysis*, H. B. Pacejka eds., Offsetdrukkerij Kanters, Netherlands, pp. 1-18.

[20] Sharp, R. S., "Normalization of tire shear forces for economy of testing and computation," 2005, Obtained directly from author.

[21] Sharp, R. S., 2005 "Testing and improving a tyre shear force computation algorithm," 2005, Obtained directly from author.

[22] Sharp, R. S., and Bettella, M., 2003, "Tyre Shear Force and Moment descriptions by Normalization of Parameters and the 'Magic Formula'," Vehicle System Dynamics, **39**(1), pp. 27-56.

[23] Sharp, R. S., and Bettella, M., 2003, "On the construction of a general numerical tyre shear force model from limited data," Journal of Automobile Engineering, **217** Proc. I. Mech. E., Part D., pp. 165-172.

[24] Yi, K., Chung, T., Kim, J., and Yi, S., 2003, "An investigation into differential braking strategies for vehicle stability control," Proc. Instn. Mech. Eng. Vol. 217 Part D: J. Automobile Engineering, pp. 1081-1093.